The Holocene history of Arsine Glacier (Western European Alps): a detailed 10Be record of oscillations driven by climate and modulated by rock avalanches

Melaine Le Roy, Irene Schimmelpfennig, Philip Deline, Julien Carcaillet, Tancrède P.M. Leger, Pierre Jégot, Philippe Schoeneich, Diego Cusicanqui, Felix Martin Hofmann, Xavier Bodin, et al.

The Holocene history of Arsine Glacier (Western European Alps): a detailed ^{10}Be record of oscillations driven by climate and modulated by rock avalanches

Melaine Le Roy[a], Irene Schimmelpfennig[b], Philip Deline[a], Julien Carcaillet[c], Tancrède P.M. Leger[d], Pierre Jégot[b], Philippe Schoeneich[e], Diego Cusicanqui[a,f], Felix Martin Hofmann[g], Xavier Bodin[a], ASTER Team[b,1]

[a] Environnements, Dynamiques et Territoires de Montagne (EDYTEM), Université Savoie Mont Blanc, CNRS, Chambéry, France

[b] Centre de Recherche et d'Enseignement des Géosciences de l'Environnement (CEREGE), Aix Marseille Université, CNRS, IRD, INRA, Aix-en-Provence, France

[c] Institut des Sciences de la Terre (ISTerre), Université Grenoble Alpes, Université Savoie Mont Blanc, CNRS, IRD, IFSTTAR, Grenoble, France

[d] Institute of Earth Surface Dynamics, University of Lausanne, Lausanne, Switzerland

[e] Institut d'Urbanisme et de Géographie Alpine (IUGA), Université Grenoble Alpes, Grenoble, France

[f] Institut des Sciences de la Terre (ISTerre), Université Grenoble Alpes, CNES, CNRS, IRD, Grenoble, France

[g] Institute of Earth and Environmental Sciences, University of Freiburg, Freiburg, Germany

[1] Consortium: Georges Aumaître, Karim Keddadouche, Fawzi Zaidi

Abstract

Lateglacial to Early Holocene (EH) glacier variations in the Alps have recently been thoroughly refined using ^{10}Be terrestrial cosmogenic nuclide (TCN) exposure dating of moraines. In contrast, knowledge of the spatial extent reached by glaciers during the Neoglacial period (~4.2 to 0.14 ka) is still fragmentary because of the scarcity of preserved moraines predating the Little Ice Age (LIA). In addition, although the climatic meaning of the geomorphological imprints left by debris-covered glaciers or rock glaciers is increasingly investigated, direct comparison with those of debris-free glaciers is often not possible. Here, we provide an unprecedentedly large TCN dataset for the region (n = 53) constraining the behaviour of Arsine Glacier, French Alps, from the end of the Lateglacial to the end of the LIA. Stadial moraines are present in both the western and eastern valleys formerly occupied by two separate branches of the ice body, up to ~3 km from the extant glacier front. Further upslope, the forefield of Arsine Glacier is

characterized by two prominent geomorphic complexes. The first is a peculiar landform with concentric ridges, previously interpreted as a moraine-derived rock glacier. It is framed by an extensive and chaotic boulder field and is overtopped – in the most glacier-proximal part – by the second outstanding feature, a large complex of unvegetated lateral and frontal composite moraines. The chronological results indicate that the most distal moraine sets testify to five oscillations of the western glacier branch between **11.88 ± 0.43 ka** and **11.10 ± 0.37 ka**. Robust constraints on the spatial extent of these positions show depression of the glacier equilibrium line altitude ranging from 224 m to 169 m relative to the LIA. The innermost EH complex dated here is interpreted as being related to the regional expression of the Preboreal Oscillation (PBO). The previously interpreted moraine-derived rock glacier was found to rather represent a moraine complex deposited following a rock avalanche covering the eastern branch of the ice body and the surrounding floor. This catastrophic event occurred at **10.71 ± 0.42 ka**, during the first significant warming of the Preboreal period, as shown by dating of the framing boulder field deposit. Dating of the ridges of the resulting moraine complex shows a subsequent advance of c. 1250 m peaking at **10.25 ± 0.42 ka**, followed by persistence of the debris-covered eastern tongue outboard the LIA extent until **9.52 ± 0.43 ka**. By contrast, during this interval no prominent moraine was deposited by the western glacier branch, not affected by the rock avalanche. Like elsewhere in the Alps, no ^{10}Be boulder ages corresponding to the mid-Holocene (8.2 to 4.2 ka) were found. Dating of the glacier-proximal moraine complex allows assigning its deposition to the Neoglacial period. The emplacement of this feature had started no later than **3.74 ± 0.02 ka**. A subsequent period of glacier maxima deposited a till unit dated on both sides of the glacier at **2.69 ± 0.14 ka**. During the Common Era, the first LIA-like advance occurred at **1.67 ± 0.05 ka**. During the LIA, an early advance (eLIA) deposited the outermost Neoglacial frontal moraine **650 ± 30 a** ago. Finally, the innermost preserved lateral moraine was deposited at the end of the LIA, **170 ± 10 a** ago. The Arsine Glacier record is, to our knowledge, the most detailed ^{10}Be-based Holocene-long glacier chronology in the Alps, and agrees well with other existing glacier records in the region. We propose that, apart from the directly climate-driven glacier advances and corresponding ice-marginal moraine deposits of the EH and the Neoglacial, a large EH rock avalanche occurred following warm-period-related destabilization of the cirque headwalls, bringing large amount of debris onto one part of the glacier. This excessive supply – estimated to a volume of c. **8.4×10^6 m^3** – led the eastern glacier branch to evolve into a heavily debris-covered tongue that recorded climate-related oscillations between ~10.3 and 9.5 ka outboard the LIA extent.

Keywords: Early Holocene, Neoglacial events, Glacier chronology, Rock avalanche, TCN, ^{10}Be, Debris-cover, Ecrins-Pelvoux Massif, Western European Alps

1. Introduction

Mean air temperatures currently exceed the upper limit of reconstructed natural Holocene warming [Porter et al., 2019; Affolter et al., 2019; Kaufman et al., 2020; Zander et al., 2024] set during the Holocene Thermal Maximum (HTM), between ~11.0 and 4.2 ka in the Alps [Le Roy et al., 2024; Nicolussi et al., unpublished]. The most visible expression of this ongoing climate warming is glacier mass loss and its acceleration over the last two decades, especially well documented in the Alps [Sommer et al., 2020; The GlaMBIE Team, 2025]. Small alpine glaciers show sensitive response to climate change, mostly variations of summer temperature and winter precipitation, at seasonal to decadal timescales [Bahr et al., 1988; Zekollari et al., 2020; Christian et al., 2022]. As a result, reconstructed glacier length variations represent a suitable proxy to investigate decadal- to millennial-scale climate variability over the Holocene [Leclercq and Oerlemans, 2012; Jomelli et al., 2022]. This approach helps to understand the natural climate drivers and to disentangle them from the anthropogenic contribution of today's climate evolution [Vargo et al., 2020; Roe et al., 2021; Vlug et al., 2023; Clauzel et al., 2023].

Although discontinuous, glacio-geomorphological records are invaluable to investigate Holocene climate evolution, as they provide accurate spatial and temporal bounds from which quantitative climate parameters can be extracted [Doughty et al., 2013; Mackintosh et al., 2017; Brooks et al., 2022]. In the Alps, Holocene glacier advances and prevailing climate conditions have been reconstructed based on moraine dating [e.g., Nicolussi and Patzelt, 2001; Schimmelpfennig et al., 2012; 2014; Le Roy et al., 2015; 2017; 2023; Protin et al., 2019; 2021; Braumann et al., 2020; 2021]. On the other hand, the duration and magnitude of Holocene glacier recession periods have been precisely constrained thanks to (i) tree-ring dated glacier-borne subfossil trees [Nicolussi and Patzelt, 2000; Joerin et al., 2008] and (ii) inventories of cosmogenic nuclides in recently deglaciated bedrock [Goehring et al., 2011; Wirsig et al., 2016; Schimmelpfennig et al., 2022]. The synthesis of these different datasets shows a clear tripartition of the Holocene [Le Roy et al., 2024]. The coldest conditions and largest glacier extent occurred during the early Preboreal, up to ~11 ka. During the subsequent long-lasting HTM, glaciers were most of the time smaller than their 2000-2020 CE extent, particularly during the three marked HTM Phases [HTMPs, Le Roy et al., 2024]. Finally, during the

Neoglacial period (~ last 4 ka), glaciers readvanced more frequently towards maximum positions of the Late Holocene, which were reached several times, especially during the Little Ice Age (LIA). The LIA spans the period 1260 to 1860 CE [Nicolussi et al., 2022] and its last maximum around 1850 CE is commonly used as a reference for glacio-climatological studies [Maisch et al., 2000; Reinthaler and Paul, 2025].

Distant correlations of the Lateglacial and EH glacier advances in the Alps have relied so far on the computation of morphometric parameters, like the equilibrium line altitude (ELA). Depression values of the ELA (δELA) with respect to the '1850 CE stadial' have been widely used in this way [Maisch, 1981; 1987]. However, it has been recently demonstrated that stratigraphic correlations based on this sole parameter are not reliable, as δELA can vary spatially for contemporary stadials [Reitner et al., 2016; Boxleitner et al., 2019b]. Refinement of the Lateglacial and EH morphostratigraphical framework (i.e., the succession of stadials defined and named at 'type localities') can only be achieved by systematic numerical dating. This is even more the case during the Neoglacial period, which is characterised by multiple glacier advances too similar to be discriminated on an ELA basis. Neoglacial advances of small and climate-sensitive glaciers repeatedly reached extents of the order of 1850 CE [Le Roy et al., 2024], leading to partial self-obliteration of the moraine record [Kirkbride and Winkler, 2012]. A bias towards younger periods therefore often exists, especially at large glaciers where LIA advances were the largest of the Late Holocene and overrun older deposits [Holzhauser et al., 2005; Holzhauser, 2010]. Evolving ice dynamics – e.g., under the influence of channelization by lateral moraines throughout the Neoglacial – resulted in partial preservation of some ridge sections. Only by dating the segments of these moraines preserved outboard the LIA extent, a complete picture of Neoglacial variations can emerge [e.g., Röthlisberger and Schneebeli, 1979]. Yet, quantitatively establishing a sound hierarchy of these Neoglacial advances from the sole geomorphic record remains a challenge.

While ice-marginal moraine ridges are in most cases direct proxies for paleoclimate change, non-climatic factors, such as erosional feedback, topographic controls, bedrock lithology and the presence of surface debris have also been shown to influence moraine deposition, preservation and completeness [Kirkbride and Winkler, 2012; Barr and Lovell, 2014; Rowan et al., 2022; Boston et al., 2023]. Among the most common triggers for not directly climatically driven glacier advances, rock avalanches (RAs, typically $> 1 \times 10^6$ m^3) onto glaciers have been extensively reported [Deline et al., 2017; 2021]. Supraglacial RA debris deposited in the ablation zone tend to reduce surface ablation [Reznichenko et al., 2011; Jamieson et al., 2015;

Fleischer et al., 2023] and might cause an anomalous advance and possibly subsequent 'non-climatic' moraine deposition. A few case studies provide evidence of such RA-triggered advances in the modern era [Deline, 2009; Hewitt, 2009] as well as in the paleo-record [Deline and Kirkbride, 2009; Menounos et al., 2013; Deline et al., 2015]. However, proper identification of glacially-transported RA debris is not straightforward in the sedimentary record and often precludes distinction between climatic and RA-derived moraines [Reznichenko et al., 2016].

To complement the knowledge on climate- and RA-driven Holocene glacier advances in the Alps, the forefield of Arsine Glacier is an ideal study site. It features a rich glacio-geomorphic record, including a notable suite of moraines supposedly covering the entire Holocene, and several RA deposits. By building a comprehensive Holocene-long moraine chronology of Arsine Glacier, we aim to (i) refine the existing framework of Alpine glacier behaviour during the EH and the Neoglacial, to (ii) assess whether the chronology of glacier fluctuations is consistent with (larger) glacier records elsewhere in the region, and to (iii) evaluate if an imprint of RAs on the timing of Holocene glacier dynamics can be identified.

FIGURE 1. Location of the Arsine Glacier in the context of the Ecrins-Pelvoux Massif (EPM). The location of Fig. 3 is indicated in the main map. The sites with TCN-based constraints on glacier extent since the Lateglacial are indicated as coloured dots and the moraines mentioned in the text are indicated with grey lines. The rock glaciers, proglacial lakes, rock slope failures (RSFs) and paleoecological records mentioned in the text are shown as coloured symbols. Late-Little Ice Age (~1850 CE) and modern (2009 CE) glacier extents are displayed in light blue and white, according to Mourey et al. [unpublished] and Gardent et al. [2014], respectively. The inset map shows the location of the EPM in the European Alps, along with the sites where Holocene moraines have been dated (blue: Early Holocene, pink: Neoglacial). See Fig. 10 for the compiled age datasets. The main map digital elevation model (DEM) background is the BD ALTI® 25 m from the Institut Géographique National. Lambert 93 Grid in meters (tick marks spacing is 10 km).

2. Study area and previous work

2.1. Overview of the Arsine catchment physical setting

The Ecrins-Pelvoux Massif (EPM) belongs to the external crystalline massifs, which represent the exposed Paleozoic basement in the external Western Alps. The blocks of metamorphic and

igneous rocks of Precambrian to Carboniferous age were metamorphosed and intruded by granitoids during the Hercynian orogeny [Guillot et al., 2009], then exhumed along crustal-scale faults since Oligocene-Early Miocene times. Remnants of inverted Jurassic sedimentary basins are interspersed between these blocks [Dumont et al., 2008]. The EPM has a sub-circular shape of c. 35 km in diameter and consists of two different litho-structural units: the eastern and central parts are mainly composed of migmatites and granites, while the western part presents low- to medium-grade metasediments.

The EPM is the most southerly and westerly of the major glacierized massifs in the European Alps, due to its high average altitude, with 171 km² ice extent during the LIA and 68 km² in 2009 CE [Fig. 1]. During the LIA, the mean ELA for the main EPM glaciers was c. 2763 ± 174 m (n = 63) above sea-level (a.s.l.) based on the classical Accumulation-Area-Ratio method (AAR 0.65), showing a marked eastward rising trend (c. 300 m/30 km) [Cossart, 2011]. A more realistic and climatically reliable estimate of 2895 ± 173 m a.s.l. (n = 111) was found based on recent glaciological modelling [Henz et al., 2024]. In comparison, mean ELA was 3100 ± 80 m a.s.l. for the main EPM glaciers (n = 11) over the 1984-2010 CE period [Rabatel et al., 2013], and peaked above 3300 m a.s.l. in recent years.

Arsine Glacier is located on the eastern fringe of the EPM [Fig. 1], partly sheltered from the westerlies. At 2400 m a.s.l., the mean annual air temperature is 0.92°C and the mean winter snow depth (November-April) is 1.07 ± 0.35 m (1958-2021 CE period) [Vernay et al., 2022]. Arsine is a small-sized (1.9 km² in 2015 CE, 2480-3040 m a.s.l.), north-facing and arcuate-shaped debris-covered cirque glacier [Fig. 2]. The cirque's headwall is carved into the crystalline basement, with alternating bands of Lavey gneiss/migmatite to the east towards anatectic granite to the west [Barbier et al., 1976]. The bands are separated by a network of sub-vertical faults (N20°W) that is densest at the 'Neige Cordier fault corridor', creating numerous couloirs. The glacier owes its existence to snow avalanches delivered from this 3 km-wide and 500 m-high headwall [Fig. 2]. Additional minor ice supply comes from the steep hanging Upper Arsine Glacier (0.2 km², 2860-3450 m a.s.l.), which flows down from the northwest face of the 'Calotte des Agneaux' (3634 m a.s.l.) [Fig. 2b,c]. This tributary is no longer confluent with the main cirque body since 2016 CE.

Inboard the most recent moraine complex ['Proximal Moraine Complex', see Fig. 2 and Section 4.2.5], a set of sharply defined frontal ridges indicate that the tongue recorded all known post-LIA cooling events with little lag [Fig. 2a,d]. Here, the outer moraine set – which subdivides into three nested ridges in some places – was deposited between 1892 and 1930 CE [Fig. 3; Fig.

198 8e], as shown in the first topographic map ('Service Géographique des Armées' map), surveyed
199 in 1928 CE. The first aerial photograph in 1952 CE shows that the tongue was still close to this
200 limit. Finally, the innermost moraine was deposited ~1986 CE [Fig. 2d,e]. Since the mid-19th
201 century, sustained sediment supply and decreasing flow velocity led to an expanding debris-
202 cover [Fig. 2b]. As a result, the glacio-geomorphological features observed today are
203 hummocky terrain and proglacial lakes developed since the 1940s. Several large RA deposits
204 are visible on the glacier [Fig. 3], protruding from 20-30 m relative to the surface and suggesting
205 high current levels of denudation in Arsine's cirque headwalls.
206
207 2.2. Deglaciation of the Ecrins-Pelvoux massif
208 During the last glacial maximum (27.5-23.3 ka) [Hughes and Gibbard, 2015], an ice saddle was
209 located at c. 2750 m a.s.l. above Arsine Pass (2340 m a.s.l.). Hence, the ice thickness at this
210 locality amounted to about 400 m [Beaudevin, 2001]. At that time the Romanche Glacier fed
211 the Isère Glacier (Moirans Lobe) and the Guisane Glacier fed the Durance Glacier (Sisteron
212 Lobe) [Fig. 1]. The prevailing ELA was located at c. 1600 ± 200 m a.s.l. in the region [van der
213 Beek and Bourbon, 2008; Coutterand, 2010; Leger et al., 2025]. During the EH, the Arsine Pass
214 still acted as a diffluence dividing the glacier into two glacial tongues, flowing westward in the
215 Rif de la Planche Valley (RP), where it fed the Romanche River (Isère catchment) and eastward
216 in the Tabuc Valley (TA), where it fed the Guisane River (Durance catchment) [Fig. 1]. At
217 present, Arsine Glacier's meltwater mainly feeds the Guisane River in the TA. Previous
218 research has addressed the postglacial history of the Upper Romanche and Vénéon catchments,
219 and the Guisane and Durance drainage basins [Edouard, 1978; 1994; Delunel, 2010; Cossart et
220 al., 2008; 2011; 2012]. In the following, we refer to recalculated exposure ages according to the
221 methodology described in Section 3.6 (no snow nor erosion correction and the number of TCN
222 ages retained and discarded is indicated).

223 Few Lateglacial moraines have been preserved in the EPM Massif. In the Vénéon trunk valley,
224 the hypothetical 'Ougiers moraine' (870 m a.s.l.) [Monjuvent, 1973; Bourgeat, 1990] [Fig. 1]
225 has not been dated but could correspond to the Gschnitz stadial at ~17 ka, which has been
226 correlated with the Heinrich Event 1 [Ivy-Ochs et al., 2006a]. Likely contemporary ice-
227 marginal positions, associated with a δELA of c. 700 m, have been mapped at 1050 m a.s.l. in
228 the Vallouise Valley ('GY.M_{S3}') and 1440 m a.s.l. in the Clarée Valley ('CL.M_{S2}') [Cossart et
229 al., 2011; 2012] [Fig. 1]. In the Upper Romanche Valley, ages obtained from roches
230 moutonnées on the Emparis Plateau (2300-2400 m a.s.l.), c. 15 km downstream Arsine Glacier

[Fig. 1], indicate that deglaciation of this area had occurred prior to **15.69 ± 0.47 ka** (n = 3; one outlier) [Delunel, 2010], i.e., during the recession from the Gschnitz stadial maximum position. During the Egesen stadial, which has been correlated with the Younger Dryas (YD, ~12.9-11.7 ka) [Ivy-Ochs et al., 2009], the glaciers in the EPM fluctuated several times, with most of the ice-marginal positions situated at 1800-2200 m a.s.l. [Edouard, 1978; 1994; Francou, 1981; Couteaux, 1983a; 1983b; Colas, 2000; Cossart et al., 2008; 2012; Delunel, 2010; Hofmann et al., 2019]. At the two major Egesen glacier systems (Meije-Rateau and Vallouise Glaciers), fronts were locally lower, down to c. 1400-1500 m a.s.l. [Edouard, 1994; Cossart, 2005]. In the Vallouise Valley, the first position downstream of the LIA maximum is the 'Ailefroide moraine' at 1450 m a.s.l. ('GY.M_{S4}') [Fig. 1]. This hummocky moraine complex, deposited by a paleo-glacier with a proposed ELA of c. 2300 m, probably dates from that period [Lagier and Masson, 1997; Cossart, 2005; Cossart et al., 2008]. So far, only one Egesen stadial maximum moraine was numerically dated near the EPM, the 'Stage 3' lateral moraine ('CL.M_{S3}') in the Upper Clarée Valley [Cossart et al., 2012] [Fig. 1]. It is associated with a δELA of c. 440 m and has been exposure dated to **12.47 ± 0.33 ka** (n = 2; one outlier) [Cossart et al., 2012]. In the same valley, glacier recession to the upper cirques (> 2300 m a.s.l.) occurred no later than **12.00 ± 0.39 ka** (n = 2), i.e., at the end of the Egesen stadial, as shown by the age of a polished knob immediately outboard a 'Stage 4' moraine. The subsequent glacier re-advance occurred during the Preboreal and led to the formation of the 'Stage 4' moraines ('CL.M_{S4}') dated to **10.82 ± 0.70 ka** (n = 4; 2 outliers) [Cossart et al., 2008; 2012] [Fig. 1].

Immediately downstream from our study area, several of the moraine ridges deposited by the former Romanche Glacier at 'Plan de l'Alpe' were TCN-dated [Chenet et al., 2016; Schoeneich et al., 2019] [Fig. 1; Fig. 3]. According to our interpretation (based on comprehensive mapping, new unpublished ages, recalculation of existing data without snow correction and different outlier treatment) they indicate deposition around the Lateglacial-EH boundary [Schoeneich et al., 2019], i.e., ~1 ka younger than initially published [Chenet et al., 2016].

Finally, few studies have dated Holocene glacier variations in the EPM [see Fig. 1]. Among them, only one has explicitly addressed the Neoglacial period, proposing ages for five pre-LIA advances between **4.63 ± 0.33 ka** (n = 4) and **1.08 ± 0.03 ka** (n = 2) at four glacier systems similar in size to Arsine [Le Roy et al., 2017].

2.3. Previous work at Arsine Glacier

Lory [1908] first described the Arsine Glacier moraine record. He distinguished three moraine generations and linked the outermost to the Daun stadial [*sensu* Penck and Brückner, 1909], which would correspond to the Egesen stadial as defined today. Roland Bonaparte undertook the first glaciological surveys at the Arsine Glacier in 1890-1891 CE, revealing a stationary tongue [Bonaparte, 1891; 1892]. According to Martin [1933]'s first visit, the glacier was already retreating in 1893 CE (likely since the previous year), abandoning a small frontal moraine [state shown in Fig. 2b]. The same author describes clean ice conditions and only one central medial moraine (length: 150 m, width: 40 m, height: 25 m) during the second half of the 19th century. The first glacier-wide quality photograph taken by Paul Helbronner on 30th July 1905 CE shows several well-developed medial moraines and an almost continuous debris cover in the frontal area [Helbronner, 1935] [Fig. 2b]. This is the state described by Martin [1933] during his second visit in September 1907 CE, when he mentioned a 40 m-high double-crested medial moraine.

Following high melt rates [Huss et al., 2009], the proglacial Lake Arsine began to form in the second half of the 1940s. During the 1970s, its expansion raised concerns about the stability of the moraine dam [Fig. 2d]. Geophysical and geotechnical surveys were carried out to determine the till and ice thickness, and describe till properties. In frontal position, a till thickness of 70 m was measured west of the lakes, just downstream of the 1892 CE moraine ridge [Vallon, 1989; Antoine and Fabre, 2000] [Fig. 3; Fig. 8e]. The large right lateral moraine was considered stable [Antoine and Monnet, 1986], and the glacier bed was found to be soft, made of c. 10-20 m-thick basal till [Vallon, 1992]. In 1969 CE, an ice thickness of at least 70 m was determined at the glacier front and of c. 115 m to 900 m upstream, at the upper profile [Echevin, 1970] [Fig. 3]. For comparison, mean and maximum ice thickness dropped to c. 25 ± 20 m and 95 m in 2015 CE. In the spring of 1986 CE, the high risk of lake outburst flooding (lake volume c. 0.8×10^6 m^3 in 1985) led to the digging of a drainage channel through the frontal moraine [CEMAGREF, 1986; Vallon, 1989; Lahousse and Guen, 1998]. The ablation stake network (n = 17) set up in 1985 CE [Vallon, 1992] was discontinued between 1995 and 1999.

From 1969 to 1989 CE, both ice fluxes of the glacier showed opposite behaviours. The western part thickened c. 15 m while the eastern part thinned c. 10 m. Between 1989 and 1990 CE, a sharp fall in the velocity (30-50%) initiated thinning on the western part and slight thickening on the eastern part from 1992, due to slowing of the calving rate [Vallon, 1992]. During the early 1980s advance, ice flow velocity peaked at c. 50 m a^{-1} in areas where it was only 8-9 m a^{-1} in 1970, 13 m a^{-1} in 1985 and 3 m a^{-1} in 2000 CE [Vallon and Vincent, 2000]. The mass

balance series reconstructed by deep learning methods since 1967 CE shows few balanced or positive years [Bolibar et al., 2020], except in 1977-1988 [Fig. 2e], when a positive anomaly was responsible for the deposition of the innermost moraine set [Fig. 2d; Fig. 3]. Arsine Glacier's response time has been approximated to 17 years by Zekollari et al. [2020], which is quite reactive given the debris cover, and agrees with its rich post-LIA moraine record [Fig. 3; Section 2.1].

FIGURE 2. Overview of the Arsine Glacier cirque. **(a)** Stitched panorama based on the two earliest known photographs of Arsine Glacier (western lobe), taken in 1892 CE by Joseph Lemercier (© BNF Gallica, F. 36/38 bis, http://ark.bnf.fr/ark:/12148/cb405892283). The light blue arrows point to the three LIA frontal moraines, the outermost of which was sampled here (see the encircled location of the ARS-19-15 mega-boulder). The dark blue arrow points to the 1892 CE glacier front and the small moraine formed that very year, **(b)** Historical photograph of Arsine Glacier taken by Paul Helbronner from the western Combeynot summit (3155 m a.s.l.) on 30th July 1905 CE (© Musée dauphinois - Département de l'Isère). Former tributaries of Arsine Glacier during the Holocene are indicated (Casset and Chamoissière Glaciers were not tributaries during the Holocene, but had been earlier) as well as main peaks of the Ecrins-Pelvoux Massif. The white arrows highlight three of the TCN-dated crests at both composite lateral moraines. At the RLM, these are the 'PMC RLM outer crest' and 'PMC RLM inner crests'. The innermost dated ridge at the RLM is a secondary ridge located between the two main ridges pointed here [see also Fig. 4b]. Note that, due to erosion, the innermost ridge here (not arrowed) and a part of the 'PMC RLM inner crests' have disappeared since 1905 CE. At the LLM, the arrow highlights the short 'PMC LLM outer crest' (here underlined by shadow), **(c)** Overview of the Arsine cirque seen from the north based on a 14th July 2015 CE orthophoto draped on a DEM showing the main localities mentioned in the text, **(d)** Bathymetric map of the western lake surveyed in 1997 CE with the location of recent immersed moraine ridges. The most prominent emerged ridge is the 1986 CE moraine, while still-stands have led to small moraine deposition between 1970 and 1975 and around 1992 [Lahousse and Guen, 1998], **(e)** Deep-learning-reconstruction-based surface mass balance series of Arsine Glacier between 1967 and 2015 CE [Bolibar et al., 2020]. RLM: right lateral moraine, LLM: left lateral moraine, PMC: proximal moraine complex, aRG: 'apparent rock glacier'.

3. Methods

The survey involved (i) a detailed geomorphological mapping, (ii) the establishment of a local morphostratigraphy, (iii) the selection of the best-preserved glacial positions for reconstruction of the glacier paleo-surfaces, (iv) the calculation of ELA and δELA relative to the LIA reference ELA, and (v) TCN-dating of suitable boulders.

3.1. Geomorphological mapping

A complete geomorphological survey was conducted focusing on glacial, periglacial and gravitational features. This is a necessary prerequisite for any dating programme [Chandler et al., 2017; Winkler, 2018]. We used a combination of high-resolution aerial images, with up to 20 cm/pixel (Institut Géographique National ortho-image, Google Earth, Bing, ESRI basemap), with different lighting orientations, to delineate the landforms [Fig. 3]. To gain insights into the extent and significance of block fields and RA deposits, we also manually digitized all boulders larger than 2 m² (n = 11,000) on the valley floors based on high resolution orthophotos [Fig. 3]. Additionally, a 26 cm DEM was created from a set of 30 digital aerial images acquired on the 10th of August 2013 CE (25-cm ground sample distance) through the use of the Structure-from-Motion technique [Smith et al., 2015] in Agisoft Metashape [version 1.6.2; Agisoft, 2019]. We used twenty-one ground control points collected from the RGE ALTI 5 m dataset of Institut Géographique National. We further added nine GPS points derived from differential GPS measurements on stable areas [C. Vincent, pers. comm.], mainly located on the Neoglacial moraines of Arsine Glacier, to improve the Structure-from-Motion DEM accuracy. Then, we used a high-density point cloud methodology into Agisoft Metashape to generate the DEM, following the protocol of Cusicanqui et al. [2021]. Finally, the DEM was checked against sixteen other ground control points (also derived from differential GPS measurements). A mean RMSE of ± 0.9 m was obtained from this comparison, highlighting its high vertical accuracy.

3.2. Morphostratigraphy

A local morphostratigraphy was built [e.g., Schoeneich, 1998] allowing (i) to define and label the successive glacier frontal positions and (ii) to assess the temporal relationship of RA deposits relative to the glacier positions. Given the bilobate paleo-geometry of Arsine Glacier during the Early Holocene, moraines representing contemporary ice-marginal positions can be found in both the western Rif de la Planche (RP) and eastern Tabuc (TA) Valleys [Fig. 3]. The set of glacial landforms is better preserved and resolved in the RP Valley than in the TA Valley [Section 4.2]. All individual frontal positions were labelled from the youngest to the oldest (RP1 to RP7 and TA1 to TA7) [Fig. 3], not including the Proximal Moraine Complex (PMC)

362 [Fig. 2]. The inverse chronological order opens the series downwards for older stadials lying
363 outside of the study area. To determine Lateglacial-EH ice-marginal positions of the paleo-
364 glacier, we associated frontal positions in both valleys based on (i) relative stratigraphy, (ii)
365 glacier front elevation, and we confirmed it by (iii) numerical dating, if applicable.

366 As a sound terminology is necessary to ensure consistency, the classical approach [e.g., Gross
367 et al., 1977; Maisch, 1981] classifies moraines into:

368 - 'Positions' ('Stand' in German, 'positions' in French): position of the glacial front
369 defined by an individual frontal or near-frontal moraine.
370 - 'Stadials' ('Stadium' in German, 'stades' in French): higher hierarchical unit, often
371 formed by several close lying positions, and interpreted as a readvance.

372 The so defined morphostratigraphical stadial does not necessarily have a climatic significance,
373 as not every moraine is linked to climatic oscillations [e.g., Barr and Lovell, 2014; Rowan et
374 al., 2022]. The grouping of close lying positions into a same stadial is an assumption that such
375 positions belong to a same phase of glacier advance/retreat. This introduces a bias that can be
376 overcome by grouping in a stadial only the frontal positions that can be linked to a same pair of
377 lateral moraines. This works in one sense (distinct lateral moraines indicate different stadials),
378 but not in the other (the same lateral moraines can be reused by a subsequent glacier advance,
379 as it is the rule during the Neoglacial). In other words, it can be used in case of a continuous
380 retreating trend, like during the Lateglacial and Early Holocene. The classical Eastern Alpine
381 Lateglacial stratigraphy and its succession of stadials (Egesen and substadials, Kartell, Kromer)
382 [Maisch, 1987], as well as the Neoglacial stadials [Le Roy et al., 2024] are used for comparison
383 purpose in the Discussion section.
384
385 3.3. Glacier reconstruction
386 The paleo-glacier outlines for the three main stadials were drawn based on our
387 geomorphological mapping. Then, paleo-glacier surfaces were obtained by manually tracing 20
388 m-spaced contour lines following a well-established procedure [Sissons, 1974; Lukas and
389 Bradwell, 2010]. Contours were drawn perpendicular to previously established flowlines, with
390 convex and concave shape in the suspected ablation and accumulation zones, respectively.
391 Contour establishment is based on robust lateral constraints in the ablation zone (moraines,
392 trimlines) but is more challenging in the accumulation zone. In addition, significant changes
393 that occurred in the lower part of the accumulation zone since the LIA must be taken into
394 account, otherwise leading to substantial errors [Reinthaler and Paul, 2024]. We used the

'Service Géographique des Armées' map surveyed in 1928 CE to estimate thickness changes above c. 2800 m a.s.l. For the reconstruction of the two oldest paleo-glaciers, the accumulation zone elevation was kept similar as during the LIA above this altitude. The DEMs (10 m cell size) of the paleo-glaciers surface were obtained with the 'Topo to Raster' tool in the ArcGIS software [Hutchinson, 1989]. The paleo-glacier bed was reconstructed using the same method. The main slope deposits were manually removing from the RP and TA Valley floors, and the available geophysical data were used for the PMC area [Echevin, 1970; Antoine and Fabre, 2000] [Fig. 3; Fig. 9].

3.4. Investigation of mass movements

Volume estimate is a prerequisite for characterizing the magnitude of catastrophic events. We have combined different methods to assess uncertainties relating to the thickness of the RA deposits. Firstly, we used cross profiles drawn at evenly-spaced locations to compare surface elevation (based on the high-resolution DEM, Section 3.1) with nearby debris-free terrain. Regarding the landform hereafter called 'apparent rock glacier' (aRG) [Fig. 2; Fig. 3], the height of the clearly-defined lateral and frontal talus was first measured to obtain a rough volume estimate [e.g., Barsch and Jakob, 1998] [Fig. 7d]. Secondly, we differentiated the paleo-topography (obtained by removing slope deposits) from the modern surface for the mapped RA deposits. Thirdly, we used the 'Topo to Raster' tool to automatically reconstruct the paleo-topography only below the aRG. To derive bedrock volume estimations, a conservative value of 30% was applied for porosity, both for the RA deposits and for the aRG. This value appears generally suitable for RA [Nicoletti and Sorriso-Valvo, 1991; Stock and Uhrhammer, 2010], relict rock glaciers [Wahrhaftig and Cox, 1959; Munroe et al., 2024] and coarse-grained till deposits [Parriaux and Nicoud, 1990; Ronnert and Mickelson, 1992; Burki et al., 2010].

The computation of the apparent friction coefficient (so-called *fahrböschung*) by dividing the fall height (H) by the runout length (L) informs on the RA mobility and can give insights into possible substrate along the travel path. Indeed, RAs that partly travel onto the ice tend to have lower H/L ratio for a given volume [Schneider et al., 2011; Deline et al., 2021].

3.5. ELA modelling

Paleo-ELAs represent a valuable climate proxy relying on former glacier extents, as well-formed frontal moraines indicate a near equilibrium state. We computed paleo-ELAs for the three most relevant positions of Arsine Glacier and used the 1850 CE stadial as datum for δELA

calculation. The ELAs were calculated with an ArcGIS toolbox [Pellitero et al., 2015] based on the DEMs of the reconstructed paleo-glaciers. The contour line interval was set to 10 m, resulting in an error of 5 m in the ELA and an uncertainty twice as large in the δELA [Pellitero et al., 2015]. Results based on two approaches are reported hereafter, the Accumulation-Area-Ratio (AAR) and the Area-Altitude-Balance-Ratio (AABR) methods [Rea, 2009]. Traditionally, an AAR of 0.67 has been widely used in the Alps for clean ice valley glaciers [Gross et al., 1977], while a global median value of 0.58 has been recently proposed [Oien et al., 2022]. As Arsine Glacier did not have a proper accumulation area during the Late Holocene, it can be defined as a cirque glacier. ELAs of small cirque glaciers are known to be difficult to estimate owing to the headwall topographic control on snow accumulation. For instance, Kern and László [2010] found size-dependent values of steady-state AAR of 0.54 and 0.64, for glacier area below and above 4 km², respectively. Using their data from the Alps, this would yield AAR values of 0.69 and 0.66 for the two oldest dated Arsine paleo-extents, with areas of 8.7 and 6.7 km². For the end of the LIA (1850 CE), when Arsine Glacier was 3.4 km² (4.3 km² with former tributaries), the AAR would have been 0.58. Based on this rationale, we considered the 0.67 and 0.54 ratios as suitable for the EH and Late Holocene at our study site. Regarding AABR, given the sensitivity of the balance ratio to regional climate, the regional value of 1.29 for the Alps is to be preferred to the global median value of 1.56 [Oien et al., 2022]. However, this regional value was calculated on a set of glaciers all located in the dry eastern Alps [Oien et al., 2022]. It is therefore likely that these two values represent the bounds of the true range. As a result, we computed ELAs with AARs of 0.54/0.67 and AABRs of 1.3/1.6.

In addition, independent evidence for the minimum elevation reached by the ELA for a given position can be approximated using the Maximum Elevation of Lateral Moraine (MELM) method [Lichtenecker, 1938; Kerschner, 1990]. It assumes that lateral moraines cannot be deposited above the ELA. Hence, a minimum constraint is given by their maximum elevation. This proves useful to tune the results of previous methods with ground-truth evidence in the case of topographically-constrained and avalanche-fed glaciers, as in this case. We then assessed the reliability of the AAR and AABR results by comparing them with MELM estimates, which were ultimately preferred in case of conflict with former values (i.e., higher ELA value based on MELM). The MELM method yields generally good agreement with other methods in the Alps, provided that certain conditions are met [e.g., Bichler and Reindl, 2013; Gschwentner et al., 2020].

3.6. TCN exposure dating

3.6.1. Sampling

Sampling was carried out during five field campaigns between 2012 and 2019 CE. We selected the most prominent boulders on each targeted moraine/landform identified during geomorphological mapping. Hammer and chisel, sometimes in combination with an angle grinder and a diamond blade, were used to collect c. 1-4 cm thick samples from boulder surfaces [Supp. Tab. 1]. The sampled lithologies were gneiss and granite. Whenever possible, quartz veins were sampled. Although the selected boulders were mostly sited in wind-swept locations, a few were located in wind-sheltered places, when there was no alternative. Sample locations were accurately pointed on a HR ortho-image (20-cm ground sample distance), assuming a horizontal uncertainty of 0.5 m. Their elevation was recorded either with a TRIMBLE Geo7x GPS device or extracted from the structure-from-motion-based DEM, assuming a vertical uncertainty of c. 1 m. Topographic shielding was recorded in the field with a compass and clinometer. Pairs of azimuth and elevation angles were then converted into the dimensionless shielding factor with the aid of the calculator available at http://stoneage.ice-d.org/math/skyline/skyline_in.html taking self-shielding (dip of the surface) into account [Supp. Tab. 1].

3.6.2. Sample processing

Sample processing for ^{10}Be dating was conducted at the Cosmogenic Nuclide laboratory of ISTerre (Grenoble, France; the six samples labelled ARS-12-06 and -08 and RP-16-05 to -08) and at the National Laboratory for Cosmogenic Nuclides (LN2C) of CEREGE (Aix-en-Provence, France; all other samples). After isolation and purification of the quartz, a ^{9}Be carrier (3025 ± 9 µg ^{9}Be g^{-1}) produced in-house from a phenakite mineral was added, the quartz was dissolved in HF, and Be was isolated following standard ion exchange procedures based on Merchel and Herpers [1999] [Tab. 1]. Beryllium-10/beryllium-9 ratios of the BeO targets produced from each sample and 10 chemistry blanks were measured at the ASTER AMS facility of CEREGE [Arnold et al., 2010], using the in-house standard STD-11 with a ^{10}Be/^{9}Be ratio of (1.191 ± 0.013) × 10^{-11} [Braucher et al., 2015] and the ^{10}Be half-life of (1.387 ± 0.012) × 10^{6} years [Chmeleff et al., 2010; Korschinek et al., 2010] [Tab. 1]. Chemistry blank corrections were performed by subtracting the number of atoms in the blanks (n = 10) from those in the samples [Tab. 1]. The analytical uncertainties in the resulting ^{10}Be concentrations include (i) measurement uncertainties (AMS counting statistics), (ii) the error of average

494 standard measures, (iii) the systematic error of ASTER [0.5%; Arnold et al., 2010], (iv) the ^{9}Be
495 carrier weight uncertainties, and (v) the error of the ^{10}Be concentration in the blank.
496
497 3.6.3. Age calculation and interpretation
498 The choice of the scaling model, the production rate and the geomagnetic database is decisive
499 for the discussed results. Surface exposure ages were computed with the CREp online calculator
500 [Martin et al., 2017; https://crep.otelo.univ-lorraine.fr/#/, last accessed February 2025] using
501 the Lal-Stone 'Lm' time corrected scaling model [Balco et al., 2008], the ERA40 atmospheric
502 reanalyses [Uppala et al., 2005] and the Lifton VDM 2016 geomagnetic database [Pavon-
503 Carrasco et al., 2014; Lifton, 2016], i.e., the 'Lm-ERA-Lift' combination [Tab. 2]. We chose
504 to apply the local 'Alps' ^{10}Be production rate of Claude et al. [2014] with a value of 4.07 ± 0.10
505 at g^{-1} a^{-1}, as resulting from the ICE-D database linked to CREp, which is close to the global
506 average ^{10}Be production rate (4.09 ± 0.19 at g^{-1} a^{-1}). No erosion nor snow corrections have been
507 applied. Although the majority of sampled boulders (70%) were taller than the mean snow depth
508 in the area (1 m thick at the average altitude of the samples), our exposure ages must be seen as
509 minimum ages. This is especially true for wide/flat boulders and those sampled below 80 cm
510 (10 out of the 53 boulders) in wind-shielded areas (e.g., 'PMC RLM distal face-Mid.') [Supp.
511 Tab. 1].

512 To allow comparison with previous work in the Alps [e.g., Braumann et al., 2022], we also
513 computed a second set of ages with the version 3 of the former CRONUS-Earth online
514 calculator [Balco et al., 2008; https://hess.ess.washington.edu/math/v3/v3_age_in.html, last
515 accessed February 2025] using the same parameters as above regarding the ^{10}Be production rate
516 (calculated as 3.99 ± 0.37 at g^{-1} a^{-1} using the calibration data from the ICE-D database), the
517 scaling scheme, the atmosphere model, and the geomagnetic field model also based on Lifton
518 [2016]. Finally, a third set of ages was computed with CREp with the current generally accepted
519 scaling method, the physically-based 'LSDn' model [Lifton et al., 2014], using the same
520 parameters as above and the 'Alps' production rate (calculated as 4.16 ± 0.10 at g^{-1} a^{-1}), i.e., the
521 'LSD-ERA-Lift' combination [Tab. 2].

522 To address the geological scatter caused by post-depositional moraine degradation or
523 inheritance [Balco, 2020], outliers have been detected according to the reduced chi-squared
524 statistics. To ensure the data represent a single population, a reduced chi-squared value should
525 fall within a 2σ envelope (95% confidence) determined by the chi-squared criterion [Spencer
526 et al., 2017]. When reduced chi-squared was above this criterion, the sample furthest from the

mean was pruned. After outliers' removal, the landform mean ages were computed using the error-weighted mean of the included ages and their weighted average internal and external uncertainties, after Rodés [2020a] [Tab. 2]. The individual and mean ^{10}Be ages reported in the Results section do not include the production rate uncertainty. The ages reported in the Discussion section include the external uncertainties (production rate uncertainty added in quadrature) to allow comparison with other dating methods. All exposure ages from the literature reported here were recalculated with the same parameters as those used in the present study, so the conclusions we draw may differ from those expressed by the authors in the original articles. We hereafter report chronological information as 'ka', i.e., kiloyears before the year of sampling, or as calendar years (including a year 0) for tree-ring and ice core data. Radiocarbon ages are recalibrated according to Reimer et al. [2020] and reported as 'cal ka' (only the median probability is reported for sake of clarity).

3.6.4. Bayesian filtering

We employed a Bayesian age model to refine our chronology of the oldest dated deposition events as individual ages from these landforms overlap, and the mean age of the RA deposit slightly conflicts with the morphostratigraphic sequence. Based on the relative order of events, the Bayesian age model filters ages that are inconsistent with the landform stratigraphy and thus estimates the most likely, stratigraphically-consistent probability age distributions. Bayesian models have been widely applied to establish chronologies of lake and marine sediment cores [e.g., Bronk Ramsey, 2008] and are increasingly used to refine TCN chronologies exhibiting closely-spaced landform ages [Chiverrell et al., 2013; Hofmann et al., 2019; Martin et al., 2020b; Charton et al., 2022]. The code used for our Bayesian age model is the Cosmo-Ages Sequence Calculator [Rodés, 2020b; Leger et al., 2021]. It produces a probability distribution (also termed a posterior density estimate) for each landform, by employing a Markov Chain Monte Carlo sampling approach. Prior to our Bayesian analysis, only the most obvious outliers irreconcilable with stratigraphy (ARS-13-02, ARS-16-03 and ARS-16-14) were removed from the dataset, while tight outliers identified from the reduced chi-squared test were kept, which doesn't affect the modelled ages [Fig. 3; Fig. 5].

FIGURE 3. Glacio-geomorphological map of the Arsine Glacier catchment with TCN dating results. The mapping of the glacier extent and features reflects the state of 2015 CE. TCN samples are shown as yellow dots. For each exposure-dated surface, the error-weighted

mean age is reported after exclusion of outliers (based on the reduced chi-squared test) and is accompanied by its weighted average internal uncertainties. For the oldest landforms, the Bayesian-filtered mean age (followed by an asterisk, see Section 3.6.4), which is used in the Discussion section, is shown above the error-weighted mean age (italic grey font), which may include stratigraphic outliers (i.e., single ages that conflict with the mean ages of the framing surfaces). The Arsine Glacier Early Holocene ice-marginal positions are indicated in black font. The locations of geophysical surveys carried out by Echevin [1970] and Antoine and Fabre [2000] are shown as white and light brown dots, respectively. LG: Lateglacial, EH: Early Holocene. Lambert 93 Grid in meters (tick marks spacing is 1 km).

4. Results and interpretation

TABLE 1. Results of the ^{10}Be measurements at Arsine Glacier.

4.1. Impact of scaling schemes on exposure ages

As an introductory remark, we consider that both first sets of ages presented in Tab. 2 are equally robust and that it is not possible to objectively choose one over the other. The second set of ages (CRONUS 'Lm') is on average close to the ages retained here (CREp 'Lm'), but with opposite sign between the Early Holocene (2.2% older) and the Late Holocene (3.6% younger) [Tab. 2]. Based on comparison with near calendar-dated independent evidence available in the Alps (high resolution speleothem records and tree-ring dated moraines) [Le Roy et al., 2024], it appears that the first set would provide slightly 'too old' ages for the Late Holocene and that the second set would provide slightly 'too old' ages for the Early Holocene [Fig. 10; Fig. 12]. We therefore interpret the ages retained here for the Discussion section as minimum-limiting for the Early Holocene and maximum-limiting for the Late Holocene.

The third set of ages (CREp 'LSDn') is on average 8% younger than the ages retained here [Tab. 2]. Although this combination was used in a previous study dealing with Late Holocene landforms in the EPM [Le Roy et al., 2017], it has not been retained here as it gives 'too young' ages for the Early Holocene [Tab. 2]. Choosing this model would violate state-of-the-art knowledge on glacier chronology in the Alps [Le Roy et al., 2024], as none of the outer moraines here would be assigned a deposition age older than 11 ka [Tab. 2]. This discrepancy is in line with studies showing that 'LSDn' ages are inconsistent with independent radiocarbon age control over the Lateglacial period [e.g., Strand et al., 2024]. The widely-used and simpler

592 'Lm' framework performs similarly for Holocene timescales, and can be used for locations and
593 ages close to the calibration dataset [Putnam et al., 2010; Borchers et al., 2016].
594
595 **TABLE 2. ^{10}Be TCN boulder exposure age results and mean surface ages computed at**
596 **Arsine Glacier, according to three different scaling schemes.** Individual and mean ages are
597 reported with the internal (analytical) uncertainties and the external uncertainties (including
598 production rate uncertainties) between brackets. No snow- nor erosion- correction have been
599 applied (see main text). Pruned outliers are in italic (see Section 3.6.3). The weighted mean
600 ages shown here (together with weighted mean internal and external uncertainties) are not
601 necessarily the landform ages used in the Discussion section (see Section 3.6.4). For calculation
602 we assumed a rock density of 2.65 g cm^{-3}. Exposure ages are expressed in ka before the
603 sampling year (indicated in sample label).
604
605 4.2. Geomorphological description and ^{10}Be chronology
606 4.2.1. Rif de la Planche (RP) Valley
607 The wide and even RP Valley allowed the preservation of a succession of lateral and frontal
608 moraine remnants [Fig. 3]. We identified one ice-marginal position marking a former
609 confluence of Arsine and Romanche Glaciers (RP7) and six main positions between the
610 confluence with Romanche Glacier and the PMC (RP6 to RP1) [Fig. 3]. During part of the YD
611 chronozone (12.9 - 11.7 ka), the Arsine Glacier was likely confluent with the Romanche Glacier
612 to the west (RP branch) and confluent with the Casset Glacier to the east (TA branch). The
613 geometry of the right lateral ridge deposited by the Romanche Glacier at the confluence with
614 the RP Valley (noted 'RO Outer' on Fig. 3] shows that both glaciers were no longer confluent
615 when it was deposited, i.e., shortly before **11.76 ± 0.20 ka** (n = 4) [Schoeneich et al., 2019]. In
616 the RP Valley, the outermost positions (RP6a-c) are documented by three subdued moraines
617 lacking sharp crests. The next ones (RP5a-b) are represented by the most extensive moraine set
618 in the RP [Fig. 4a]. They featured two closely-spaced (60 m) well-defined frontal moraine
619 ridges, mostly matrix-supported, with RP5a being located at 2160 m a.s.l. [Fig. 3; Fig. 4a].
620 Several other nested minor moraines (not labelled) are associated with these two main ridges,
621 both outboard and inboard, indicating that the RP5 positions were occupied over a long period
622 of time [Fig. 4a]. Four consistent ages ranging from 11.02 ± 0.33 ka to 11.85 ± 0.43 ka were
623 obtained from the RP5a position (RP-16-05 to -08), yielding a mean age of **11.50 ± 0.37 ka**.
624 Although the youngest age (RP-16-06) is not considered an outlier according to the reduced

chi-squared test, it is in conflict with the mean age of the next dated surface inboard (RP2). The Bayesian analysis gives an age of **11.88 ± 0.43 ka** (n = 4) for the RP5a moraine, serving as upper bound for younger stratigraphic units (unit 1; 'Outer complex') [Fig. 3; Fig. 5]. The continuity of the left lateral moraine corresponding to this frontal position reveals that the north-facing Chamoissière cirque – deglaciated today but confluent with Arsine Glacier sometime before ~11.9 ka – was disconnected from the trunk valley during RP5a moraine deposition [Fig. 3; Fig. 4a]. Another well-marked frontal ridge segment (RP4) is present 350 m upstream of RP5a [Fig. 3; Fig. 4a]. The next younger position, RP3 (at 2195 m a.s.l.), is materialized by a ridge partially buried by slope deposits left of the stream, associated with a short but well-defined ridge on the right-hand side. The left ridge bounds the downstream tip of an extensive blockfield, interpreted as a RA deposit paving the RP Valley floor [Fig. 6a]. The last prominent position in RP, and the second to be dated, is the sharp-crested latero-frontal ridge named RP2, that dams the 'Lac de l'Etoile'. It is located 880 m upstream from RP5 with a frontal position at 2220 m a.s.l. The four boulders sampled on the RP2 moraine gave ages between 9.97 ± 0.30 ka and 11.08 ± 0.38 ka (RP-16-01 to -04), yielding a mean age of **10.88 ± 0.25 ka**, after discarding the youngest age according to the reduced chi-squared test. Eroded latero-frontal moraine remnants located 750 m upstream of RP2 and 500 m downstream of the PMC were labelled RP1 [Fig. 6b]. This moraine set is associated with a kame terrace located at the confluence of the RP Valley and the hanging Dragon Valley. A little further upstream, a lateral moraine remnant of Arsine Glacier, located at c. 2420 m a.s.l. on top of a cliff at the mouth of Dragon Valley and partly covered by the Proximal Moraine Complex [Fig. 3], may also be plausibly linked to the RP1 ice-marginal position.

FIGURE 4. **Examples of sampled boulders at two locations of the Arsine Glacier forefield.** **(a)** The outermost Lateglacial to Early Holocene moraines in the RP Valley. Left panel: View southward over the outer frontal ridge of the RP5 moraine doublet (RP5a), which was dated here. The RP5 left lateral moraine is highlighted, showing its continuity below the Chamoissière cirque. This indicates that the cirque ice body was no longer confluent with the valley tongue when RP5 moraines were deposited. Right panel: Two examples of the four boulders sampled on the RP5a frontal moraine ridge with TCN dating results, **(b)** Early Holocene to Little Ice Age moraines dated at the RLM. Upper panel: Overview of the RLM looking north-west with all sample locations. The vantage point of each close-up photograph is indicated. Lower panel: Close up photographs of the Late Holocene dated boulders. Note the cross painted for earlier

658 photogrammetric investigations on the flat boulder of sample ARS-16-20, which is sitting right
659 on the outer RLM crest.
660
661 4.2.2. Tabuc (TA) Valley
662 The narrow Tabuc Valley is less suitable for conservation of glacial landforms than the RP
663 Valley, given intense morphogenic slope activity. The highest visible lateral moraines are
664 located at 2380 m a.s.l. on both sides of the TA Valley (position TA7) [Fig. 3]. They can be
665 geometrically linked to a right lateral moraine underlined by scree and trees perched in the north
666 facing slope at the outlet of the valley (between c. 2050 and 2030 m a.s.l.). It reflects a position
667 when Arsine Glacier was confluent with the Casset Glacier to the east, likely at the end of the
668 Lateglacial period [Fig. 3]. No position corresponding to RP6 has been identified in TA Valley.
669 About 400 m upstream, a remnant of a frontal moraine (TA5) is visible, mostly on the right
670 bank of the stream, where it is underlined by trees, but also on the left bank where it is covered
671 by scree [Fig. 3]. This landform documents an ice-marginal position at 2098 m a.s.l. The third
672 moraine set mapped in the Tabuc valley (TA4) is the least evident. Faint traces in a colluvial
673 fan on the left bank can be linked to a flat spot on the right bank at 2160 m a.s.l., probably
674 covered by a RA deposit. The next ice-marginal position, TA3, consists of a doublet of little
675 marked latero-frontal moraine remnants covered by slope deposits which are present on both
676 sides of the valley, making the reconstruction reliable. Corresponding lateral moraines are
677 present on the left bank at around 2342 and 2335 m a.s.l. The best-preserved complex, and the
678 only dated moraine in the valley, TA2, comprises a right lateral moraine and a small remnant
679 on the left side, both suggesting a frontal position around 2215 m a.s.l. [Fig. 3]. After removing
680 an obvious outlier (ARS-13-02, apparent age of 5.27 ± 0.42 ka), the remaining three consistent
681 ages range from 10.71 ± 0.39 ka to 11.34 ± 0.36 ka (ARS-13-01, -03 and -04), yielding a mean
682 age of **11.08 ± 0.25 ka** for the TA2 moraine complex. Finally, the TA1 positions (TA1a-c) are
683 represented by the aRG moraine ridges (see Section 4.2.4).

684 Owing to the similar (i) stratigraphic position, (ii) altitudes of their fronts (c. 2220 m) and (iii)
685 ranges of boulder ages, we combined the seven ages from the TA2 and RP2 moraines as the
686 stratigraphic unit 2 ('Inner complex'). We also included to this unit the ages obtained in lateral
687 position at the 'PMC RLM distal face-Mid.' that average **10.72 ± 0.20 ka** (see Section 4.2.5 for
688 rationale). After applying the Bayesian age model, the age of this second unit is **11.10 ± 0.37**
689 **ka** (n = 10) [Fig. 3; Fig. 5].
690

FIGURE 5. Bayesian age modelling of Arsine Glacier Early Holocene landforms. Probability distributions of the TCN-dated Early Holocene landform deposition ages before (blue) and after (red) Bayesian filtering. The tight outliers identified from reduced chi-squared statistics were kept for modelling. This explains why the potential boulder exhumation or instability component is visible in the probability distributions of the Outer and Inner complexes. Note the probably inherited component visible both in the probability distributions of the RA2 deposit and the outer ridge of the 'apparent rock glacier' (TA1a moraine). One sigma standard deviation of the distribution is indicated by the length of corresponding bars.

4.2.3. Rock avalanche (RA) deposits

Clusters of large boulders are a diagnostic criterion for identifying RA deposits. Based on detailed boulder mapping, we delineated several RA deposits in the RP Valley, at Arsine Pass and, in the TA Valley, all framed or in contact with glacial deposits [Fig. 3]. At the western glacier branch (RP Valley), the most distal deposit lies in the footprint of the RP3 moraine complex. The lobate front is constrained by both moraines RP3 and RP2 indicating these landforms acted as barriers to the RA flow [Fig. 6a]. In the frontal area of this here called RA1 deposit, longitudinal flowbands, which are indicators of flow direction [Dufresne and Davies, 2009; Shugar and Clague, 2011], are not running parallel to the valley axis but are oriented WNW [Fig. 6a]. They are up to 2-m high with respect to the deposit's surface [Fig. 6a]. Well-defined trains of debris are also present in the distal sector. These features are usually emplaced in the lee of huge boulders [Delaney and Evans, 2014]. The most distal of these debris trains was diverted by the RP2 ridge (as shown by a short debris-free gap corresponding to the RP2 moraine distal face) and becomes subparallel to flowbands in the terminal area [Fig. 6a]. The delineation of the RA1 deposits mantling the RP valley floor between the RP1 and RP3 moraines, including the areas covered by slope deposits, gives a surface area of c. 0.20 km² [Fig. 3]. Combining the two methods described in Section 3.4 [see Fig. 6a, inset, for the cross profile method], we obtain a volume of c. $\mathbf{1.2 \pm 0.6 \times 10^6\ m^3}$ [Tab. 3]. Taking porosity into account, this translates into a minimum bedrock volume of c. $\mathbf{0.8 \pm 0.4 \times 10^6\ m^3}$ for the RA1. For this event, we tentatively propose a source area at c. 2820 m a.s.l. on the north buttress of 'point 2996' m a.s.l. located on the crest delimiting the Dragon Valley to the south [Fig. 3]. This implies a marked excessive runout for this event (H/L: 0.27) [Tab. 3] in relation to its estimated volume [Deline et al., 2021].

TABLE 3. Characteristics of the Early Holocene rock avalanches (RAs) at Arsine Glacier.

At the eastern glacier branch, two main RA deposits, grouped here as RA2, frame the aRG landform [Fig. 3]. They were emplaced outside of the existing glacier at that time and show chaotic topography without fluctuation lobes. One is located in lateral position and encompasses the Arsine Pass area (2340 m a.s.l.) with an area of 0.1 km² [Fig. 6b]. The other one is located at the head of the Tabuc Valley (2250 m a.s.l.) and occupies a similar area [Fig. 3]. It is highly dissected by streams and partly buried by alluvial deposits. Our estimate based on reconstructed valley floor is c. **0.6 ± 0.1 × 10^6 m^3** [Tab. 3]. Contrary to the Tabuc Valley deposit, the Arsine Pass deposit features a more pristine aspect and sharp delimitation, especially at its northern limit on the counter slope [Fig. 6b]. The Arsine Pass deposit can be divided into two distinct units, a western and an eastern one. Both units feature clearly identifiable longitudinal ridges with average strikes of N8°W, diverging towards the edge of their respective extent [Fig. 6b]. The western unit is shallower and its estimated volume is c. **0.2 ± 0.1 × 10^6 m^3** [Tab. 3]. Longitudinal ridges are more clearly defined on this unit. It also features a distinct spatula-shaped lobe with prominent outer levees and an inner depression in the front area [Fig. 6b]. The eastern unit is much thicker and has a more rounded and even topography. It displays mega-boulders up to 15 m in length and its estimated volume is c. **0.4 ± 0.2 × 10^6 m^3** [Tab. 3]. These morphological differences between both units likely arise from melting of different ice content. Clearer signs of a pristine deposit are present at the western unit, suggesting a limited initial ice content, whereas it may have been greater in the eastern unit. Possible slight overriding of the western unit by eastern one indicates a slightly younger age for the latter [Fig. 6b]. Four mega-boulders were sampled in the eastern unit (ARS-16-11 to -14). After removal of an old outlier (ARS-16-14 at 14.56 ± 0.95 ka) based on the reduced chi-squared test, the three remaining statistically consistent ages (10.69 ± 0.60 ka, 11.81 ± 0.49 ka and 11.89 ± 0.69 ka) yield a mean age of **11.48 ± 0.53 ka**. As the RA2 deposition necessarily occurred after the retreat of the glacier from the 'Inner complex' (RP2/TA2 moraines), both located further down-valley and dated here to **11.10 ± 0.37 ka**, the real age of the RA2 deposit is most likely a few hundred years younger. The slight age overestimation is probably due to an inherited ^{10}Be component accumulated during the Last Glaciation. High-elevation rockwalls are less prone to frequent refreshing during a glacial period, thereby favouring nuclide buildup. Our preferred approximation of the event age results from the Bayesian age model, which produces an age of **10.71 ± 0.42 ka** (unit 3) [Fig. 5]. This is consistent with studies showing that the youngest ages in RA deposits are more likely to be close to the true age of the event

[Akçar et al., 2012; Hilger et al., 2019; Delgado et al., 2025]. For the RA2 event, the tentative location of the source area is high up the headwall, on the western ridge of Calotte des Agneaux at c. 3405 m a.s.l. The mobility index computed for the RA2 event (H/L: 0.30) in relation to its volume [Tab. 3] is consistent with an RA that has partially travelled onto a glacier [Deline et al., 2021].

FIGURE 6. Geomorphological maps of the two main rock avalanche (RA) deposits in the study area (same key as Fig. 3). **(a)** The Rif de la Planche RA deposit (RA1 event) with main morphological features highlighted. In the upper panel, the white arrows point to the front of the RA1 deposit, and the cross profile runs through the distal area (inset) enclosed by the RP3 frontal moraine, **(b)** The Arsine Pass western and eastern RA deposits (RA2 event) with main morphological features highlighted. In the upper panel, the white arrows point to a spatula shaped frontal lobe. The blue arrows point to the small Neoglacial composite frontal moraine ('PMC W. outer frontal lobe') that has preserved the inherited aRG topography underneath. In the lower panels, violet lines represent longitudinal ridges. Lambert 93 Grid in meters (tick marks spacing is 100 m).

4.2.4. 'Apparent rock glacier' (aRG)

The landform east of Arsine Pass – herein called aRG – is a large (max. length: 780 m, max. width: 760 m, uncovered area: 0.40 km²), tongue-shaped and gently dipping (average slope: 19°) body, spanning 2270 to 2400 m a.s.l. [Fig. 7c]. Its complex topography partly resembles the classical transverse ridges-and-furrows rock glacier morphology (visible at nearby Réou d'Arsine relict rock glacier). It was previously mapped either as a fossil/relict rock glacier, consistent with its elevation range [Lahousse and Guen, 1998; Marcer et al., 2017], or as a moraine complex [Antoine and Fabre, 2000]. The evenly-spaced (100 m) front height measurements (n = 14) carried out along the western and frontal ridges (the eastern one is partly buried by slope deposits) give an average of 21.4 ± 4.1 m and a volume of c. 8.6 ± 1.6 × 10^6 m^3 [Fig. 7d]. The two DEM differencing methods yield a mean thickness of 30.0 ± 4.4 m and a volume of c. 12.0 ± 1.7 × 10^6 m^3 [Fig. 7d]. Conservatively combining the three methods, we obtain a volume of **10.9 ± 2.3 × 10^6 m^3**, which translates into a bedrock volume of c. **7.6 ± 1.6 × 10^6 m^3** for the aRG, taking porosity into account [Tab. 3].

According to our interpretation, the RA2 fell partly onto the glacier and was later deposited as moraine lobes by a heavily debris-covered glacier – forming the aRG. These ridges have been

likely affected by creeping after their deposition, possibly due to (i) periglacial processes, (ii) ice-core melting, and/or (iii) compression due to a remaining component of glacier flow. The main characteristics of this landform that support this view are as follows:

- The presence of extensive rock avalanche deposits, with mega-boulders, framing the landform, (i) at Arsine Pass, (ii) at the head of Tabuc Valley, and (iii) immediately outboard the right lateral moraine (RLM) around 2560 m a.s.l. [Fig. 3; Fig. 7b].
- The notable steepness of the ridge's distal faces [Fig. 7a,c], which is a diagnostic criterion for moraines formed by dumping of abundant supraglacial RA material [Shulmeister et al., 2009], but also for ice-cored moraines [Crump et al., 2017].
- The high frequency of large capping boulders on the outer ridges (TA1a-b moraines). Conversely the inner ridge (TA1c moraine) bears almost no large boulders [Fig 7b].
- The outcropping boulders are embedded in a glacial till-type diamicton.
- Three main generations of ridges are expressed in the morphology (some overriding older ones), reflecting an increasingly narrow and retreating glacier front [Fig. 7a].
- The well-defined nested lateral ridges on the eastern side run parallel and can be traced up to their distinct roots buried by the PMC [Fig 7a].
- Two small lateral ridges are present on the western side [arrow on Fig. 7a], the innermost displaying a 'balanced' mega-boulder, which is not conform to a rock glacier margin. These small outer moraines are cross-cutted by the main aRG outer ridge dated here (TA1a moraine), implying an immediately earlier deposition.
- Marked depressions, barely filled by outwash, exist inboard the inner ridges (TA1c moraine), likely the imprint of a former bilobate glacier front or massive ice-cores [Fig. 7c].
- No equivalent landform has formed on the RP (western) lobe of the glacier, despite a similar setting, highlighting a contrasting debris supply. This could be due to the fact that the deeper eastern part of the valley floor helped channel the RA2 flow.

On the outermost left-lateral ridge of the aRG (TA1a moraine), five boulders were sampled (ARS-16-06 to -10). The exposure ages increase downstream, from 9.42 ± 0.69 ka to 11.61 ± 0.49 ka, yielding a mean age of **10.63 ± 0.70 ka**. As the two oldest ages overlap with the mean ages of moraines RP5, RP2 and TA2, in older stratigraphic positions, we assume that they both reflect a small inherited ^{10}Be concentration. A similar amount of inherited ^{10}Be is probably present in two of the boulders in the RA2 deposit (ARS-16-12 and -13, section 4.2.3) [see Fig. 5]. This may support the proposed hypothesis that the boulders of these two landforms have the

same origin, the RA2 event. The youngest age on the TA1a moraine overlaps with the mean age of the TA1c moraine (see below) and is therefore considered 'too young'. The most probable age of stabilization of the aRG outer ridge (TA1a moraine), resulting from the Bayesian age model is **10.25 ± 0.42 ka** (unit 4) [Fig. 5], which is in agreement with the two remaining consistent ages (10.35 ± 0.40 and 10.32 ± 0.41 ka).

On the innermost ridge of the aRG (TA1c moraine), three boulders were sampled (ARS-16-01 to -03). A young outlier, whose age is likely underestimated due to exhumation of this short boulder, has been discarded based on the reduced chi-squared test (ARS-16-03 at 7.76 ± 0.28 ka). The two remaining consistent ages (9.69 ± 0.60 ka and 9.51 ± 0.41 ka) yielded a mean age of **9.57 ± 0.08 ka**, and a Bayesian-age-model-corrected age of **9.52 ± 0.43 ka** (unit 5) [Fig. 5].

FIGURE 7. 'Apparent rock glacier' (aRG) morphological features. (a) Structure-from-Motion DEM (0.26 m) of the aRG and longitudinal/transversal profiles highlighting the three generations of moraine ridges. Nested lateral ridges and overriding ridges are highlighted with arrows, **(b)** Boulder map (> 2 m²) of the aRG, Arsine Pass and Tabuc RA deposits. The continuous aRG rocky carapace is shown as light grey, **(c)** Slope map of the aRG based on the Structure-from-Motion DEM (resampled to 1 m resolution), **(d)** aRG thickness map based on DEM differencing (DoD). Manually reconstructed valley floor paleo-topography is shown as 20 m contour lines. Lambert 93 Grid in meters (tick marks spacing is 300 m).

4.2.5. Proximal Moraine Complex (PMC)

The most proximal part of the glacier forefield is characterized by a prominent complex of composite moraines made of fresh-looking (mostly unvegetated) till [Fig. 2]. The lateral moraines display an arcuate shape and have lengths of c. 1.5 km protruding 15-70 m from outboard terrain, while the frontal moraine reaches heights of 80-100 m, overtopping parts of the aRG landform [Fig. 2]. The lateral moraines are partly multi-crested over lengths of 150 m for the left-lateral moraine (LLM) and 280 m for the right-lateral moraine (RLM) [Fig. 2b], and display several generations of accretion on some parts of their outer slopes [Fig. 8].

At the LLM, most of the external parts were overtopped during younger advances, as evidenced by the light grey till on the distal face. Three limited sectors are exceptions [Fig. 3]. Starting upstream, the first sector is a subdued ridge located mid-slope, 12 m below main crest [Fig. 8a], which bears the boulders of samples ARS-12-04b and ARS-19-04 yielding ages of 2.46 ± 0.12 ka and 2.00 ± 0.08 ka, respectively. The second sector is a small isolated patch of slightly

vegetated till, lying 18 m below the main crest, which bears the boulder of sample ARS-19-05 dated to 2.59 ± 0.11 ka [Fig. 3]. The third sector features two well-defined small ridges sitting on top of the LLM and located 7 and 13 m outboard the main (eroded) LIA crest [see Fig. 2b; Fig. 8b]. On the distal side of the most prominent outermost ridge ('PMC LLM outer crest'), two further boulders (ARS-19-06 and -07) were sampled 9 and 13 m below the main crest, yielding ages of 2.83 ± 0.12 ka and 2.28 ± 0.07 ka, respectively. Together, the five boulders from the distal face of the LLM were considered a common unit as sharing a location defined by a depression 13 ± 4 m below the main (eroded) LIA crest. They give a mean age of **2.62 ± 0.15 ka** after the exclusion of the two youngest ages (ARS-19-04 and -07) according to the reduced chi-squared test. Of interest, the furthest downstream of the young outliers (ARS-19-07 at 2.28 ± 0.07 ka), despite its stratigraphically discordant position (4 m lower in the distal face than ARS-19-06 dated to 2.83 ± 0.12 ka), could also mark a younger advance, as it is unlikely to have been exhumed. This advance could coincide with the one that deposited two boulders (ARS-18-01 and -02) of the frontal composite moraine (see Section 5.7).

Finally, on the most prominent (130 m long) and outermost of the two small ridges of the third sector ('PMC LLM outer crest') [see Fig 2b; Fig. 8b], four boulders were dated (ARS-19-01, -02, -03, -08). Three of them were sitting on the crest and one was embedded 6 meters below the crest in the distal face. The exposure ages range between 1.62 ± 0.06 ka and 1.86 ± 0.08 ka and result in a mean age of **1.67 ± 0.05 ka** after the exclusion of the oldest age (ARS-19-01) according to the reduced chi-squared test. The oldest boulder stood on the crest 70 m north of the others, which were tightly grouped.

FIGURE 8. Proximal Moraine Complex (PMC) dated moraine units. Cross profiles [see Fig. 3 for location] through the **(a,b)** PMC left-lateral moraine (LLM), **(c,d)** right-lateral moraine (RLM) and **(e)** frontal moraine, with main TCN dating results. The profile **(e)** does not conform to the former glacier flowline between the 1892-1930 CE moraines and the 2015 CE front, and therefore does not reflect the actual ice margin retreat over this interval [Fig. 3]. The arrangement of the different till units (especially the undated ones) reflects in part an interpretation and cannot be considered entirely accurate. Units marked with question marks do not have dating control. Note that on the profile **(d)**, no inner ridges posterior to 2.7 ka have been preserved. LAAP: Late Antique Advance Period, IAAP: Iron Age Advance Period, BAAP: Bronze Age Advance Period [see Le Roy et al., 2024 for the nomenclature of glacier advances]. The scale is the same on all panels (vertical exaggeration x3).

At the RLM, by contrast, only the upper (> 2580 m a.s.l.) and lower (< 2520 m a.s.l.) sectors of the main crest were overtopped during a younger period [Fig. 4b], as shown by the preservation of accreted inner ridges. Some of these inner ridges still existed during the early 20th century [see Fig. 2b], but have since then disappeared. In the middle part of the RLM, several generations of moraine accretion are visible, either from distinguishable layers on the distal slope or from multiple preserved crests [Fig. 4b; Fig. 8c,d].

The outermost moraine position recorded at the PMC is represented by a 'bouldery ridge' located in the lower half of the RLM distal face ('PMC RLM distal face-Mid.') [Fig. 3; Fig. 4b]. The three boulders sampled on this ridge are located 46 ± 5 m below the main crest and c. 25 m above the moraine base [Fig. 4b; Fig. 8d]. They gave ages of 9.78 ± 0.37 ka, 10.52 ± 0.33 ka and 10.92 ± 0.33 ka (ARS-16-24, ARS-12-08 and ARS-16-24), yielding a mean age of **10.72 ± 0.20 ka**, after exclusion of the youngest sample according to the reduced chi-squared test. The mean age of this boulder-rich ridge overlaps with the non-modelled mean ages of RP2 (**10.88 ± 0.25 ka**) and TA2 (**11.08 ± 0.25 ka**). It could thus correspond to the former right lateral moraine crest of the 'Inner complex' stadial. This appears likely given that (i) the slightly younger age can be explained by the much more sheltered location of this ridge, (ii) the geometry corresponds to the upstream route of TA2, and (iii) no other ridges are preserved outboard at this location [Fig. 9a]. This way, the last important EH advance would have overtopped them in lateral position [Fig. 8d]. Alternatively, as the age of this ridge overlaps with the modelled age of RA2 (**10.71 ± 0.42 ka**) and that its location is on the presumed path of RA2, it could represent RA material deposited on top of pre-existing moraine or dumped during an early stage of a RA2-triggered advance. We have not retained this hypothesis, as none of the three samples show any inheritance and they are well anchored in till. We therefore included this surface in the 'Inner complex' stadial, whose Bayesian modelled age is **11.10 ± 0.37 ka** [Fig. 5]. In this scenario, the lateral moraine deposited by the RA2-triggered advance that created the TA1a frontal moraine would lie in more internal position here [see Fig. 8d].

In another accreted layer further up on the same distal face, three boulders were sampled in the upper unit of the RLM, as their location averages 9 ± 6 m below the main crest. They gave ages of 3.76 ± 0.12 ka, 3.71 ± 0.12 ka and 3.11 ± 0.10 ka (ARS-19-10 to -12), yielding a mean age of **3.74 ± 0.02 ka** after exclusion of the youngest sample according to the reduced chi-squared test [Fig. 4b; Fig. 8c,d]. On the main crest of the RLM [Fig. 2b], three more boulders provide consistent ages of 2.67 ± 0.22 ka, 2.70 ± 0.11 ka and 2.86 ± 0.11 ka (ARS-12-06, ARS-16-19

and -20), yielding a mean age of **2.76 ± 0.08 ka** [Fig. 4b; Fig. 8c,d]. Finally, three boulders from the next immediately inboard and only slightly protruding crest ['Outer LIA ridge' on Fig. 4b] yielded exposure ages of 0.58 ± 0.04 ka, 0.17 ± 0.03 ka and 0.16 ± 0.04 ka (ARS-16-21, -22 and -23) [Fig. 4b]. Given that (i) a more prominent LIA crest (not sampled) is present further inboard [inner arrow on Fig. 2b; 'Inner LIA ridge' on Fig. 4b], and (ii) the large size of the two youngest boulders, excluding exhumation as a rejuvenation factor, two scenarios are possible. First, this ridge may have been deposited at **0.17 ± 0.01 ka** and reworked an early-LIA-aged boulder. In this scenario, two close LIA ridges would have been deposited at 0.17 ka and shortly afterwards [Fig. 4b; Fig. 8c]. Another interpretation would be that the 'Outer LIA ridge' is an actual early-LIA ridge to which two younger boulders have been added during the initial phase of a subsequent advance (represented by the innermost ridge, not sampled). In this case, the 'Inner LIA ridge' would be dated to 0.17 ka [inner arrow on Fig. 2b; Fig. 4b].

In the frontal area of the PMC, three clearly distinct generations of ridges are visible on the distal slope [Fig. 2a; Fig. 8e]. The outermost one has been deposited perpendicularly on top of lateral ridges of the aRG, as demonstrated by the thin mantle of till that has preserved the inherited topography underneath [see Fig. 6b; Fig 8e]. In total, 8 boulders were dated from two sectors of the outer lobes in the frontal area. In the western sector ('PMC W. outer frontal lobe'), six boulders yielded dispersed ages of 8.17 ± 0.23 ka (ARS-16-16), 2.13 ± 0.21 ka and 1.79 ± 0.21 ka (ARS-18-01 and -02), and 0.66 ± 0.04 ka, 0.59 ± 0.08 ka and 0.85 ± 0.04 ka (ARS-16-17, ARS-18-03 and ARS-19-15, respectively). The first three ages were not considered in the calculation of the mean age of this moraine. The last three ages provided a mean age of **0.65 ± 0.03 ka** for the last occupation of this position, after exclusion of a slight old outlier [the ARS-19-15 mega-boulder, see Fig. 2a] according to the reduced chi-squared test. In the eastern sector ('PMC E. outer frontal lobe'), two boulders gave clearly distinct ages of 1.17 ± 0.05 ka and **0.50 ± 0.04 ka** (ARS-19-13 and -14). The youngest one is considered as dating the last occupation of the eastern outer lobe, in accordance with the mean age obtained on the western lobe.

Although undated at this frontal location (but dated in lateral position), the innermost set of the three ridges on the frontal distal slope [Fig. 8e] was selected as representing the last LIA position during the 19th century (1850 CE) used for ELA calculation. It is based on the classical threefold LIA Alpine chronology, with maximum glacier advances occurring during the 14th, 17th and 19th centuries [Holzhauser et al., 2005; Schimmelpfennig et al., 2014; Fouinat et al.,

2017; Nicolussi et al., 2022]. We assume they are represented by the three LIA frontal moraines present here [Fig. 2a; Fig. 8e; Fig. 9a].

FIGURE 9. **Paleo-glacier extents, ice thickness and ELAs for the three main reconstructed stadials of Arsine Glacier.** Greyscale depicts the paleo-ice thickness. Paleo-glacier surface elevation is shown as 50 m-spaced contour lines. Fronts elevations of the reconstructed stadials are given (black) along with the corresponding ELAs computed with the Area-Altitude-Balance-Ratio (AABR = 1.3) method (red). The Maximum Elevation of the Lateral Moraine (MELM) is also indicated (orange). Bed elevation is based on Echevin [1970] and Antoine and Fabre [2000] for the PMC area, **(a)** The three reconstructed stadials are shown with the mapped moraine ridges used to delineate them. Note the three distinct LIA frontal moraine sets, **(b)** The 'Outer complex', **(c)** The 'Inner complex', **(d)** The late-LIA position (1850 CE). The AABR ELA indicated in **(d)** for the LIA is the weighted average for the three former tributaries [see Tab. 4]. Lambert 93 Grid in meters (tick marks spacing is 1 km).

4.3. ELA modelling

The ELA results for the two methods are given in Table 4. Based on our mapping and geometrical reconstructions we can also propose maximum elevation of lateral moraines (MELM) values for four stadials, assuming our moraine attribution and glacier outline delineation are correct in areas close to the ELA [see Fig. 3 and Fig. 9]:

- 2465 m a.s.l. for the undated RP7 stadial, based on moraine remnants located on a structural flat north of Arsine Pass. This gives a minimum value for the RP5 stadial ELA and a robust lower bound for ELAs of all the stadials mapped here. We tentatively link RP7 to the YD maximum and propose a *maximum* δELA of 335 m for this stadial (not reconstructed here) [Fig. 9b].
- 2525 m a.s.l. for the RP5/TA5 (i.e., 'Outer complex') moraine set at Réou d'Arsine. This is the innermost of a close moraine doublet mapped in this area [Fig. 9b].
- 2580 m a.s.l. for the RP2/TA2 (i.e., 'Inner complex') moraine set immediately outboard the RLM [Fig. 9c].
- 2790 m a.s.l. for the late-LIA (1850 CE) at the LLM [Fig. 9d].

It is worth stressing that for the Outer and Inner complexes, the AAR of 0.54 we used agrees with MELM values, while an AAR of 0.67 conflicts with them [Tab. 4]. This confirms the relevance of the AAR of 0.54 for Arsine Glacier during the EH. It must be stressed that steady-

state AARs can also be expected to vary through time at a single glacier system, depending on change of the debris-cover area and of firn basins geometry [Clark et al., 1994]. This was undoubtedly the case at Arsine between the Early- (presence of a proper accumulation area) and the Mid- (likely heavily debris-covered ice patch) to Late Holocene (mostly debris-free cirque glacier).

On the other hand, when it comes to the LIA 1850 CE position, all methods significantly underestimate the minimum ELA indicated by the MELM method for the Arsine Glacier *stricto sensu*, but not for the former tributaries. For the LIA 1850 CE position, the AAR that would conform with the MELM estimate is around 0.32 for the Arsine Glacier *stricto sensu*, highlighting the peculiar accumulation processes influenced by the snow contribution from the headwall. For 1850 CE, our preferred weighted average of 2802 m a.s.l. for Arsine and former tributaries [Tab. 4] is consistent with recent glaciological modelling yielding c. 2787 m a.s.l. for this stadial [Henz et al., 2024]. The AABR of 1.3 and AAR of 0.54 yielded quite similar results with δELA of 224 ± 10 m and 234 ± 10 m for the 'Outer complex' and 169 ± 10 m and 159 ± 10 m for the 'Inner complex', thus increasing our confidence in the results [Tab. 4].

To remain consistent with other studies, we only refer in the following Discussion section to ELAs calculated with the AAR method. However, the large underestimation of the true ELA (whose lower limit is given by the MELM) induced by using the 0.67 ratio at Arsine Glacier (see Section 4.3) would argue in favour of abandoning this method and computing ELAs based on the AABR method for cross-comparison purposes. Such discrepancies are evident from the EPM-wide LIA ELAs reported in Section 2.1, and at other Alpine location, e.g., at Goldberg Glacier (Hohe Tauern, Austrian Alps), both for the LIA and Egesen stadials [Bichler and Reindl, 2013].

Table 4. Characteristics and paleo-ELAs of the three main reconstructed stadials of Arsine Glacier. The paleo-ELAs are calculated using two different methods (AABR and AAR). The ELAs marked in italics are computed values that conflict with independent evidence (MELM method). Note that the AAR of 0.67 yields no suitable estimate for any of the stadials. The ELAs marked with asterisks are the values used to compute the 'LIA 1850 CE' weighted average. The ELAs marked in bold are the values retained for the Discussion section. The MELM values are rounded up to the nearest 5 m. The uncertainty amounts to ± 5 m for the computed ELA values and ± 10 m for the δELA values.

5. Discussion

5.1. Climatic correlation of the Arsine Glacier chronology

The EH cold pulses that could have been recorded by Alpine glaciers are concomitant with the Greenland Preboreal Oscillation at 11.4–11.25 ka [Rasmussen et al., 2007] and the Boreal Oscillation at 10.3 ka [Björck et al., 2001; Young et al., 2020]. The central European PBO (**11.25** to **11.10 ka**) has been found to slightly lag the Greenland PBO (**11.37** to **11.27 ka**) when aligned on the same timescale [Mekhaldi et al., 2020]. This small shift additionally revealed solar activity as a possible trigger for this event when superimposed on freshwater forcing. Probable solar forcing on central European paleohydrology is also reflected by the occurrence of two prominent EH humid periods centred on 11.5 and 11.2 ka [Magny et al., 2007; Prochnow et al., 2024]. Annual precipitation during the EH is assumed to be comparable to the mid-20th century, and much higher than during the late YD [Kerschner et al., 2000; Magny et al., 2007; Ortu et al., 2008; Hepp et al., 2019; Rea et al., 2020; Prochnow et al., 2024], including near our study site [Francou et al., 2020]. At the nearby Lautaret Pass, the YD/EH boundary is marked by inactivation of two rock glaciers (c. 2050 m a.s.l.) at **11.95 ± 0.92 ka** (RG1; n = 5) and **11.70 ± 0.29 ka** (RG2; n = 5) [Charton et al., 2021] [Fig. 1]. This inactivation falls within – or just after – the deposition of moraine RP5a at Arsine. The RG2 is a small protalus rock glacier, which means that frost-shattered debris supply ended at this elevation (headwall: 2250-2300 m a.s.l.) at the beginning of the Holocene. At the same period, the first occurrence of trees is attested at the pass, associated with geothermal springs [Carcaillet et al., 2018]. Increase in humidity at the YD/EH boundary may have partly counteracted the rise in mean annual air temperature (c. 5 ± 1°C) over these few decades [Affolter et al., 2019; Li et al., 2021]. This may explain why early Preboreal glacier extents (Arsine 'Inner complex') were still large and close to those of the late YD (Arsine 'Outer complex'). At the same time, the rise in summer temperature was more moderate (c. 3.5 ± 1°C) [Ilyashuk et al., 2009; Samartin et al., 2012; Lapellegerie et al., 2024], implying milder and snowier EH winters. Recent improvements in ice core chronology also show that the third largest Holocene volcanic eruption occurred around **11.23 ka** (9226 BCE) [Sigl et al., 2022] [Fig. 10h] and could have been an additional trigger for the PBO glacier advance. Our dating result for the Arsine 'Inner complex' (RP2/TA2/PMC RLM-Mid. moraines) at **11.10 ± 0.37 ka** is therefore consistent with a deposition during the central European PBO.

Following the early Preboreal, HTM-like summer conditions were reached shortly after 11 ka, as shown by smaller-than-present (2020 CE) glacier extent, evidenced before **10.80 cal ka**

[Nicolussi et al., unpublished] [Fig. 10b]. This is further demonstrated by (i) the disappearance of glacial varves in Lake Silvaplana at **10.70 cal ka** [Leeman and Niessen, 1994], (ii) a major tipping point in fire frequency at **10.70 cal ka** in the Western Alps [Carcaillet and Blarquez, 2017], and (iii) among the highest Holocene $\delta^{18}O$ values recorded from **10.48 ka** in high-elevation speleothems [Fohlmeister et al., 2013], all hinting towards an already warmed climate. At the Alpine scale, this is consistent with the absence of prominent EH glacier advances firmly dated to later than ~11 ka and with glacier fronts retreating inboard their LIA limit afterwards [Böhlert et al., 2011; Schindelwig et al., 2012; Schimmelpfennig et al., 2012; 2014; Hofmann et al., 2019; Protin et al., 2019; 2021; Steinemann et al., 2021; Braumann et al., 2020; 2021].

The only exception is a cluster of ages on moraines located only slightly outboard the LIA extent at small to medium glaciers, tracing the response to the cold/wet Boreal Oscillation (BO), also known as the '10.3 ka event' or the 'CE-1' phase [Haas et al., 2008; Boch et al., 2009; Schmidt et al., 2009; Belli et al., 2013; Joannin et al., 2013; Magny, 2013]. The most precise dating of this event is an excursion centred on **10.25 ka** in an Austrian speleothem [Fohlmeister et al., 2013]. A causal link might therefore be drawn between this cold/wet event and the deposition of the Arsine Glacier TA1a moraine ridge (and possibly the undated RP1) at **10.25 ± 0.42 ka**, and more generally with the deposition of 'Kromer-equivalent' moraines in the Alps.

Finally, shortly before 10 ka, air temperature was at the level of HTM peak warmth in the Alps and contiguous regions [Ilyashuk et al., 2011; Fohlmeister et al., 2013; Heiri et al., 2015; Affolter et al., 2019; Martin et al., 2020a; Zander et al., 2024] as evidenced by trees growing in glacier forefields from ~10.2 ka [Nicolussi, 2011; Nicolussi et al., 2020; Le Roy et al., 2024].

FIGURE 10. Synthesis of TCN-dated moraine boulders at Arsine Glacier in the context of the Alpine Holocene glacial and paleoclimatic history. (a) Mean annual air temperature (MAAT) reconstructed from fluid inclusions in speleothems of the Milandre Cave (Jura Mountains, Switzerland) [Affolter et al., 2019] with mention of the three Holocene Thermal Maximum (HTM) Phases proposed by Le Roy et al. [2024], as well as the Holocene cold periods. BO: Boreal Oscillation, **(b)** Tree-ring dated glacier-borne subfossil wood dates constraining glacier evolution in the Alps. The dark orange curve represents all tree-ring-dated wood samples (n = 211) coming from ice-proximal parts of glacier forefields (mostly floodplains) in the Alps and indicating a glacier extent smaller than 2000-2020 CE at the time of tree growth. The light orange curve represents all tree-ring dated wood samples (n = 439)

coming from distal parts of the glacier forefields (lateral moraines) in the Alps and pointing to a glacier extent smaller than 1850-1960 CE at the time of tree growth [see Le Roy et al., 2024 for details and Nicolussi et al., unpublished]. Note that no lateral moraine wood samples are older than 4 ka. The blue curve represents Kernel Density Estimates of all the TCN ages measured on Holocene moraine boulders in the Alps (n = 282; including data of this study). Note that all TCN-dated periods of moraine stabilisation are synchronous with – or slightly postdate – tree-ring dated subfossil trees dying-off phases (direct dating of glacier advances) during the Neoglacial, **(c)** Kernel Density Estimate of TCN-dated boulders of Holocene moraines in the Alps (n = 242; sites shown in Fig. 1 inset; data of this study not included). All moraines considered to belong to the time span covered by the Arsine chronology were included. We applied the same detection of outliers as used in this study, and therefore potentially excluded certain samples retained in the original publications, **(d)** Variations of the Upper Grindelwald Glacier ice surface reconstructed from speleothems of the Milchbach Cave (Bernese Alps, Switzerland) [Luetscher et al., 2011], **(e)** Kernel Density Estimates of TCN-dated boulders of Holocene moraines at Arsine Glacier (n = 40), **(f)** TCN-dated high elevation rock avalanches in the Ecrins massif (release area > 2100 m a.s.l.) plotted against their estimated volumes. As the Arsine RA1 is not numerically dated, we have assigned it here an age in line with the stratigraphy (11.0 ± 0.4 ka), i.e., immediately after the deposition of the RP2 moraine (see Section 5.3.1), **(g)** Activity phases of the Vallon de la Route rock glacier (Combeynot massif) defined as the evolution of the rock glacier surface velocity in time based on modelling of TCN data [Lehmann et al., 2022], **(h)** Holocene volcanic stratospheric sulfur injection (VSSI) from explosive eruptions. Main eruptions linked to dated glacier advances are indicated with their ranking [Sigl et al., 2022]. The background bands represent the TCN-dated glacier advances at Arsine Glacier (grey), tentative dated advances (light grey) and aRG dated ridges (brown). For the sake of clarity, only ± 100 yr uncertainty is shown.

5.2. Lateglacial to Early Holocene glacier activity in the Alps

5.2.1. Key comparable glacier chronologies in the Western Alps

The Arsine Glacier RP branch experienced five oscillations between ~11.9 and 11.1 ka. The first two (RP5a-b positions) probably occurred at the end of the YD, while the latter three (RP4-2 stadials) likely occurred during the Early Holocene (Preboreal chronozone). During this period, the net frontal retreat amounted to 880 m, but the ELA rose only by c. 55 m (or 75 m based on the AAR method) [Tab. 4]. The three main dated stadials of the Arsine chronology

1120 are paralleled at several sites in the western Alps, demonstrating these were the main periods
1121 of moraine deposition regionally.

1122 In the southwestern Alps, our chronological and ELA data are similar to those derived at three
1123 sites. In the Rougnoux Valley (25 km south of Arsine) [Fig. 1], after deposition of the M7
1124 moraine (δELA c. 194 m), which occurred no later than **11.80 ± 0.40 ka**, the glacier front
1125 retreated stepwise by 470 m to the innermost pre-LIA M4 moraine (δELA c. 164 m), which
1126 was abandoned no later than **10.90 ± 0.70 ka**. Consistently, in the neighbouring Prelles Valley,
1127 the former glacier withdrew no later than **10.90 ± 0.60 ka** from one of its pre-LIA positions,
1128 the M7 moraine (δELA c. 158 m) [Hofmann et al., 2019]. In the Clarée Valley (15 km NE of
1129 Arsine) [Fig. 1], one stadial of regional significance ('Stage 4') with reported δELAs averaging
1130 c. 130 m, was TCN-dated to **10.82 ± 0.70 ka** (n = 4; 2 outliers) at the former Muandes Glacier
1131 [Cossart et al., 2012]. In the Belledonne massif (40 km NW of Arsine), the M3 moraine of the
1132 Tepey Glacier yielded a δELA of c. 150 m and was dated to **10.97 ± 0.59 ka** (n = 3), as a likely
1133 response to the PBO, while the M2 moraine, characterized by a δELA of c. 70 m, was dated to
1134 **10.62 ± 0.53 ka** (n = 2) and may have been triggered by the Boreal Oscillation [Le Roy, 2012;
1135 Le Roy et al., 2024].

1136 In the northwestern Alps, three chronologies mirror the Arsine chronology in the Mont Blanc
1137 massif. At the Tour Glacier, two radiocarbon dates from lacustrine and glacio-fluvial deposits
1138 gave minimum-limiting ages for two EH moraine sets [Jaillet and Ballandras, 1999]. The first
1139 moraine ('Frasserands stadial'), represents the youngest unit of the prominent Lateglacial
1140 moraine complex, which would predate ~11.5 cal. ka (median probability of the radiocarbon
1141 age), thus likely deposited around 11.2 ka. The second moraine ('Tour stadial'), is located
1142 midway between the Lateglacial and the LIA complexes and would predate ~9.5 cal. ka (median
1143 probability of the radiocarbon age), hence likely deposited around 10.3 ka. At the nearby
1144 Argentière Glacier, the lateral moraine sequence shows evidence of at least three oscillations
1145 and an overall thinning of the glacier tongue between **11.44 ± 0.73 ka** (n = 4; one outlier) and
1146 the two close innermost EH moraines dated to **10.52 ± 0.28 ka** (n = 3) and **10.38 ± 0.41 ka** (n
1147 = 5; one outlier) [Protin et al., 2019]. This is the only site in the Alps where two distinct
1148 moraines probably contemporary to the '10.3 ka event' are numerically dated. Finally, at higher
1149 elevation (c. 2800 m a.s.l., i.e., near the ELA), the close Talèfre Glacier deposited one moraine
1150 ridge at the end of the YD, at **11.90 ± 0.42 ka** (n = 3), and two moraines during the EH, the first
1151 one at **11.17 ± 0.28 ka** (n = 3; one outlier) and a second inner one (undated) located midway to
1152 the LIA, that could correspond to the '10.3 ka event' [Protin et al., 2021].

5.2.2. Comparison with the eastern and central Alps

We tentatively correlate the Arsine 'Outer complex' with an undefined oscillation at the end of the YD chronozone. With regard to the 'eastern Alps model', the corresponding advance was regionally defined as the Egesen II stadial ('Bocktentälli') [Maisch, 1981; Ivy-Ochs, 2015]. This sub-stadial is associated with an estimated δELA of c. 190-230 m in Tyrol [Sailer and Kerschner, 1999] and c. 240 m in Valais [Scapozza, 2013]. Although not firmly TCN-dated yet, it has been estimated to **11.66 ± 1.01 ka** (n = 1; one outlier) in the Val Mulix (Albula area, Switzerland) [Böhlert et al., 2011], but shows a much smaller reported δELA (c. 125 m) at this location [Maisch, 1981]. Based on the relative stratigraphy, it is possible that (i) the lateral moraine J5 (next ridge inboard the YD maximum lateral moraine), TCN-dated to **11.50 ± 0.29 ka** (n = 2) in the Jam Valley, and (ii) the frontal moraine doublet F5, TCN-dated to **11.41 ± 0.33 ka** (outer F5b, n = 1; one outlier) and **11.48 ± 0.35 ka** (inner F5a, n = 2; 2 outliers) in the Fimba Valley [Braumann et al., 2022] both correspond to this stadial. In the Fimba Valley, ages are probably underestimated given the low prominence of the moraines. In the central Alps, possible coeval stadials have been identified: the MT2 in the Meien Valley [Boxleitner et al., 2019b], and the main crest of the massive Lateglacial/EH left lateral moraine at Tsijiore Nouve Glacier, dated to **11.64 ± 0.35 ka** (n = 7; 3 outliers) [Schimmelpfennig et al., 2012].

The deposition of the Arsine 'Inner complex' probably took place during the PBO. In the Alps, the Kartell stadial, i.e., the Egesen III stadial [Maisch, 1987; Ivy-Ochs, 2015] has earlier been proposed to correlate with the PBO [Kerschner and Ivy-Ochs, 2008]. Morphostratigrafically, this stadial is easily identifiable as the innermost ridge of the large Egesen moraine complexes. It is characterized by an estimated δELA of c. 90 m in Val Viola [Scotti et al., 2017], 85-135 m in the Northern Calcareous Alps [Hirtlreiter, 1992; Moran et al., 2017a], 90-120 m in Tyrol [Fraedrich et al., 1979; Sailer, 2001; Moran et al., 2016b], 110-160 m in Silvretta [Hertl, 2001; Moran et al., 2016a] and up to 130-180 m in the western Alps [Schindelwig, 2010; Le Roy, 2012; Cossart et al., 2012]. It is often found to be immediately followed by a phase of rock glacier development [Cossart et al., 2012; Moran et al., 2017a], which has sometimes overprinted the Kartell moraines [e.g., Le Roy, 2012; Le Roy et al., 2024]. The Kartell stadial is now dated to **11.88 ± 0.46 ka** (n = 3) at the type locality (Ferwall Group, Austria) [Fraedrich, 1979; Ivy-Ochs et al., 2006b; Ivy-Ochs et al., 2009; Ivy-Ochs, 2015] with only the youngest age (**11.58 ± 0.60 ka**) overlapping with the PBO period. However, age control on 'Kartell-equivalent' moraines (δELA c. 120-180 m) at numerous sites spread over the entire Alps agrees

with the PBO timespan. In Tyrol, a 'Kartell-equivalent' stadial (δELA c. 120 m) has been dated at both Falgin and Hinteres Bergle cirque glaciers, and yielded mean deposition ages of **11.06 ± 0.61 ka** (n = 4) and **11.00 ± 0.39 ka** (n = 2), respectively [Moran et al., 2016b]. In the central Alps, a 'Kartell-equivalent' stadial identified in the Meien Valley, MT3 (δELAs of c. 120 to 300 m, latter value at a south facing cirque) yielded a mean age of **11.06 ± 0.57 ka** (n = 6) [Boxleitner et al., 2019b]. At the Stein Glacier, the EH outer moraine ('Hublen outer') is constrained by two bracketing mean ages of **11.50 ± 0.27 ka** (n = 2; roche moutonnée a few meters outboard) and **11.03 ± 0.28 ka** (n = 2; boulders slightly inboard) [Schimmelpfennig et al., 2014; 2022]. Similarly, the recessional ridges inboard the massive Lateglacial/EH left lateral moraine at Tsijiore Nouve Glacier are dated to **11.22 ± 0.29 ka** (n = 7) [Schimmelpfennig et al., 2012]. Finally, at Belalp, the 'moraine VI', which has a slightly younger mean age of **10.61 ± 0.30 ka** (n = 4), can still be considered as 'Kartell-equivalent' because (i) it is characterized by an estimated δELA of c. 179 m (south facing cirque) [Schindelwig, 2010] and (ii) it is the inner moraine of the Egesen/YD complex with a front only 100 m higher in elevation than the Egesen maximum [Schindelwig et al., 2012].

Finally, our estimate for the stabilization of the outer aRG ridge at **10.25 ± 0.42 ka** at Arsine Glacier eastern branch is synchronous with the deposition of 'Kromer-equivalent' moraines in the Alps. We also tentatively propose that a 'Kromer-equivalent' moraine (RP1, undated here) is present at the western branch [Fig. 6b; Fig. 11d]. The 'Kromer-equivalent' stadial moraines were identified at several sites and TCN-dated between ~10.5 and 10 ka [Le Roy, 2012; Schimmelpfennig et al., 2014; Scotti et al., 2017; Boxleitner et al., 2019b; Protin et al., 2019; Braumann et al., 2020; Le Roy et al., 2024]. Morphostratigraphically, they are found in intermediate position (midway) between the innermost moraine of the Egesen complexes (Kartell/PBO) and the LIA/Neoglacial moraines. At the most climate sensitive glaciers, they are characterized by two close but distinct ridges [Moran et al., 2016a; Le Roy et al., 2024]. Both ridges have only been numerically dated separately at Argentière Glacier [Protin et al., 2019, see above] and likely also at Stein Glacier (as the 'Hublen inner' and 'In Miseren' moraines, but stratigraphy is less clear), at **10.57 ± 0.32 ka** (n = 3) and **9.91 ± 0.38 ka** (n = 2; one outlier) [Schimmelpfennig et al., 2014]. The reported δELAs for this stadial are ranging from 47 to 80 m [Gross et al., 1977; Le Roy, 2012; Moran et al., 2016a; Scotti et al., 2017]. Since the disambiguation of the Kartell/Kromer stadials, it is known that the Kromer is one millennium younger [Ivy-Ochs et al., 2006b]. At the type locality, a mean age of **9.82 ± 0.34 ka** was obtained (n = 8; one outlier), but as this moraine is cross-cut by a rock glacier front

dated to **10.24 ± 0.54 ka** (n = 1), it is still considered a minimum age [Moran et al., 2016a]. Similar mean deposition ages for the Kromer stadial were obtained in the next two neighbouring valleys of the Silvretta massif: **9.85 ± 0.62 ka** (n = 3) in the Kloster Valley [Moran et al., 2016a] and **9.68 ± 0.34 ka** (n = 4) in the Ochsen Valley [Braumann et al., 2020].

Figure 11. Snapshots of Arsine Glacier evolution since the end of the Lateglacial. Each panel shows the reconstructed glacier extent for a given time period based on TCN dated surfaces and detailed geomorphological mapping. This holds true except for the 10.7 ka and the HTMPs, for which evidence of glacier minima is not preserved. For the 10.7 ka period in panel **(c)**, the extent of the glacier is based on evidence gathered elsewhere in the Alps [Nicolussi et al., unpublished]. In panel **(c)**, the two red dots indicate the proposed RA release areas. The debris cover extent for the 9.5 ka period in panel **(e)** is based on the 2015 CE state, in line with Nicolussi and Schlüchter [2012]. For the HTMP 2-3 period in panel **(f)**, the extent of the glacier (as of a potential proglacial lake dammed by the aRG) is hypothetical, but conforms with a smaller-than-present (2020 CE) extent, as demonstrated at multiple sites in the Alps [Le Roy et al., 2024]. The depiction of the evolution of the Réou d'Arsine rock glacier is inspired by reconstructed rock glacier evolution in the area [Lehmann et al., 2022]. In panel **(h)**, the shaded TCN ages denote possible glacier advances of the same extent (see Section 5.7) based on the composite frontal moraine with multimodal TCN age distribution ('PMC outer frontal lobes', see Fig. 3). Present-day (2015 and 2023 CE) glacier extent is reported on panel **(i)** as light blue and white areas. Lambert 93 Grid in meters (tick marks spacing is 1 km).

5.3. The rock avalanche and subsequent aRG development

5.3.1. Timing and emplacement of the Arsine rock avalanches

Based on our detailed mapping, at least two RAs occurred within Arsine Glacier's forefield during the EH. Both the RP and TA Valley floors are filled with extensive boulder fields [Fig. 3; Fig. 6; Fig. 7b]. The deposits located in the RP Valley likely belong to a single event, originating from a release area c. 2820 m a.s.l. (eastern crest of the Dragon hanging valley), as shown by the RA1 path that climbed the counter-slope before abutting on the two RP2 and RP3 frontal moraines [Fig. 6a; Fig. 11c]. The RA1 event therefore post-dates the RP2 moraine deposition. In order to explain (i) the distal landforms typical of ice/debris mixture [Fig. 6a], and (ii) the high mobility index in relation to its volume, we infer that the RA1 debris travelled partly onto the ice/snow. This means that it likely occurred shortly after the retreat from the

RP2 position. The aRG is located between the two Arsine Pass deposits and a third one located at the head of TA Valley, the whole forming a continuous cover [Fig. 7b]. The only RA deposit numerically dated is the one responsible for the Arsine Pass eastern boulder field (RA2) [Fig. 6b; Fig. 7b] emplaced around **10.71 ± 0.42 ka**, based on the Bayesian age model. We suggest that the debris that became the aRG was emplaced on the ice by a catastrophic event originating at high elevation (c. 3405 m) in the eastern sector of Arsine's cirque headwall [Section 4.2.4; Fig. 11c] and that it was the same RA that constituted the Arsine Pass boulder deposits. At the time of the dated RA2, Arsine Glacier was likely to have a size analogous to its present-day's [Nicolussi et al., unpublished], and the final reach of the debris/ice mixture greatly exceeded the glacier margin [Fig. 11c]. Supporting geomorphic evidence includes the longitudinal ridges observed at the Arsine Pass western deposit [Fig. 6b] which are characteristics of ice rich mixture travelling over glacier-free terrain [Dufresne and Davies, 2009].

From the morphostratigraphy, it can be proposed that the two RAs, with estimated minimum rock volumes of c. **0.8×10^6 m^3** (RA1) and c. **8.4×10^6 m^3** (RA2) [Tab. 3], have occurred after deposition of the 'Inner complex' (RP2/TA2) and before deposition of RP1/TA1. From the TCN-dating, they occurred between ~11.10 and ~10.71 ka, thus within less than four centuries [Fig. 11c]. The RA1 likely occurred first, before deglaciation of the RP Valley (i.e., shortly after 11.10 ka).

Interestingly, TCN ages obtained from a RA deposit (c. 0.1×10^5 m^3) located only 5 km to the west in the Romanche Valley [RA2ro, Chenet et al., 2016] have a similarly large age range (n = 5; 12.86 ± 1.13 ka to 10.18 ± 0.48 ka). The three oldest boulder ages are conflicting with the mean ages of moraines downstream [Schoeneich et al., 2019]. We therefore suggest that they bear slight inheritance and that only the two youngest ages best represent the timing of the RA2ro emplacement at **10.39 ± 0.50 ka**, thus being contemporary within uncertainties to the RA deposit at Arsine Pass (**10.71 ± 0.42 ka**). The two Arsine RAs constitute major morphogenetic events, which – together with the RA2ro event – seem to define a period of increased rock slope failure activity [Fig. 10f], likely linked to a strong summer warming and permafrost degradation between ~11 and 10.4 ka [Fig. 10b].

5.3.2. Early Holocene rock slope failures in the Alps

The Early Holocene is known as a period of enhanced rock slope failures activity in the Alps (~11.5 to 8.4 ka) based on available inventories [Dapples et al., 2003; Soldati et al., 2006; Prager et al., 2008; Borgatti and Soldati, 2010]. Depending on the geological setting and elevation of

the release area, different triggers are involved. Study cases comparable to the Arsine RA2 include two events in Val Dosdè (Upper Valtellina, Italy), one of which probably travelled onto the ice (RA2do) [Scotti et al., 2017]. Here, the runout distances are c. 2.8 km (RA2do) and 1.5 km (RA3do) and release areas are located at 3000 ± 100 m a.s.l., yielding H/L ratio of 0.30 and 0.39, respectively. The deposits reached a stratigraphic position immediately outboard (RA2do) and inboard (RA3do, like at Arsine) the Kartell stadial extent, and have been dated with Schmidt-hammer to ~**10.80 ± 1.20 ka** and ~**9.90 ± 1.50 ka** [Scotti et al., 2017]. In the eastern Alps, two other events TCN-dated to **10.53 ± 0.67 ka** (n = 2; one outlier) and **10.80 ± 0.76 ka** (n = 4) have been described at lower altitude [Bichler et al., 2016; Reitner et al., 2020]. Here, the rock masses have not travelled onto ice remnants (H/L ratio of 0.52 and 0.36), as detachment areas culminate at 2300 and 1850 m a.s.l., respectively. However, permafrost degradation may have contributed to weakening the slope. All these RAs occurred during a period of significant warming starting at ~11 ka [Affolter et al., 2019; Zander et al., 2024]. This warming has triggered widespread permafrost degradation in Alpine cirque headwalls: 20–80 % of the 2500-3100 m a.s.l. elevation bands were affected until 9.6 ka [Draebing et al., 2024], and subsequently [e.g., Gallach et al., 2020]. This has enhanced mass wasting events and increased headwall erosion rates during the EH [Böhlert et al., 2011; Kenner and Magnusson, 2017; Matthews et al., 2018; Amschwand et al., 2021; Hilger et al., 2021; Booth and Pétursson, 2025]. The same consequences on high-elevated rock slopes have been evidenced as a result of recent anthropogenic warming [Ravanel and Deline; 2011; Legay et al., 2021; Courtial-Manent et al., 2025; Fey et al., 2025].

5.3.3. Genetic origin of the ‘apparent rock glacier’

A periglacial origin of the aRG can be excluded, given (i) the glacial setting (deglaciation of the site at ~11 ka, and then *quasi*-continuous presence of a glacier in the catchment during the Holocene), and (ii) the disconnection from any possible source area. Indeed, the aRG front is located c. 3 km from the headwall, which is only compatible with the development of a ‘talus-derived’ rock glacier when considering the upper bound of EH creeping rates (0.12-0.30 m a^{-1}) [Böhlert et al., 2011; Scapozza, 2013; Moran et al., 2016c; Lehmann et al., 2022], but not the Holocene-averaged rates, which are lower (0.02-0.20 m a^{-1}) [Scapozza, 2013; Lehmann et al., 2022; Munroe et al., 2024]. Regarding a ‘moraine-derived’ origin, it is unlikely that a landform of this volume has developed only fed by the stock of morainic debris available at the time of emplacement. When the RA2 occurred (~10.7 ka), the prominent PMC did not exist yet, and there was no large frontal moraine upstream.

The Arsine aRG was 'glacier-derived', as it formed at the tip of a heavily debris-covered glacier under a rapidly warming climate. The aRG can thus be seen as the last stage of the continuum between a debris-free glacier and a rock glacier, via a debris-covered glacier, as proposed by several studies [Anderson et al., 2018; Jones et al., 2019; Fernández-Fernández et al., 2020]. However, as debris supply was not steady but catastrophic, and likely the result of a climate-driven large scale rock slope failure which made available a large amount of material, the aRG has also a paraglacial origin [Knight et al., 2019]. It has also been found that high-magnitude, low-frequency events can explain the development and morphology of certain composite rock glaciers [Degenhardt, 2009].

5.3.4. Timing of the 'apparent rock glacier' emplacement

After the RA2 event at ~10.7 ka, the glacier probably started to re-advance and deposited the aRG outer moraine ridge (TA1a) with a lag of ~0.5 ka (~10.3 ka), and the aRG inner moraine ridge (TA1c) 350 m behind, with a lag of ~1.2 ka (~9.5 ka) [Fig. 11d,e]. Based on the estimated glacier position at ~10.7 ka (c. 2015 CE extent) and the location of the frontal moraine (TA1a), we can infer that this post-RA2 advance extended over c. 1250 m [Fig. 11c,d]. This is a large magnitude advance, given the size of the glacier, but of the same order (under similar assumptions) than at the other sites where it was dated [e.g., Moran et al., 2016a; Scotti et al., 2017]. Overall, the whole aRG emplacement has spanned only 0.7 ka. Although it mostly took place during a generally glacier-unfriendly period (HTMP 1, 10.2 to 8.2 ka) [Le Roy et al., 2024] [Fig. 10a], the dates we obtained for the moraine ridges show their stabilisation occurred during known periods of glacier culminations in the Alps, at 10.3 ka (often two close moraines deposited at this time, see above) and 9.6 ka [Le Roy et al., 2024] [Fig. 10b].

The final stabilization of the aRG inner ridge at **9.52 ± 0.43 ka** (according to the Bayesian age model) or **9.57 ± 0.24 ka** (based on the mean age of moraine TA1c) occurred concomitantly to a small advance of Tschierva Glacier tree-ring dated to **9.62 ka** (7623 BCE) [Fig. 10b]. This advance ended a marked retreat beyond its 2017 CE extent and then exceeded at least this position [Nicolussi et al., 2019]. This faint cooling evidenced in the Alps is also visible in some temperature reconstructions [e.g., Zander et al., 2024]. It predated the Greenland '9.3 ka event' which led to moraine deposition in the Arctic [Pendleton et al., 2019; Young et al., 2020] but likely not in the Alps [but see also Le Roy et al., 2023], where this advance was probably quite restricted, as it occurred during the ~2 ka-long HTMP 1, between ~10.2 and 8.2 ka [Luetscher et al., 2011; Le Roy et al., 2024] [Fig. 10a,b]. We therefore hypothesise that the related coolings

1352 that briefly interrupted the marked EH warming were recorded by the aRG morphology and
1353 that these moraine ridges formed in response to climate-induced advancing ice.

1354 Despite significant warming starting at 11 ka, it is not clear if the periglacial belt rose
1355 accordingly, assuming that the lower permafrost limit was considerably more depressed than
1356 the ELA at the end of the YD [Frauenfelder et al., 2001; Moran et al., 2016c]. It remains that
1357 most RGs from the 1900-2300 m a.s.l. belt became inactive at that time [Le Roy et al., 2024].
1358 However, periglacial activity within the footprint of PBO moraines has been proposed at several
1359 sites in the Alps, leading to delayed stabilization of thick debris cover [e.g., Moran et al., 2017a;
1360 Le Roy et al., 2024]. For this reason, after deposition as moraines, the aRG ridges could have
1361 undergone slight creeping, as suggested by their rounded morphology.

1362 Even though the location of the 10.3 ka aRG ridge is not anomalous with respect to other
1363 moraine of this age in the Alps – which are often found midway between earlier EH and LIA
1364 positions [Le Roy et al., 2024] – the location of the 9.5 ka ridge clearly differs from available
1365 evidence for that period. Indeed, it is established that (i) small glacier systems at high elevation
1366 (> 2800 m a.s.l.) withdrew inboard their 1880 CE extent before 10 ka, and then inboard their
1367 1950 CE extent around 9.5 ± 0.5 cal ka [Koinig et al., 2019], and that (ii) large valley glaciers
1368 tongues at lower elevation (c. 2200-2300 m a.s.l.) were shorter than their 2005 CE extent almost
1369 continuously between 10.2 and 8.2 ka [Nicolussi and Patzelt, 2001; Nicolussi, 2011; Nicolussi
1370 and Schlüchter, 2012; Nicolussi et al., 2020]. The persistence of the Arsine Glacier eastern front
1371 outboard the LIA extent as late as 9.5 ka therefore probably has a geomorphic origin. We
1372 propose that this unusually large glacier extent is due to local insulation by the RA2 debris,
1373 which prevented the eastern branch of the glacier from melting during the final EH warming,
1374 while the western branch probably receded within the maximum Neoglacial extent after the
1375 deposition of the RP1 moraine [Fig. 11e].
1376
1377 5.4. The mid-Holocene Thermal Maximum
1378 Based on our comprehensive moraine mapping and dating, no evidence was found at Arsine
1379 for moraine deposition between ~9.5 ka and 3.7 ka – bearing in mind that the location of the
1380 aRG inner ridge outboard the LIA extent (that enabled its preservation) cannot be considered
1381 entirely climate-driven here. Part of this interval (between ~6.2 and 3.4 ka) equally stands out
1382 as a quiescent phase of nearby Vallon de la Route rock glacier [Lehmann et al., 2022] [Fig.
1383 10g], revealing unfavourable conditions during the mid-Holocene for glacier and rock glacier
1384 activity in the massif.

Available paleoecological records in the region, pollen- and tree ring- based, indicate that the treeline was high during the mid-Holocene [Chardon, 1991; Edouard et al., 2002; Edouard and Thomas, 2008; Walsh et al., 2014; Cabanat et al., 2017]. The most ice proximal of these peat bog sites, located at 2050 m a.s.l. in the Lavey Valley (only 300 m outboard the LIA extent of Sellettes and Muande Glaciers) [Fig. 1], revealed *Pinus cembra* pollens and macro-remains, witnessing forest stand development between ~6.0 and 2.7 cal ka at a place which is devoid of trees today [Couteaux, 1984]. Besides pollen analysis, mega-fossils (trunks), few of which were dated, were found at different locations in the core of the EPM > 2000 m a.s.l., and testify to a formerly higher-elevated treeline [Allix, 1930; Samivel, 1978; Vivian, 1979; Edouard, 1994; Le Roy et al., 2017].

Several RAs are TCN-dated to the HTMPs in the EPM [Fig. 10f]. One of the most impressive examples is the c. 23 × 10^6 m^3 multi-stage Fontfroide landslide, which dammed the Pré de Madame Carle in the Vallouise Valley [Cossart and Fort, 2008] [Fig. 1]. The release area is thought to be between 2500 and 3000 m a.s.l. on the south face of Pic de Dormillouse (3410 m a.s.l.). The emplacement of the Fontfroide RA deposit is estimated to have occurred in several stages, the first of which is dated to **9.18 ka ± 0.21 ka** (n = 2), which is significantly younger than deglaciation age, contrary to what was originally stated [Cossart et al., 2008]. The largest event in the EPM, the Lauvitel RA, also occurred during the HTMPs. It is estimated to be c. 50–70 × 10^6 m^3 (from scar volume) and the deposit that dammed Lauvitel Lake is estimated to be at least 12 ± 4 × 10^6 m^3. TCN-dating of the event yielded a mean age of **5.16 ka ± 0.38 ka** (n = 4; 3 outliers) [Delunel et al., 2010]. Near Arsine Glacier, five smaller RA deposits mantling the Haute Romanche Valley floor have been described. They have not been reworked by a glacier and their volume ranges 0.1 to 1 × 10^5 m^3 [Violot, 2014]. In addition to RA2ro (Section 5.3.1), another of these RAs (RA1ro; c. 0.3 × 10^5 m^3) was TCN-dated to **6.96 ± 0.16 ka** (n = 2) [Chenet et al., 2016] [Fig. 10f].

5.5. Neoglacial advances

The onset of the Neoglacial spans ~5.7 to ~3.6 ka in the Alps, depending on the elevation and the sensitivity of the studied cryospheric feature [Bohleber et al., 2020; Le Roy et al., 2024] [Fig. 10]. In the Grandes Rousses massif, the proglacial Lake Blanc Huez (2543 m a.s.l.) [Fig. 1] record shows enhanced glacial activity from ~5.5 ka onwards [Simonneau et al., 2014]. In the EPM, Le Roy et al. [2017] proposed that the 4.2 ka advance, TCN-dated at the nearby Bonnepierre Glacier (8 km SW of Arsine) [Fig. 1], marks the onset of the Neoglacial. The

Neoglacial moraines dated at Arsine Glacier are compared on Fig. 12 with selected glacier proxies from the Alps. There is a good agreement between the TCN-dated moraines and the well-established tree-ring dates for the culmination of these advance periods [Fig. 12]. This holds true for the seven major Neoglacial advances dated at Arsine (five of which are firmly dated), out of the ten known in the Alps [Le Roy et al., 2024].

5.5.1. The Bronze Age Advance Period

The Bronze Age Advance Period (BAAP, ~3.7-3.4 ka) [Le Roy et al., 2024], formerly known as the Löbben advance period [Bortenschlager and Patzelt, 1969; Nicolussi et al., 2006] is the first widespread and widely-dated Neoglacial advance period in the Alps [Fig. 12]. However, previous Neoglacial advances clearly occurred to deposit part of the tens of meters of moraine height, often only the upper part of which is dated to the BAAP. For instance, at Tsijiore Nouve this moraine is c. 40 m high and at the Arsine RLM a vertical distance of c. 37 m separates the EH from the BAAP till units [Fig. 4b; Fig. 8d]. Based on an extensive corpus of tree-ring dates, the first BAAP maximum occurred at 3.63 ka (1626 BCE) and the advance period culminated immediately after 3.54 ka (1540 BCE) [Nicolussi and Patzelt, 2001; Le Roy et al., 2024] [Fig. 12g]. At Arsine, the three boulders dated in the upper part of the RLM distal face share the same location relative to the crest (9 ± 6 m) [Fig. 4b; Fig. 8c,d]. They have been deposited during this advance, dated here to **3.74 ± 0.09 ka** (n = 2; one outlier). This is in good agreement with the two distinct BAAP ridges dated to **3.97 ± 0.05 ka** (n = 2) and **3.98 ± 0.37 ka** (n = 1) at the nearby Bonnepierre Glacier [Le Roy et al., 2017]. Notable other locations that feature TCN-dated BAAP moraine ridges in the Alps include the Längental Glacier, where two BAAP frontal moraines located 450-200 m outboard the LIA are dated to **3.79 ± 0.13 ka** (n = 3) and **3.23 ± 0.25 ka** (n = 1) [Moran et al., 2017b] and the Tsijiore Nouve Glacier, where the BAAP lateral moraine is dated to **3.38 ± 0.10 ka** (n = 2; one outlier) [Schimmelpfennig et al., 2012]. The BAAP was likely triggered by a cluster of volcanic eruptions recently dated between 1681 and 1562 BCE [Pearson et al., 2022; Sigl et al., 2022; van Dijk et al., 2024] [Fig. 10g].

Figure 12. Alpine Neoglacial glacier and paleoclimatic history over the last 4.2 ka. (a) Reconstructed summer (JJA) temperature anomalies with respect to the 1901-2000 CE period based on subfossil wood material from Tyrol spanning the last 2.5 ka. Series smoothed with a 11-yr running mean [Büntgen et al., 2011] and COMNISPA II, a stacked $\delta^{18}O$ record including four speleothems from the Spannagel Cave (2340 m a.s.l., Zillertal, Tyrol) [Fohlmeister et al.,

2013], **(b)** Kernel Density Estimates of TCN-dated boulders of Holocene moraines in the Alps (n = 242). Same as Fig. 10b, **(c)** Mer de Glace tree-ring dated chronology (Mont Blanc massif) [Le Roy et al., 2015], **(d)** Avalanche frequency on a 101-yr average in Lake Lauvitel (EPM) [Fouinat et al., 2018], **(e)** Proglacial Lake Bramant (Grandes Rousses) clastic sedimentation reflecting Saint Sorlin Glacier activity. The record is shown as K/Ti (up to 800 CE) and Ti anomalies afterward. Both series were smoothed by a 30-yr running mean [Guyard et al., 2013], **(f)** Terrigenous input into sub-alpine Lake Bourget (northern French Prealps) [Arnaud et al., 2012], **(g)** All tree-ring-dated wood samples (n = 439) coming from lateral moraines in the Alps and indicating a glacier extent smaller than CE 1850-1960 at the time of tree growth. Same as Fig. 10b [see Le Roy et al., 2024 for details]. Vertical dark grey lines are TCN-based central estimates for moraine deposition at Arsine Glacier along with external uncertainties (grey bands). Tree-ring dates for the culmination of Neoglacial glacier advances in the Alps are shown as vertical green lines, based on **(g)** [see compilation details in Le Roy et al., 2024] and are mostly from the Mer de Glace site [Le Roy et al., 2015]. Out of the ten majors known Neoglacial advances in the Alps, only three were not dated at Arsine Glacier (shown as dotted lines, light green).

5.5.2. The Iron Age Advance Period 1

At Arsine Glacier the most widespread till unit – as it is dated at both lateral moraines – spans ~2.8 to 2.6 ka, with overlapping mean ages within uncertainties. At the LLM, it is dated to **2.62 ± 0.17 ka** and the till unit spans 13 ± 4 m below the main crest [Fig. 8a,b], while at the RLM all boulders were sitting on top of the main crest, dated to **2.76 ± 0.11 ka** [Fig. 2b; Fig. 8c,d]. Taken together, these deposits yield a mean age of **2.69 ± 0.16 ka** and can be linked to the first phase of the Iron Age Advance Period (~3.0-2.4 ka) [Le Roy et al., 2024], formerly known as the Göschenen I cold period in the Alps [Zoller et al., 1966]. The Iron Age Advance Period 1 culmination is tree-ring dated around 2.60 ka (600 BCE) in the Alps, but highstands (> 1920 CE extent) spanned centuries between 2.90 and 2.40 ka [Le Roy et al., 2024]. At some sites, three clearly distinct advances occurred during the Iron Age Advance Period 1 [e.g., Le Roy et al., 2015; Patzelt, 2016] [Fig. 12c]. Even if the Göschenen nomenclature is outdated [see Boxleitner et al., 2019a], significant glacier advances in the order of Neoglacial maxima did actually occur during the time it encompasses. Our results indicate that Arsine Glacier reached at that time a size similar as during the LIA. This is comparable to other small glaciers where such moraines were found slightly outboard the 1850 CE extent [Wipf, 2001; Pindur and

Heuberger, 2010]. At Stein Glacier, the Neoglacial frontal moraine located slightly outboard the LIA maximum was dated to **2.94 ± 0.10 ka** (n = 5) [Schimmelpfennig et al., 2014; 2022]. At the largest Alpine glaciers, this advance was comparatively less important, with a relative extent in the order of the 1950-1890s CE [Nicolussi and Patzelt, 2001; Holzhauser et al., 2005; Holzhauser, 2010; Le Roy et al., 2015].

5.5.3. The Late Antique Advance Period 1

The moraine ridge ('PMC LLM outer crest') [Fig. 2b; Fig. 8b] dated to **1.67 ka ± 0.06 ka** (~350 CE) marks the renewal of glacier activity after the Roman Warm Period (1-250 CE) [Luterbacher et al., 2016]. The four consistent ages obtained here (one slightly 'too-old' age pruned) casts little doubt on the dating. It therefore appears that Arsine Glacier reached a size in the range of the LIA maxima during the first phase of the two-staged Late Antique Advance Period (~250-650 CE) [Le Roy et al., 2024], in line with summer temperature trends [Büntgen et al., 2011] [Fig. 12a]. This is probably due to its short response time. On the other hand, at the largest Alpine glaciers, this first phase has not led to LIA max.-like extent (in contrast to the second phase around 600 CE). Mer de Glace remained inboard its 1946 CE extent up to 312 CE, based on an *in situ* tree-ring dated log [Le Roy et al., 2015] [Fig. 12c]. Then, both Mer de Glace and Gepatsch Glaciers experienced a first Late Antique Advance Period maximum (slightly beyond their 1930 CE extent), tree-ring dated to 337 and 336 CE, respectively [Nicolussi and Patzelt, 2001; Nicolussi et al., 2006; Le Roy et al., 2015]. At Arsine Glacier, the slight inheritance detected in the oldest boulder could be due to above average rockfall activity in the cirque headwall during the Roman Warm Period, as already demonstrated in the Mont Blanc Massif [Gallach et al., 2020]. This first Late Antique Advance Period advance could have been triggered by increasing accumulation as shown by snow avalanche activity peaking ~260 cal CE in Lake Lauvitel [Fouinat et al., 2018] [Fig. 12d].

5.6. The Little Ice Age

The LIA encompasses most of the last millennium (1260-1860 CE) [Nicolussi et al., 2022]. Immediately prior, a High Medieval Advance Period culminated between 1140 and 1180 CE, with glaciers reaching at most their 1870 CE extent [Holzhauser, 2010; Le Roy et al., 2015; Badino et al., 2018; Koinig et al., 2019]. Then, the first LIA maximum ('early-LIA' advance) peaked between the late 13th and late 14th century [Nicolussi et al., 2022]. The timing of the early-LIA is especially well reflected in proglacial lake sediment records around the EPM [Guyard et al., 2013; Simonneau et al., 2014; Fouinat et al., 2017; 2018] [Fig. 1; Fig. 12d,e,f].

At Arsine Glacier, the LIA age population shows two main clusters [Fig. 10e]. Taken together, a similar bimodal distribution on LIA-aged moraines is a classic feature in the Alps and is transcribed in our compilation shown in Fig. 12b. The first cluster (~ 0.75-0.5 ka) is thought to reflect the early-LIA maximum peaking during the 14th century [Fig. 12b]. The second cluster of the LIA age population (0.4-0.15 ka) encompasses the 17th and 19th century maxima – the last (~1850 CE) being dated at Arsine at the 'PMC RLM inner crests' [Fig. 8c].

The LIA advances are documented by scarce direct glaciological evidence in the EPM, even during the 19th century. The two earliest direct historical records of the position of glaciers in the EPM concern the Mont-de-Lans and Pierroux Glaciers [see Fig. 1 for location]. They indicate that their ice margins were close to their 19th century maximum extent in 1318 CE and 1345 CE, respectively [Allix, 1929]. The associated topographic evidence seems sufficiently robust to affirm that the EPM glaciers were in an advanced position in the first half of the 14th century. Another text reported by Allix [1929] indicates that the Meije Glacier was rather contracted in 1497 CE compared with the LIA maxima, which suggests that the early-LIA advance was over. Regarding the late-LIA, historical documentation relating to significant climatic events (e.g., floods) highlights climate worsening which peaked in ~1580-1640 CE and 1800-1860 CE in the Vallouise Valley [Lagier and Masson, 1997; Dallons Thanneur et al., 2025].

At most Alpine sites, evidence related to the early-LIA comes from the steep proximal faces of composite lateral moraines [Nicolussi et al., 2022] or from *in situ* stumps scattered in glacier forefields [Holzhauser et al., 2005; Holzhauser, 2010]. Sometimes, short fragments of early-LIA outer ridges can be found outside of the 19th century deposits, like at the Rhône, Rutor, Horn, Stein and Laraintal Glaciers [Zumbühl and Holzhauser, 1988; Orombelli, 2005; Pindur and Heuberger, 2010; Schimmelpfennig et al., 2014; Braumann et al., 2021]. However, the dating of an extended section of a frontal moraine to the early-LIA is rare in the Alps. At Arsine, it corresponds to the Neoglacial maximum frontal moraine (both 'PMC outer frontal lobes' dated to **0.65 ± 0.03 ka** and **0.50 ± 0.04 ka**) which, based on the resulting age distribution, is likely a composite moraine [Fig. 3]. Such composite nature of 'LIA' frontal moraines is rarely identified, but a few examples do exist [e.g., Braumann et al., 2020; 2022]. Here, the oldest samples may represent bulldozed boulders from pre-existing moraine ridges and thus reflect the re-occupation of roughly the same location by different advances of similar magnitude. In addition to the frontal moraine, a section of the lateral moraine probably also dates from the early-LIA period (**0.58 ± 0.05 ka** at the 'PMC RLM inner crests') [Fig. 2b; Fig. 8c].

5.7. Other possible LIA-like glacier advances

Given the composite nature of the Neoglacial frontal moraine ('PMC outer frontal lobes'), possible ages for pre-LIA advances reaching this location are **8.17 ± 0.30 ka** (ARS-16-16), **1.96 ± 0.18 ka** (ARS-18-01 and -02) and **1.17 ± 0.05 ka** (ARS-19-13) [Fig. 11h].

The age of the oldest sample here might point to a glacier advance coeval with the '8.2 ka event'. This advance has been tree-ring dated to 8.17 ka (6168 BCE) in the Alps [Nicolussi and Schlüchter, 2012] [Fig. 10b]. Current state of knowledge shows that the most advanced positions reached by large Alpine glaciers (LIA area: 22-27 km²) around 8.2 ka did not exceed the LIA maximum and correspond to the c. 1950 CE extent [Nicolussi and Patzelt, 2001; Le Roy et al., 2024]. However, the medium-sized and steep Simony Glacier (LIA area: 4.3 km²) reached an extent of c. 1870 CE [Nicolussi and Patzelt, 2001]. Therefore, at small glaciers (LIA area: 1.5-3.5 km²) an extent slightly exceeding the LIA maximum cannot be ruled out [Joerin, 2006]. For example, a single boulder located in similar stratigraphic position (on a faint ridge 75 m outboard the LIA extent) has also been dated to **8.16 ± 0.41 ka** at the Litzner Glacier [Moran et al., 2016a]. Alternatively, at Arsine, this boulder could have been remobilized from the underlying aRG deposits which stabilized around 9.5 ka in this sector.

The two consistent ages obtained on short boulders ARS-18-01 and -02 in the frontal moraine (mean: **1.96 ± 0.18 ka**) can be tentatively grouped with the similarly-aged larger boulder ARS-19-07 (**2.28 ± 0.09 ka)** from the LLM distal face to yield a mean age of **2.22 ± 0.16 ka**. This reinforces diffuse evidence for a prominent advance prior to the Roman Warm Period, called the Iron Age Advance Period 2, which is known to have peaked at ~2.2-2.1 ka [Le Roy et al., 2024]. It is dated at a few sites in the Alps, including the nearby Bonnepierre Glacier, at **2.31 ± 0.07 ka** (n = 2; one outlier) [Le Roy et al., 2017]. Other sites include Argentière and Lower and Upper Grindelwald Glaciers [Le Roy, 2012; Luetscher et al., 2011; Holzhauser, 2016]. A boulder of similar age (**2.04 ± 0.09 ka**) has also been found in a late-LIA moraine at Talèfre Glacier [Protin et al., 2021], likely indicating a LIA-like extent during the Iron Age Advance Period 2. The '2.1 ka event' and subsequent glacier advance could result from a cluster of volcanic eruptions spanning 172 to 43 BCE [Sigl et al., 2022; van Dijk et al., 2024] [Fig. 10g]. This is the only major Neoglacial advance that has not yet been tree-ring dated in the Alps [Fig. 12g]. Close to our study site, this period stands out in several proglacial lake sediment records [Arnaud et al., 2012; Guyard et al., 2013; Fouinat et al., 2018] [Fig. 12d,e,f].

Finally, the boulder dated to **1.17 ± 0.05 ka** agrees with a 9th century CE deposition, a period known to have seen one of the largest Neoglacial advance, the early Medieval Advance [Le Roy et al., 2024], which culminated around **1.16 ka** (840 CE) based on tree-ring dates [Orombelli and Porter, 1982; Nicolussi and Patzelt, 2001; Holzhauser et al., 2005; Nicolussi et al., 2006; Holzhauser, 2010, 2016]. In the EPM, a Medieval Neoglacial frontal maximum has previously been proposed at Étages Glacier ('M1 moraine') [Le Roy et al., 2017]. Recalculation of the age of this moraine (including a snow correction required for the two short and very flat boulders, not applied in the original publication) yields a mean of **1.08 ± 0.03 ka** (n = 2) and conforms with the early Medieval Advance. In the eastern and central Alps, the early Medieval Advance is TCN-dated to **1.07 ± 0.04 ka** (n = 1) at Jamtal Glacier [Braumann et al., 2021] and **1.22 ± 0.09 ka** (n = 2) at Obersee Glacier [Kronig et al., 2018]. The early Medieval Advance could have been triggered by a particularly prolonged eruption period of Katla (Iceland) between 815 and 827 CE [Büntgen et al., 2017; Sigl et al., 2022].

5.8. Rates and modes of moraine deposition

In lateral position, the dominant deposition mode can vary temporally and spatially during the Holocene, between superposition and accretion [*sensu* Röthlisberger and Schneebeli, 1979]. At Arsine Glacier, both modes occurred on each side, but superposition was the main mode at the LLM while accretion was predominant at the RLM [see Fig. 2b; Fig 4b]. Due to a c. 50 m overdeepening in the eastern part of the bed [Echevin, 1970] [Fig. 9d], glacier flow and till deposition were not constrained by topography on the right bank, whereas they were mainly backed onto the slope on the left bank [Fig. 8]. This discrepancy has led to an asymmetry in the elevation of the lateral moraines. The current LLM crest (eroded LIA crest) is 24 m higher than the RLM crest (stable Neoglacial outer crest) on a transverse profile located c. 150 m upstream the 2015 CE front position. This value increases to 35 m when comparing only both (eroded) LIA crests. Based on the samples from the '2.7 ka advance' (n = 6) – two of which are located on this profile (ARS-19-05 and ARS-16-20) – we can infer that the western glacier margin was at least 12 m higher than the eastern margin during the culmination of this advance. Due to the different deposition modes, the oldest till units that are outcropping in the RLM distal face, dated to the EH and to 3.7 ka [Fig. 4b; Fig. 8c,d], are no longer visible at the LLM. We postulate that they were buried by Late Holocene moraines, as the 2.7 ka till unit extends down to the bottom of the LLM distal face [Fig. 8a,b]. The last LIA advance overtopped the composite lateral moraines, leaving only isolated patches of pre-existing deposits. Late overtopping of the distal face was more widespread at the LLM due to prevalent superposition mode.

The rate of till deposition by superposition during a given advance period can be roughly estimated based on the relative vertical distance to the main lateral crest of some of the dated units [Small et al., 1984] [Fig. 8]. At the LLM, the dated boulders belonging to the '2.7 ka advance' (Iron Age Advance Period 1) spread over a 9 m-thick layer and the boulders belonging to the '1.7 ka advance' (Late Antique Advance Period 1) spread at least the top 6 meters of the outer moraine crest [Fig. 8b]. At the RLM, the dated boulders belonging to the '3.7 ka advance' (Bronze Age Advance Period) spread over a 11 m-thick layer. These estimations are minimum-limiting, as we are not capturing the entire thickness of each unit with this approach. However, it appears that major Neoglacial advance periods added more than 10 m to the lateral moraines when overtopping them. At the RLM, the c. 37 m that separate the 11.1 ka and 3.7 ka till units imply that several advances occurred during this interval [Fig. 8d]. They were not dated by lack of suitable boulders [Fig. 4b].

As lateral till units' thickness are minimum estimates conditioned by boulders sampling, they cannot be directly transcribed into past advances duration. Similarly, past advances magnitude cannot be deduced from till units' elevation, mainly because (i) change of the glacier bed elevation due to sediment aggradation, and (ii) paraglacial overprinting of the moraine during retreat periods are both difficult to constrain. At Arsine, (i) the bed is made up of 10-20 m thick sediments for which the deposition period is not known, and (ii) the lateral moraines are mostly free-standing (i.e. less prone to paraglacial reworking), which might suggest that these parameters are not very effective. However, post-LIA retreat has already led to the destruction of part of the inner accreted moraines at the RLM [Fig. 2b,c; Fig. 8d]. So, this process may already have occurred during previous retreats.

6. Conclusions

We present here the most comprehensive TCN-based Holocene glacier chronology for a single glacier site in the Alps. We find the chronology slightly differs from those developed for the largest Alpine glaciers (LIA size > 25 km²) regarding the relative extents reached during the Neoglacial advance periods. This shows the importance of dating well-preserved moraine records at small glacier sites (LIA size < 4 km²).

The Arsine Glacier's Younger Dryas to Early Holocene chronology main features.

- A major advance during the late YD, marked by a large moraine complex (RP5a-b).
- Four recurrences during the Preboreal (RP4 to RP1), the third and fourth being related to the Preboreal Oscillation and to the '10.3 ka cold event', respectively.

- An uncertain 8.2 ka-aged deposit (based on a single boulder) in a LIA composite frontal moraine. Evidence of the maximum extent reached by glaciers at that time – that remains elusive in the Alps – should therefore be sought at small glacier systems.

During the Early Holocene, at least two rock avalanches travelled partly onto the ice, RA1 and RA2, with minimum volume estimates of c. 0.8 and 8.4×10^6 m^3.

- Two distal deposits that were part of these RAs (RP and AP west) retain pristine surfaces with well-defined ridges, implying they were little affected by post-depositional melting of underlying snow/ice layer.
- The largest event (RA2) reached the Arsine Pass and the Upper Tabuc Valley at ~10.7 ka, and subsequently allowed the development of the 'apparent rock glacier', by slowing down melting of part of the glacier tongue.
- The existence of the 'apparent rock glacier' at the eastern branch of the glacier has made it possible to detect at least one climate-driven EH advances (TA1c) that is not recorded by the debris-free glacier tongue at the western branch. The latter was probably in a much more retracted position at the same time.
- The proposed hypothesis regarding the rock avalanche origin of the 'apparent rock glacier' needs further testing by modelling the runout of the estimated volume and by sedimentological investigations.

The Arsine Glacier's Neoglacial chronology main features.

- Confirmation that the Bronze Age Advance Period (~3.7 ka) is the most widespread preserved moraine of the early Neoglacial at the Alpine scale. This is the third TCN-dated occurrence in the Ecrins-Pelvoux Massif.
- Evidence that the Iron Age Advance Period 1 (~2.8 to 2.6 ka) has been a size equivalent as the LIA maxima at small glaciers.
- Tentative dating of the Iron Age Advance Period 2 in the composite Neoglacial maximum frontal moraine (two short boulders averaging ~2.0 ka**)** pointing to a possible significant advance before the Roman Climatic Optimum. This would be the second TCN-dated occurrence in the Ecrins-Pelvoux Massif.
- Evidence that the first phase of the Late Antique Advance Period at 1.7 ka (~350 CE) has been a size equivalent as the LIA maxima at small glaciers.
- A large early-LIA advance at 0.7 ka (~1370 CE) is materialized by the youngest boulders in the composite Neoglacial maximum frontal moraine located 200 m outboard

the late-LIA frontal moraine (~1850 CE). Two single boulders likely deposited during the same early-LIA advance were also dated at two other locations of the forefield.

Acknowledgements

This work was initiated in 2012 during the PhD thesis project of M.L.R. (funded by French Ministry of Higher Education and Research) and was subsequently supported by the following projects: APIC CEREGE in 2013 (PI: I.S.), *'Dynamique de la déglaciation tardiglaciaire dans le massif des Ecrins'* (PI: P.D.) funded by Zone Atelier Alpes (ZAA) in 2014, the INEE/CNRS DIPEE program in 2015, the ANR project WarHol (ANR-15-CE01-0007-01) (PI: I.S.) for analyses and the MSc internship of P.J. in 2018 and the INSU/CNRS LEFE IMAGO project '*Glady'* (PI: I.S.) in 2019. The ^{10}Be measurements were performed at the ASTER AMS national facility (CEREGE, Aix-en-Provence) which is supported by the INSU/CNRS, the ANR through the 'Projets thematiques d'excellence' program for the 'Equipements d'excellence' ASTER-CEREGE action, IRD and CEA. We acknowledge Ecrins National Park for sampling authorizations (n° 538/2013, 143/2015, 340/2016) and Musée Dauphinois (CD Isère, Grenoble) for making the Paul Helbronner photographs available. We are grateful to Christian Vincent for help with the GCPs and to Laura Poirel, Marie Protin and Jesús Alcalá for support in the field. Thanks to Philippe Choler and the late Serge Aubert for their lively interest at the beginning of the project. Relevant comments from two anonymous reviewers contributed to improve this manuscript.

References

Affolter S., Häuselmann A., Fleitmann D., Edwards R.L., Cheng H., Leuenberger M., 2019. Central Europe temperature constrained by speleothem fluid inclusion water isotopes over the past 14,000 years. Science Advances 5, 6, eaav3809. http://doi.org/10.1126/sciadv.aav3809

Agisoft., 2019. Agisoft Metashape 2019 version 1.6 User manual.

Akçar, N., Deline, P., Ivy-Ochs, S., Alfimov, V., Hajdas, I., Kubik, P.W., Christl, M. and Schlüchter, C., 2012. The AD 1717 rock avalanche deposits in the upper Ferret Valley (Italy): a dating approach with cosmogenic ^{10}Be. J. Quaternary Sci. 27, 383–392. https://doi.org/10.1002/jqs.1558

Allix, A., 1929. L'Oisans au Moyen-Age. Étude de géographie historique en haute montagne d'après des documents inédits, suivie de la transcription des textes. Librairie ancienne Honoré Champion, 255 pp.

Allix, A., 1930. Le déboisement de l'Oisans. Bull. Soc. Scient. Dauph. 50, 79–164.

1715 Amschwand, D., Ivy-Ochs, S., Frehner, M., Steinemann, O., Christl, M., and Vockenhuber, C., 2021.
1716 Deciphering the evolution of the Bleis Marscha rock glacier (Val d'Err, eastern Switzerland) with
1717 cosmogenic nuclide exposure dating, aerial image correlation, and finite element modelling. The
1718 Cryosphere 15, 2057– 2081. https://doi.org/10.5194/tc-15-2057-2021

1719 Anderson, R.S., Anderson, L.S., Armstrong, W.H., Rossi, M.W., Crump, S.E., 2018. Glaciation of
1720 alpine valleys: the glacier – debris-covered glacier – rock glacier continuum. Geomorphology 311,
1721 127–142. https://doi.org/10.1016/j.geomorph.2018.03.015

1722 Antoine, P., Monnet, J., 1986. Détermination de la stabilité de la moraine limitant a l'Est le lac d' Arsine.
1723 Rapport IRIGM, Grenoble, 27 pp.

1724 Antoine, P, Fabre, D., 2000. Géologie, hydrogéologie et stabilité du système morainique du lac d'Arsine.
1725 Rapport LIGRIM, Université Joseph Fourier, Grenoble, 22 pp.

1726 Arnaud, F., Revillon, S., Debret, M., Revel, M., Chapron, E., Jacob, J., Giguet-Covex, C., Poulenard,
1727 J., Magny, M., 2012. Lake Bourget regional erosion patterns reconstruction reveals Holocene NW
1728 European Alps soil evolution and paleohydrology. Quat. Sci. Rev. 51, 81–92.
1729 https://doi.org/10.1016/j.quascirev.2012.07.025

1730 Arnold, M., Merchel, S., Bourlès, D., Braucher, R., Benedetti, L., Finkel, R.C., Aumaître, G.,
1731 Gottdang, A., Klein, M., 2010. The French accelerator mass spectrometry facility ASTER: improved
1732 performance and developments. Nucl. Instrum. Methods Phys. Res. B 268, 1954–1959.
1733 https://doi.org/10.1016/j.nimb.2010.02.107

1734 Badino, F., Ravazzi, C., Vallè, F., Pini, R., Aceti, A., Brunetti, M., Champvillair, E., Maggi, V.,
1735 Maspero, F., Perego, R., Orombelli, G., 2018. 8800 years of high-altitude vegetation and climate
1736 history at the Rutor Glacier forefield, Italian Alps. Evidence of middle Holocene timberline rise and
1737 glacier contraction. Quat. Sci. Rev. 185, 41–68. https://doi.org/10.1016/j.quascirev.2018.01.022

1738 Bahr, D.B., Pfeffer, W.T., Sassolas, C., Meier, M.F., 1998. Response time of glaciers as a function of
1739 size and mass balance: 1. Theory. J. Geophys. Res. 103, B5, 9777– 9782.
1740 https://doi.org/10.1029/98JB00507

1741 Balco, G., 2020. Glacier Change and Paleoclimate Applications of Cosmogenic-Nuclide Exposure
1742 Dating. Annual Review of Earth and Planetary Sciences, 48, 1. https://doi.org/10.1146/annurev-earth-
1743 081619-052609

1744 Barbier, R., Barféty, J.C., Bordet, P., 1976. Notice de la carte géologique de la France à 1/50 000e,
1745 feuille 798 (La Grave). Bureau de Recherches Géologiques et Minière, Orléans.

1746 Barr, I.D. Lovell, H., 2014. A review of topographic controls on moraine distribution. Geomorphology
1747 226, 44–64. https://doi.org/10.1016/j.geomorph.2014.07.030

1748 Barsch, D., Jakob, M., 1998. Mass transport by active rockglaciers in the Khumbu Himalaya.
1749 Geomorphology 26, 215–222. https://doi.org/10.1016/S0169-555X(98)00060-9

1750 Beaudevin, C., 2001. Contribution à l'étude de l'altitude atteinte par les glaciers quaternaires dans
1751 quelques vallées alpines. Géol. Alp. 76, 83–116.

1752 Belli, R., Frisia, S., Borsato, A., Drysdale, R., Hellstrom, J. Zhao, J.-x., Spötl, C., 2013. Regional
1753 climate variability and ecosystem responses to the last deglaciation in the northern hemisphere from
1754 stable isotope data and calcite fabrics in two northern Adriatic stalagmites. Quaternary Science
1755 Reviews 72, 146158. https://doi.org/10.1016/j.quascirev.2013.04.014

Bichler, M. G., Reindl, M., 2013. Landscape evolution north of the Sonnblick (Salzburg) during the Alpine Lateglacial. MSc thesis, Universität Wien, 164 pp. https://phaidra.univie.ac.at/o:1302146

Bichler, M. G., Reindl, M., Reitner, J.M., Drescher-Schneider, R., Wirsig, C., Christl, M., Hajdas, I., Ivy-Ochs, S., 2016. Landslide deposits as stratigraphical markers for a sequence-based glacial stratigraphy: a case study of a Younger Dryas system in the Eastern Alps. Boreas 45, 3, 537–551. https://doi.org/10.1111/bor.12173

Björck, S., Muscheler, R., Kromer, B., Andresen, C.S., Heinemeier, J., Johnsen, S.J., Conley, D., Koç, N., Spurk, M., Veski, S., 2001. High-resolution analyses of an early Holocene climate event may imply decreased solar forcing as an important climate trigger. Geology 29, 1107. https://doi.org/10.1130/0091-7613(2001)029<1107:HRAOAE>2.0.CO;2

Boch, R., Spötl, C., Kramers, J., 2009. High-resolution isotope records of early Holocene rapid climate change from two coeval stalagmites of Katerloch Cave, Austria. Quaternary Science Reviews 28 (2324), 25272538. https://doi.org/10.1016/j.quascirev.2009.05.015

Bohleber, P., Schwikowski, M., Stocker-Waldhuber, M., Fang L., Fischer A., 2020. New glacier evidence for ice-free summits during the life of the Tyrolean Iceman. Sci. Rep. 10, 20513. https://doi.org/10.1038/s41598-020-77518-9

Böhlert, R., Egli, M., Maisch, M., Brandová, D., Ivy-Ochs, S., Kubik, P. W., Haeberli, W., 2011. Application of a combination of dating techniques to reconstruct the Lateglacial and early Holocene landscape history of the Albula region (eastern Switzerland). Geomorphology 127, 1-2, 1–13. https://doi.org/10.1016/j.geomorph.2010.10.034

Bolibar, J., Rabatel, A., Gouttevin, I., Galiez, C., 2020. A deep learning reconstruction of mass balance series for all glaciers in the French Alps: 1967–2015. Earth Syst. Sci. Data 12, 1973–1983. https://doi.org/10.5194/essd-12-1973-2020

Bonaparte R., 1891. Les variations périodiques des glaciers français. Annuaire du C.A.F., 17e et 18e vol., 1890-1891.

Booth, A.M., Pétursson, H.G., 2025. Permafrost and structural controls on Holocene bedrock landslide occurrence around Eyjafjörður, north-central Iceland. Journal of Geophysical Research: Earth Surface, 130, e2024JF007933. https://doi.org/10.1029/2024JF007933

Borchers, B., Marrero, S., Balco, G., Caffee, M., Goehring, B., Lifton, N., Nishiizumi, K., Phillips, F., Schaefer, J., Stone, J., 2016. Geological calibration of spallation production rates in the CRONUS-Earth project. Quaternary Geochronology 31, 188-198. https://doi.org/10.1016/j.quageo.2015.01.009

Bortenschlager, S., Patzelt, G., 1969. Wärmezeitliche Klimat- und Gletscherschwankungen im Pollenprofil eines hochgelegenen Moores 2.270 m der Venedigergruppe. Eiszeitalter Ggw. 20, 116–122.

Boston, C.M., Chandler, B.M.P., Lovell, H., Weber, P., Davies, B.J., 2023. The role of topography in landform development at an active temperate glacier in Arctic Norway. Earth Surface Processes and Landforms 48, 9, 1783–1803. https://doi.org/10.1002/esp.5588

Bourgeat, S., 1990. Éboulements et écroulements dans le bassin versant du Vénéon (massif des Ecrins, Isère). Rev. Géogr. Alpine 28 (1/2/3), 11–23.

Boxleitner M., Ivy-Ochs S., Egli M., Brandova D., Christl M., Dahms D., Maisch M., 2019a. The ^{10}Be deglaciation chronology of the Göschenertal, central Swiss Alps, and new insights into the Göschenen Cold Phases. Boreas 48, 4, 867–878. https://doi.org/10.1111/bor.12394

1798 Boxleitner, M., Ivy-Ochs, S., Egli, M., Brandova, D., Christl, M., Maisch, M., 2019b. Lateglacial and
1799 Early Holocene glacier stages – New dating evidence from the Meiental in central Switzerland.
1800 Geomorphology 340, 15–31. https://doi.org/10.1016/j.geomorph.2019.04.004

1801 Braucher, R., Guillou, V., Bourles, D. L., Arnold, M., Aumaître, G., Keddadouche, K., Nottoli, E.,
1802 2015. Preparation of ASTER inhouse 10Be/9Be standard solutions. Nucl. Instrum. Meth. B, 361, 335–
1803 340. https://doi.org/10.1016/j.nimb.2015.06.012

1804 Braumann, S.M., Schaefer, J.M., Neuhuber, S.M., Reitner, J.M., Lüthgens, C., Fiebig, M., 2020.
1805 Holocene glacier change in the Silvretta Massif (Austrian Alps) constrained by a new ^{10}Be
1806 chronology, historical records and modern observations. Quaternary Science Reviews 245, 106493.
1807 https://doi.org/10.1016/j.quascirev.2020.106493

1808 Braumann, S.M., Schaefer, J.M., Neuhuber, S.M., Lüthgens, C., Hidy, A.J., Fiebig, M., 2021. Early
1809 Holocene cold snaps and their expression in the moraine record of the Eastern European Alps. Clim.
1810 Past Discuss. https://doi.org/10.5194/cp-2021-54

1811 Braumann, S.M., Schaefer, J.M., Neuhuber, S., Fiebig, M., 2022. Moraines in the Austrian Alps
1812 Record Repeated Phases of Glacier Stabilization through the Late Glacial and the Early Holocene.
1813 Scientific Reports. https://doi.org/10.1038/s41598-022-12477-x

1814 Bronk Ramsey, C., 2008. Deposition models for chronological records. Quat. Sci. Rev. 27, 1-2, 42–60.
1815 https://doi.org/10.1016/j.quascirev.2007.01.019

1816 Brooks, J.P., Larocca, L.J., Axford, Y.L., 2022. Little Ice Age climate in southernmost Greenland
1817 inferred from quantitative geospatial analyses of alpine glacier reconstructions. Quaternary Science
1818 Reviews 293, 107701. https://doi.org/10.1016/j.quascirev.2022.107701

1819 Büntgen, U., Tegel, W., Nicolussi, K., McCormick, M., Frank, D., Trouet, V., Kaplan, J., Herzig, F.,
1820 Heussner, U., Wanner, H., Luterbacher, J., Esper, J., 2011. 2500 years of European climate variability
1821 and human susceptibility. Science 331, 578–582. https://doi.org/10.1126/science.1197175

1822 Büntgen, U., Eggertsson, O., Wacker, L., Sigl, M., Ljungqvist, F. C., Di Cosmo, N., Plunkett, G.,
1823 Krusic, P. J., Newfield, T. P., Esper, J., Lane, C., Reinig, F., Oppenheimer, C., 2017. Multi-proxy
1824 dating of Iceland's major pre-settlement Katla eruption to 822-823 CE. Geology, 45, 783–786.
1825 https://doi.org/10.1130/G39269.1

1826 Burki, V., Hansen, L., Fredin, O., Andersen, T.A., Beylich, A.A., Jaboyedoff, M., Larsen, E.,
1827 Tønnesen, J.-F., 2010. Little Ice Age advance and retreat sediment budgets for an outlet glacier in
1828 western Norway. Boreas 39, 3, 551–566. https://doi.org/10.1111/j.1502-3885.2009.00133.x

1829 Cabanat, A.-L., David, F., Latil, J.-L., Perrier, C., Aubert, S., 2017. Vegetation cover changes during
1830 the last 7200 years at 2000 m in the Southwestern Alps (Lautaret Pass, France): A combined
1831 palynological and paleobotanical study. Review of Palaeobotany and Palynology, 246, 32–43.
1832 https://doi.org/10.1016/j.revpalbo.2017.05.012

1833 Carcaillet, C., Blarquez, O., 2017. Fire ecology of a tree glacial refugium on a nunatak with a view on
1834 Alpine glaciers. New Phytol, 216: 1281-1290. https://doi.org/10.1111/nph.14721

1835 Carcaillet, C., Latil, J-L., Abou, S., Ali, A., Ghaleb, B., Magnin, F., Roiron, P., Aubert, S., 2018. Keep
1836 your feet warm? A cryptic refugium of trees linked to a geothermal spring in an ocean of glaciers.
1837 Glob Change Biol., 24, 2476–2487. https://doi.org/10.1111/gcb.14067

1838 CEMAGREF, groupement d'Aix-en-Provence (division Hydraulique générale), 1986. Lac du Glacier
1839 d'Arsine. Étude demandée par la direction départementale de la protection civile, à l'initiative du
1840 service RTM de Gap.

Chardon, M., 1991. L'évolution tardiglaciaire et holocène des glaciers et de la végétation autour de l'Alpe d'Huez (Oisans, Alpes Françaises). Revue de géographie alpine, 79, 2, 39–53.

Charton, J., Verfaillie, D., Jomelli, V., Francou, B., 2021. Early Holocene rock glacier stabilisation at col du Lautaret (French Alps): Palaeoclimatic implications. Geomorphology 394, 107962. https://doi.org/10.1016/j.geomorph.2021.107962

Charton, J., Schimmelpfennig, I., Jomelli, V., Delpech, G., Blard, P.-H., Braucher, R., Verfaillie, D., Favier, V., Rinterknecht, V., Goosse, H., Crosta, X., Chassiot, L., Martin, L., Guillaume, D., Legentil, C., ASTER Team, 2022. New cosmogenic nuclide constraints on Late Glacial and Holocene glacier fluctuations in the sub-Antarctic Indian Ocean (Kerguelen Islands, 49°S). Quaternary Science Reviews 293, 107461. https://doi.org/10.1016/j.quascirev.2022.107461

Chenet, M., Brunstein, D., Jomelli, V., Roussel, E., Rinterknecht, V., Mokadem, F., Biette, M., Robert, V., Leanni, L. 2016. ^{10}Be cosmic-ray exposure dating of moraines and rock avalanches in the Upper Romanche valley (French Alps): evidence of two glacial advances during the Late Glacial/Holocene transition. Quaternary Science Reviews 148, 209–221. https://doi.org/10.1016/j.quascirev.2016.07.025

Chmeleff, J., von Blanckenburg, F., Kossert, K., Jakob, J., 2010. Determination of the ^{10}Be half-life by multicollector ICP-MS and liquid scintillation counting. Nucl. Instrum. Methods Phys. Res. B 268 (2), 192–199. https://doi.org/10.1016/j.nimb.2009.09.012

Christian, J.E., Whorton, E., Carnahan, E., Koutnik, M., Roe, G., 2022. Differences in the transient responses of individual glaciers: a case study of the Cascade Mountains of Washington State, USA. Journal of Glaciology 1–13. https://doi.org/10.1017/jog.2021.133

Claude, A., Ivy-Ochs, S., Kober, F., Antognini, M., Salcher, B., Kubik, P.W., 2014. The Chironico landslide (Valle Leventina, southern Swiss Alps): age and evolution. Swiss J. Geosci. 107, 273–291. https://doi.org/10.1007/s00015-014-0170-z

Clark, D.H., Clark, M.M., Gillespie, A.R., 1994. Debris-covered glaciers in the Sierra Nevada, California, and their implications for snowline reconstructions. Quaternary Research 41, 139–153. https://doi.org/10.1006/qres.1994.1016

Clauzel, L., Ménégoz, M., Gilbert, A., Gagliardini, O., Six, D., Gastineau, G., Vincent, C., 2023. Sensitivity of glaciers in the European Alps to anthropogenic atmospheric forcings: Case study of the Argentière Glacier. Geophysical Research Letters, 50, e2022GL100363. https://doi.org/10.1029/2022GL100363

Colas, A., 2000. Recherches géomorphologiques en Vallouise. Unpublished PhD Thesis, Lille 1 University, 458 pp.

Cossart, E., 2005. Évolution géomorphologique du haut bassin durancien depuis la dernière glaciation – contribution à la compréhension du fonctionnement du système paraglaciaire. Unpublished PhD Thesis, Paris 7 University, 380 pp.

Cossart, E., 2011. Mapping Glacier Variations at Regional Scale through Equilibrium Line Altitude Interpolation: GIS and Statistical Application in Massif des Ecrins (French Alps). J. Geogr. Inf. Syst. 3, 232–241. https://doi.org/10.4236/jgis.2011.33020

Cossart, E., Fort, M., 2008. Consequences of landslide dams on alpine river valleys: Examples and typology from the French Southern Alps. Norsk Geografisk Tidsskrift - Norwegian Journal of Geography, 62, 2, 75–88. https://doi.org/10.1080/00291950802094882

Cossart, E., Braucher, R., Fort, M., Bourlès, D. L., Carcaillet, J., 2008. Slope instability in relation to glacial debuttressing in alpine areas (Upper Durance catchment, southeastern France): Evidence from field data and 10Be cosmic ray exposure ages. Geomorphology 95, 1-2, 3–26. https://doi.org/10.1016/j.geomorph.2006.12.022

Cossart, E., Bourlès, D., Braucher, R., Carcaillet, J., Fort, M., Siame, L., 2011. L'englacement du haut bassin durancien (Alpes françaises du sud) du Dernier Maximum Glaciaire à l'Holocène: synthèse chronologique. Géomorphologie: Relief, Processus, Environnement 17, 2, 123–142. https://doi.org/10.4000/geomorphologie.9336

Cossart, E., Fort, M., Bourles, D., Braucher, R., Siame, L., 2012. Deglaciation pattern during the Lateglacial/Holocene transition in the southern French Alps. Chronological data and geographical reconstruction from the Clarée Valley (upper Durance catchment, southeastern France). Palaeogeography Palaeoclimatology Palaeoecology, 315–316, 109–123. https://doi.org/10.1016/j.palaeo.2011.11.017

Courtial-Manent, L., Mugnier, J-L., Ravanel, L., Carcaillet, J., Deline, P., Buoncristiani, J-F., 2025. A significant doubling of rockfall rates since the Little Ice Age in the Mont-Blanc massif, inferred from 10Be concentrations and rockfall inventories. Earth and Planetary Science Letters, 651, 119142. https://doi.org/10.1016/j.epsl.2024.119142

Coûteaux, M., 1983a. Fluctuations glaciaires de la fin du Würm dans les Alpes françaises, établies par des analyses polliniques. Boreas, 12, 1, 35–56. https://doi.org/10.1111/j.1502-3885.1983.tb00359.x

Coûteaux, M., 1983b. La déglaciation du vallon de la Lavey (Vallée du Vénéon, massif des Ecrins, Isère), S.H.F., Section de Glaciologie, compte-rendu de la séance de Grenoble (Mars 1983), 1–13.

Coûteaux, M., 1984. Présence, datages et signification phytosociologique de macrorestes de Pinus et de pollens de *Pinus cembra* L. à 2050 m dans le vallon de la Lavey (massif des Ecrins, Isère, France). Revue de Paléobiologie. NS, 55–62.

Coutterand, S., 2010. Étude géomorphologique des flux glaciaires dans les Alpes nord-occidentales au Pléistocène récent. Du maximum de la dernière glaciation aux premières étapes de la déglaciation. Géographie. Université de Savoie, 468 pp.

Crump, S.E., Anderson, L.S., Miller, G.H., Anderson, R.S., 2017. Interpreting exposure ages from ice-cored moraines: a Neoglacial case study on Baffin Island, Arctic Canada. J. Quaternary Sci. 32, 1049–1062. https://doi.org/10.1002/jqs.2979

Cusicanqui, D., Rabatel, A., Vincent, C., Bodin, X., Thibert, E., Francou, B., 2021. Interpretation of volume and flux changes of the Laurichard rock glacier between 1952 and 2019, French Alps. Journal of Geophysical Research: Earth Surface, 126, e2021JF006161. https://doi.org/10.1029/2021JF006161

Dallons Thanneur, L., Giacona, F., Eckert, N., Frey, P., 2025. Constitution of a multicentennial multirisk database in a mountainous environment from composite sources: the example of the Vallouise-Pelvoux municipality (Ecrins, France), EGUsphere [preprint]. https://doi.org/10.5194/egusphere-2025-761

Dapples, F., Oswald, D., Raetzo, H., Lardelli, T., Zwahlen, P., 2003. New records of Holocene landslide activity in the western and eastern Swiss Alps: Implication of climate and vegetation changes. Eclogae Geol. Helv., 96, 1–9. http://doi.org/10.5169/seals-169002

Delaney, K.B., Evans, S.G., 2014. The 1997 Mount Munday landslide (British Columbia) and the behaviour of rock avalanches on glacier surfaces. Landslides 11, 1019–1036. https://doi.org/10.1007/s10346-013-0456-7

Delgado, F., Zerathe, S., Schwartz, S., Gaidzik, K., Robert, X., Carcaillet, J., Benavente, C., Aumaître, G., 2025. Pleistocene Chronicles of Large Landslides Triggering on the Western Flank of the Central Andes Revealed by Cosmogenic Nuclide Dating. Journal of South American Earth Sciences, 152, 105290. https://doi.org/10.1016/j.jsames.2024.105290

Deline, P., 2009. Interactions between rock avalanches and glaciers in the Mont Blanc massif during the late Holocene. Quaternary Science Reviews, 28, 11-12, 1070–1083. https://doi.org/10.1016/j.quascirev.2008.09.025

Deline, P., Orombelli, G., 2005. Glacier fluctuations in the western Alps during the Neoglacial, as indicated by the Miage morainic amphitheatre (Mont Blanc massif, Italy). Boreas 34, 456–467. https://doi.org/10.1111/j.1502-3885.2005.tb01444.x

Deline, P., Kirkbride, M.P., 2009. Rock avalanches on a glacier and morainic complex in Haut Val Ferret (Mont Blanc Massif, Italy). Geomorphology, 103, 1, 80–92. https://doi.org/10.1016/j.geomorph.2007.10.020

Deline, P., Akçar, N., Ivy-Ochs, S., & Kubik, P.W., 2015. Repeated Holocene rock avalanches onto the Brenva Glacier, Mont Blanc massif, Italy: A chronology. Quaternary Science Reviews, 126, 186–200. https://doi.org/10.1016/j.quascirev.2015.09.004

Deline, P., Gruber, S., Amann, F., Bodin, X., Delaloye, R., Failletaz, J., Fischer, L., Geertsema, M., Giardino, M., Hasler, A., Kirkbride, M., Krautblatter, M., Magnin, F., McColl, S., Ravanel, L., Schoeneich, P., Weber, S., 2021. Chapter 15 - Ice loss from glaciers and permafrost and related slope instability in high-mountain regions. In: Haeberli, W., Whiteman, C. (Eds.) Hazards and Disasters Series, Snow and Ice-Related Hazards, Risks, and Disasters (Second Edition), 501–540. https://doi.org/10.1016/B978-0-12-817129-5.00015-9

Delunel, R., 2010. Évolution géomorphologique du massif des Ecrins-Pelvoux depuis le Dernier Maximum Glaciaire. Apports des nucléides cosmogéniques produits *in-situ*. PhD thesis, Université Joseph Fourier, Grenoble, 261 pp.

Delunel, R., Hantz, D., Braucher, R., Bourles, D.L., Schoeneich, P., Deparis, J., 2010. Surface exposure dating and geophysical prospecting of the Holocene Lauvitel rock slide (French Alps). Landslides 7, 393–400. https://doi.org/10.1007/s10346-010-0221-0

Degenhardt, J.J., 2009. Development of tongue-shaped and multilobate rock glaciers in alpine environments – Interpretations from ground penetrating radar surveys. Geomorphology 109, 3–4, 94–107. https://doi.org/10.1016/j.geomorph.2009.02.020

Draebing, D., Mayer, T., Jacobs, B., Binnie, S.A., Dühnforth, M., McColl, S.T., 2024. Holocene warming of alpine rockwalls decreased rockwall erosion rates. Earth and Planetary Science Letters 626. https://doi.org/10.1016/j.epsl.2023.118496

Dufresne, A., Davies, T.R. 2009. Longitudinal ridges in mass movement deposits. Geomorphology 105, 3-4, 171–181. https://doi.org/10.1016/j.geomorph.2008.09.009

Dumont, T., Champagnac, J.D., Crouzet, C., Rochat, P., 2008. Multistage shortening in the Dauphiné zone (French Alps): the record of Alpine collision and implications for pre-Alpine restoration. Swiss J. Geosci. 101 (Suppl 1), 89–110. https://doi.org/10.1007/s00015-008-1280-2

Echevin, M. 1970. Prospection gravimétrique du glacier d'Arsine. PhD thesis, Université Joseph Fourier, Grenoble, 65 pp.

Edouard, J.-L., 1978. La glaciation dans le massif de l'Oisans. Contribution à la connaissance des fluctuations glaciaires postwürmiennes. PhD Thesis, University of Grenoble, 329 pp.

Edouard, J.L., 1994. Les lacs d'altitude dans les Alpes françaises. Contribution à la connaissance des lacs d'altitude et à l'histoire des milieux montagnards depuis la fin du Tardiglaciaire. PhD Thesis, University of Grenoble, 798 pp.

Edouard, J.L., Guibal, F., Nicault, A., Rathgeber, C., Tessier, L., Thomas, A., Wicha, S., 2002. Arbres subfossiles (Pinus cembra, Pinus uncinata et Larix decidua) et évolution des forêts d'altitude dans les Alpes françaises au cours de l'Holocène. Approche dendrochronologique. In Richard, H., Vignot, A., (Eds.) Actes du colloque international 'Équilibre et rupture dans les écosystèmes depuis 20000 ans en Europe de l'Ouest : durabilité et mutation'. Annales littéraires, 730. Série 'Environnement, Sociétés et Archéologie', Presses Universitaires Francomtoises, n° 3, 403–411.

Edouard, J.L., Thomas, A., 2008. Cernes d'arbres et chronologie holocène dans les Alpes françaises. Actes de la Table ronde JurAlp 'Dynamique holocène de l'environnement dans le Jura et les Alpes : du climat à l'Homme'. In M. Desmet, M. Magny, F. Mocci (Eds), Aix en Provence, 15-16 novembre 2007. Collection EDYTEM 6, 179–190.

Fernández-Fernández, J.M., Palacios, D., Andrés, N., Schimmelpfennig, I., Tanarro, L.M., Brynjólfsson, S., López-Acevedo, F.J., Sæmundsson, Þ., ASTER Team. 2020. Constraints on the timing of debris-covered and rock glaciers: An exploratory case study in the Hólar area, northern Iceland. Geomorphology 361, 107196, https://doi.org/10.1016/j.geomorph.2020.107196

Fey, C., Wichmann, V., Zangerl, C., 2025. Influence of permafrost degradation and glacier retreat on recent high mountain rockfall distribution in the eastern European Alps. Earth Surface Processes and Landforms 50, 5, e70063. https://doi.org/10.1002/esp.70063

Fleischer, F., Haas, F., Altmann, M., Rom, J., Ressl, C., Becht, M., 2023. Glaciogenic Periglacial Landform in the Making – Geomorphological Evolution of a Rockfall on a Small Glacier in the Horlachtal, Stubai Alps, Austria. Remote Sens, 15, 1472. https://doi.org/10.3390/rs15061472

Fohlmeister, J., Vollweiler, N., Spötl, C., Mangini, A., 2013. COMNISPA II: update of a mid-European isotope climate record, 11 ka to present. Holocene 23, 5, 749–754. https://doi.org/10.1177/0959683612465446

Fouinat, L., Sabatier, P., Poulenard, J., Etienne, D., Crouzet, C., Develle, A., Doyen, E., Malet, E., Jean-Louis Reysse, J-L., Sagot, C., Bonet, R., Arnaud, F., 2017. One thousand seven hundred years of interaction between glacial activity and flood frequency in proglacial Lake Muzelle (western French Alps). Quaternary Research 87, 3, 407–422. https://doi.org/10.1017/qua.2017.18

Fouinat, L., Sabatier, P., David, F., Montet, X., Schoeneich, P., Chaumillon, E., Poulenard, J., Arnaud, F., 2018. Wet avalanches: long-term evolution in the Western Alps under climate and human forcing. Clim. Past 14, 1299–1313. https://doi.org/10.5194/cp-14-1299-2018

Francou, B., 1981. Géodynamique des éboulis et formes associées de la Combe de Laurichard (Hautes-Alpes). PhD thesis. University of Grenoble, 153 pp.

Francou, B., Bodin, X., Jomelli, V., 2020. Eboulis et glaciers rocheux de la combe de Laurichard (Col du Lautaret, Hautes-Alpes): à quelle vitesse se détruisent les montagnes ? Les cahiers illustrés du Lautaret, 9, 144 pp.

Gallach, X., Carcaillet, J., Ravanel, L., Deline, P., Ogier, C., Rossi, M., Malet E., Garcia-Sellés, D., 2020. Climatic and structural controls on Late-glacial and Holocene rockfall occurrence in high-elevated rock walls of the Mont Blanc massif (Western Alps). Earth Surface Processes and Landforms 45, 3071–3091. https://doi.org/10.1002/esp.4952

Gardent, M., Rabatel, A., Dedieu, J.P., Deline, P., 2014. Multitemporal glacier inventory of the French Alps from the late 1960s to the late 2000s. Glob. Planet. Change 120, 24–37. https://doi.org/10.1016/j.gloplacha.2014.05.004

Goehring, B.M., Schaefer, J.M., Schlüchter, C., Lifton, N.A., Finkel, R.C., Jull, A.J.T., Akçar, N., Alley, R.B., 2011. The Rhone Glacier was smaller than today for most of the Holocene. Geology 39, 679–682. https://doi.org/10.1130/G32145.1

Gross, G., Kerschner, H., Patzelt, G., 1977. Methodische Untersuchungen uber die Schneegrenze in alpinen Gletschergebieten. Z. für Gletscherkd. Glazialgeol. 7, 223–251.

Gschwentner, P., Kerschner, H., Spötl, C., 2020. Late Glacial ice advance in the Kellerjoch region near Schwaz (Tyrol, Eastern Alps). Austrian Journal of Earth Sciences 113, 2, 211–227. https://doi.org/10.17738/ajes.2020.0013

Guillot, S., di Paola, S., Menot, R. P., Ledru, P., Spalla, M. I., Gosso, G., Schwartz, S., 2009. Suture zones and importance of strike-slip faulting for Variscan geodynamic reconstructions of the External Crystalline Massifs of the western Alps. Bulletin de la Societe Géologique de France 180, 6, 483–500. https://doi.org/10.2113/gssgfbull.180.6.483

Haas, J.N., Richoz, I., Tinner, W., Wick, L., 1998. Synchronous Holocene climatic oscillations recorded on the Swiss Plateau and at timberline in the Alps. Holocene 8, 3, 301–309. https://doi.org/10.1191/095968398675491173

Heiri, O., Ilyashuk, B., Millet, L., Samartin, S., Lotter, A.F., 2015. Stacking of discontinuous regional palaeoclimate records: Chironomid-based summer temperatures from the Alpine region. The Holocene 25, 1, 137–149. https://doi.org/10.1177/0959683614556382

Helbronner, P. 1935. Description géométrique détaillée des Alpes françaises, tome X, Gauthier Villars, Paris.

Henz, A., Reinthaler, J., Nussbaumer, S., Jouvet, G., Vieli, A., 2024. Alpine-wide LIA glacier reconstruction and ELA patterns using glacier modelling. EGU General Assembly 2024, Vienna, Austria, 14–19 Apr 2024, EGU24-4111. https://doi.org/10.5194/egusphere-egu24-4111

Hepp, J., Wüthrich, L., Bromm, T., Bliedtner, M., Schäfer, I. K., Glaser, B., Rozanski, K., Sirocko, F., Zech, R., Zech, M., 2019. How dry was the Younger Dryas? Evidence from a coupled δ^2H–δ^{18}O biomarker paleohygrometer applied to the Gemündener Maar sediments, Western Eifel, Germany. Clim. Past, 15, 713–733. https://doi.org/10.5194/cp-15-713-2019

Hertl, A., 2001. Untersuchungen zur spätglazialen Gletscher- und Klimageschichte der österreichischen Silvrettagruppe. Institute of Geography, University of Innsbruck, 265 pp.

Hewitt, K., 2009. Rock avalanches that travel onto glaciers and related developments, Karakoram Himalaya, Inner Asia. Geomorphology 103, 1, 66–79. https://doi.org/10.1016/j.geomorph.2007.10.017

Hilger, P., Gosse, J.C., Hermanns, R.L., 2019. How significant is inheritance when dating rockslide boulders with terrestrial cosmogenic nuclide dating? – a case study of an historic event. Landslides 16, 729–738. https://doi.org/10.1007/s10346-018-01132-0

Hilger, P., Hermanns, R.L., Czekirda, J., Myhra, K.S., Gosse, J.C., Etzelmüller, B., 2021. Permafrost as a first order control on long-term rock-slope deformation in (Sub-)Arctic Norway. Quaternary Science Reviews 251, 106718. https://doi.org/10.1016/j.quascirev.2020.106718

Hirtlreiter, G., 1992. Spät- und postglaziale Gletscherschwankungen im Wettersteingebirge und seiner Umgebung. Dissertation, University of Munich. 154 pp.

2053 Hofmann, F.M., Alexanderson H., Schoeneich P., Mertes, J.R., Léanni L., 2019. Post-Last Glacial
2054 Maximum glacier fluctuations in the southern Écrins massif (westernmost Alps): insights from ^{10}Be
2055 cosmic ray exposure dating. Boreas 48, 4, 1019–1041. https://doi.org/10.1111/bor.12405

2056 Holzhauser, H., 2010. Zur Geschichte des Gornergletschers – Ein Puzzle aus historischen Dokumenten
2057 und fossilen Hölzern aus dem Gletschervorfeld. Geographica Bernensia. 253 pp.

2058 Holzhauser, H., 2016. Auf dem Holzweg zur frühen Geschichte des Unteren Grindelwaldgletschers –
2059 was uns alte Bäume aus den Ufermoränen erzählen. In: Zumbühl, H.J., Nussbaumer, S.U., Holzhauser,
2060 H. (Eds.) Die Grindelwaldgletscher – Kunst und Wissenschaft. Bern: Haupt, 177–188.

2061 Holzhauser, H., Magny, M., Zumbuhl, H.J., 2005. Glacier and lake-level variations in west-central
2062 Europe over the last 3500 years. The Holocene 15, 789–801.
2063 https://doi.org/10.1191/0959683605hl853ra

2064 Hughes, P.D., Gibbard, P.L., 2015 A stratigraphical basis for the Last Glacial Maximum (LGM),
2065 Quatern. Intern. 383, 174–185. https://doi.org/10.1016/j.quaint.2014.06.006

2066 Huss, M., Funk, M., Ohmura, A., 2009. Strong Alpine glacier melt in the 1940s due to enhanced solar
2067 radiation. Geophys. Res. Lett. 36, L23501. https://doi.org/10.1029/2009GL040789

2068 Hutchinson, M.F., 1989. A new procedure for gridding elevation and streamline data with automatic
2069 removal of spurious pits. J. Hydrol. 106, 211–232. https://doi.org/10.1016/0022-1694(89)90073-5

2070 Ilyashuk, B., Gobet, E., Heiri, O., Lotter, A.F., van Leeuwen, J.F.N., van der Knaap,W.O., Ilyashuk,
2071 E., Oberli, F., Ammann, B., 2009. Lateglacial environmental and climatic changes at the Maloja Pass,
2072 Central Swiss Alps, as recorded by chironomids and pollen. Quat. Sci. Rev. 28, 1340–1353.
2073 https://doi.org/10.1016/j.quascirev.2009.01.007

2074 Ilyashuk, E.A., Koinig, K.A., Heiri, O., Ilyashuk, B.P., Psenner, R., 2011. Holocene temperature
2075 variations at a high-altitude site in the Eastern Alps: a chironomid record from Schwarzsee ob Solden,
2076 Austria. Quat. Sci. Rev. 30, 176–191. https://doi.org/10.1016/j.quascirev.2010.10.008

2077 Ivy-Ochs, S., 2015. Glacier Variations in the European Alps at the End of the Last Glaciation. Cuad.
2078 Investig. Geogr. 41, 295–315. https://doi.org/10.18172/cig.2750

2079 Ivy-Ochs, S., Kerschner, H., Kubik, P.W. and Schlüchter, C., 2006a. Glacier response in the European
2080 Alps to Heinrich Event 1 cooling: the Gschnitz stadial. J. Quaternary Sci. 21, 115-130.
2081 https://doi.org/10.1002/jqs.955

2082 Ivy-Ochs, S., Kerschner, H., Reuther, A., Maisch, M., Sailer, R., Schaefer, J., Kubik, P.W., Synal,
2083 H.A., Schlüchter, Ch., 2006b. The timing of glacier advances in the northern European Alps based on
2084 surface exposure dating with cosmogenic 10Be, 26Al, 36Cl, and 21Ne. In: Siame, L.L., Bourlès, D.L.,
2085 Brown, E.T. (Eds.), In Situ– Produced Cosmogenic Nuclides and Quantification of Geological
2086 Processes: Geological Society of America Special Paper, vol. 415, 43–60.
2087 https://doi.org/10.1130/2006.2415(04)

2088 Ivy-Ochs, S., Kerschner, H., Maisch, M., Christl, M., Kubik, P. W., Schlüchter, C., 2009. Latest
2089 Pleistocene and Holocene glacier variations in the European Alps. Quaternary Sci Rev, 28, 2137–
2090 2149. https://doi.org/10.1016/j.quascirev.2009.03.009

2091 Jaillet S., Ballandras S., 1999. La transition Tardiglaciaire/Holocène à travers les fluctuations du
2092 glacier du Tour (vallée de Chamonix, Alpes du nord françaises). Quaternaire 10, 15–23.
2093 https://doi.org/10.3406/quate.1999.1625

Jamieson, S.S.R., Ewertowski, M.W., Evans, D.J.A., 2015. Rapid advance of two mountain glaciers in response to mine-related debris loading. Journal of Geophysical Research: Earth Surface, 120, 7, 1418–1435. https://doi.org/10.1002/2015JF003504

Joannin, S., Vannière, B., Galop, D., Peyron, O., Haas, J. N., Gilli, A., Chapron, E., Wirth, S. B., Anselmetti, F., Desmet, M., and Magny, M., 2013. Climate and vegetation changes during the Lateglacial and early–middle Holocene at Lake Ledro (southern Alps, Italy). Clim. Past 9, 913–933. https://doi.org/10.5194/cp-9-913-2013

Joerin, U.E., 2006. Holocene glacier fluctuations in the Swiss Alps. PhD thesis, University of Bern, 106 pp.

Joerin, U.E., Nicolussi, K., Fischer, A., Stocker, T.F., Schlüchter, C., 2008. Holocene optimum events inferred from subglacial sediments at Tschierva Glacier, Eastern Swiss Alps. Quaternary Science Reviews 27, 3-4, 337–350. https://doi.org/10.1016/j.quascirev.2007.10.016

Jomelli, V., Swingedouw, D., Vuille, M., Favier, V., Goehring, B., Shakun, J., Braucher, R., Schimmelpfennig, I., Menviel, L., Rabatel, A., Martin, L.C.P., Blard, P.-H., Condom, T., Lupker, M., Christl, M., He, Z., Verfaillie, D., Gorin, A. Aumaître, G., Bourlès, D.L., Keddadouche, K., 2022. In-phase millennial-scale glacier changes in the tropics and North Atlantic regions during the Holocene. Nat. Commun. 13, 1419. https://doi.org/10.1038/s41467-022-28939-9

Jones, D.B., Harrison, S., Anderson, K., 2019. Mountain glacier-to-rock glacier transition. Global and Planetary Change 181, 102999. https://doi.org/10.1016/j.gloplacha.2019.102999

Kaufman, D., McKay, N., Routson, C., Erb M., Dätwyler C., Sommer P.S., Heiri O., Davis B., 2020. Holocene global mean surface temperature, a multi-method reconstruction approach. Sci Data 7, 201. https://doi.org/10.1038/s41597-020-0530-7

Kenner, R., Magnusson, J., 2017. Estimating the effect of different influencing factors on rock glacier development in two regions in the Swiss Alps. Permafrost and Periglacial Processes 28, 1, 195–208. https://doi.org/10.1002/ppp.1910

Kern, Z., László, P., 2010. Size specific steady-state accumulation-area ratio: an improvement for equilibrium-line estimation of small palaeoglaciers. Quaternary Science Reviews 29, 19–20, 2781–2787. https://doi.org/10.1016/j.quascirev.2010.06.033

Kerschner, H., 1990. Methoden der Schneegrenzbestimmung. In: Liedtke, H. (Ed.), Eiszeitforschung. Wissenschaftliche Buchgesellschaft, Darmstadt, 299–311.

Kerschner, H., Ivy-Ochs, S., 2008. Palaeoclimate from glaciers: Examples from the Eastern Alps during the Alpine Lateglacial and early Holocene. Global and Planetary Change 60, 1–2, 58–71. https://doi.org/10.1016/j.gloplacha.2006.07.034

Kerschner, H., Kaser, G., Sailer, R., 2000. Alpine Younger Dryas glaciers as palaeo-precipitation gauges. Ann. Glaciol. 31, 80–84. https://doi.org/10.3189/172756400781820237

Kirkbride, M.P., Winkler, S., 2012. Correlation of Late Quaternary moraines: impact of climate variability, glacier response, and chronological resolution. Quaternary Science Reviews 46, 1–29. https://doi.org/10.1016/j.quascirev.2012.04.002

Knight, J., Harrison, S., Jones, D.B., 2019. Rock glaciers and the geomorphological evolution of deglacierizing mountains. Geomorphology 324, 14–24. https://doi.org/10.1016/j.geomorph.2018.09.020

Koinig, K., Nicolussi, K., Moernaut, J., Huang, J.-J.S., Tessadri, R., Ilyashuk, E., Strasser, M., Psenner, R., Ilyashuk, B., 2019. Timing the Little Ice Age Advance and Fluctuations of a Glacier in the Eastern Alps - a Multi-Proxy Lake Sediment Study. INQUA Dublin, 27th July, 2019, O-2093.

Korschinek, G., Bergmaier, A., Faestermann, T., Gerstmann, U.C., Knie, K., Rugel, G., Wallner, A., Dillmann, I., Dollinger, G., von Gostomski Lierse, Ch, Kossert, K., Maitia, M., Poutivtsev, M., Remmert, A., 2010. A new value for the half-life of ^{10}Be by heavy-ion elastic recoil detection and liquid scintillation counting. Nucl. Instrum. Methods Phys. Res. B 268 (2), 187–191. https://doi.org/10.1016/j.nimb.2009.09.020

Kronig O., Ivy-Ochs S., Hajdas I., Christl M., Wirsig C., Schlüchter C., 2018. Holocene evolution of the Triftje- and the Oberseegletscher (Swiss Alps) constrained with ^{10}Be exposure and radiocarbon dating. Swiss Journal of Geosciences 111, 117–131. https://doi.org/10.1007/s00015-017-0288-x

Lagier, T., Masson, S., 1997. Les glaciers de la Vallouise (glacier Blanc, glacier Noir), héritages holocène et évolution climatique. MSc thesis, Université Aix-Marseille I, 86 pp.

Lahousse, P., Guen, R., 1998. Le lac proglaciaire d'Arsine (Alpes françaises, massif du Pelvoux): un risque de vidange brutale définitivement écarté? Revue de Géographie Alpine 86, 3, 49–59. https://doi.org/10.3406/rga.1998.2891

Lapellegerie, P., Millet, L., Rius, D., Duprat-Oualid, F., Luoto, T., Heiri, O., 2024. Chironomid-inferred summer temperature during the Last Glacial Maximum in the Southern Black Forest, Central Europe. Quaternary Science Reviews, Volume 345, 109016. https://doi.org/10.1016/j.quascirev.2024.109016

Leclercq, P.W. and Oerlemans, J., 2012. Global and Hemispheric Temperature Reconstruction from Glacier Length Fluctuations. Climate Dynamics 38, 1065–1079. http://dx.doi.org/10.1007/s00382-011-1145-7

Leemann, A., Niessen, F., 1994. Holocene glacial activity and climatic variations in the Swiss Alps: reconstructing a continuous record from proglacial lake sediments. Holocene 4, 3 259–268. https://doi.org/10.1177/095968369400400305

Legay, A., Magnin, F., Ravanel, L., 2021. Rock temperature prior to failure: analysis of 209 rockfall events in the Mont Blanc massif (Western European Alps). Permafrost Periglacial 32, 520–536. https://doi.org/10.1002/ppp.2110

Leger, T.P.M., Hein, A.S., Bingham, R.G., Rodés, Á., Fabel, D., Smedley, R.K., 2021. Geomorphology and 10Be chronology of the Last Glacial Maximum and deglaciation in northeastern Patagonia, 43°S-71°W. Quaternary Science Reviews 272, 107194. https://doi.org/10.1016/j.quascirev.2021.107194

Leger, T.P.M., Jouvet, G., Kamleitner, S., Mey, J., Herman, F., Finley, B.D., Ivy-Ochs, S., Vieli, A., Henz, A., Nussbaumer, S.U., 2025. A data-consistent model of the last glaciation in the Alps achieved with physics-driven AI. Nat. Commun. 16, 848. https://doi.org/10.1038/s41467-025-56168-3

Lehmann, B., Anderson, R.S., Bodin, X., Cusicanqui, D., Valla, P.G., Carcaillet, J., 2022. Alpine rock glacier activity over Holocene to modern timescales (western French Alps), Earth Surf. Dynam. 10, 605–633. https://doi.org/10.5194/esurf-10-605-2022

Le Roy, M., 2012. Reconstitution des fluctuations glaciaires holocènes dans les Alpes occidentales – apports de la dendrochronologie et des datations par isotopes cosmogéniques produits *in situ*. PhD thesis, Université de Savoie, 360 pp.

Le Roy, M., Nicolussi, K., Deline, P., Astrade, L., Edouard, J.L., Miramont, C., Arnaud, F., 2015. Calendar-dated glacier variations in the western European Alps during the neoglacial: the Mer de Glace record, Mont Blanc massif. Quat. Sci. Rev. 108, 1–22. https://doi.org/10.1016/j.quascirev.2014.10.033

Le Roy, M., Deline, P., Carcaillet, J., Schimmelpfennig, I., Ermini, M., ASTER Team, 2017. ^{10}Be exposure dating of the timing of Neoglacial glacier advances in the Ecrins-Pelvoux massif, southern French Alps. Quat. Sci. Rev. 178, 118–138. https://doi.org/10.1016/j.quascirev.2017.10.010

Le Roy, M., Nicolussi, K., Schlüchter, C., 2023. Tree-ring Dating of the Little Ice Age Maxima of Arolla Glaciers (Valais, Switzerland). Journal of Alpine Research | Revue de géographie alpine, 111-2. https://doi.org/10.4000/rga.12170

Le Roy, M., Ivy-Ochs, S., Nicolussi, K., Monegato, G., Reitner, J.M., Colucci, R.R., Ribolini, A., Spagnolo, M., Stoffel, M., 2024. Chapter 20 - Holocene glacier variations in the Alps. In: Palacios, D., Hughes, P.D., Jomelli, V., Tanarro, L.M. (Eds.) European Glacial Landscapes: The Holocene. Elsevier, Amsterdam. 367–418. https://doi.org/10.1016/B978-0-323-99712-6.00018-0

Li, H., Spötl, C., Cheng, H., 2021. A high-resolution speleothem proxy record of the Late Glacial in the European Alps: extending the NALPS19 record until the beginning of the Holocene. J. Quaternary Sci. 36, 1, 29–39. https://doi.org/10.1002/jqs.3255

Lifton, N.A., 2016. Implications of two Holocene time-dependent geomagnetic models for cosmogenic nuclide production rate scaling. Earth Planet. Sci. Lett. 433, 257–268. http://dx.doi.org/10.1016/j.epsl.2015.11.006

Lifton, N.A., Sato, T., Dunai, T.J., 2014. Scaling in situ cosmogenic nuclide production rates using analytical approximations to atmospheric cosmic-ray fluxes. Earth Planet. Sci. Lett. 386, 149–160. http://dx.doi.org/10.1016/j.epsl.2013.10.052

Lichtenecker, N., 1938. Die Gegenwärtige und die Eiszeitliche Schneegrenze in den Ostalpen. In: Götzinger, G. (Ed.), Verhandlungen der III Internationalen Quartärkonferenz. INQUA, Vienna, 141–147.

Lory, P., 1908. Révision des feuilles de Grenoble et de Vizille. Bulletin de la Carte géologique de France 119, t. XVIII, 187 pp.

Luetscher, M., Hoffmann, D.L., Frisia, S., Spötl, C., 2011. Holocene glacier history from alpine speleothems, Milchbach cave, Switzerland. Earth and Planetary Science Letters 302, 95–106. https://doi.org/10.1016/j.epsl.2010.11.042

Lukas, S., Bradwell, T., 2010. Reconstruction of a Lateglacial (Younger Dryas) mountain ice field in Sutherland, northwestern Scotland, and its palaeoclimatic implications. Journal of Quaternary Science 25, 567–580. https://doi.org/10.1002/jqs.1376

Luterbacher, J., Werner, J. P., Smerdon, J. E., Fernández-Donado, L., González-Rouco, F. J., Barriopedro, D., et al., 2016. European summer temperatures since Roman times. Environmental Research Letters 11, 024001. https://doi.org/10.1088/1748-9326/11/2/024001

Mackintosh, A.N., Anderson, B.M., Pierrehumbert, R.T., 2017. Reconstructing Climate from Glaciers. Annual Review of Earth and Planetary Sciences 2017 45, 1, 649–680. https://doi.org/10.1146/annurev-earth-063016-020643

Magny, M., 2013. Orbital, ice-sheet, and possible solar forcing of Holocene lake-level fluctuations in west-central Europe: A comment on Bleicher. The Holocene 23, 8, 12021212. https://doi.org/10.1177/0959683613483627

Magny, M., Vannière, B., de Beaulieu, J.-L., Bégeot, C., Heiri, O., Millet, L., Peyron, O., and Walter-Simonnet, A.-V., 2007. Early-Holocene climatic oscillations recorded by lake-level fluctuations in west-central Europe and in central Italy. Quaternary Sci. Rev. 26, 1951–1964. https://doi.org/10.1016/j.quascirev.2006.04.013

Maisch, M., 1981. Glazialmorphologische und gletschergeschichtliche Untersuchungen im Gebiet zwischen Landwasser- und Albulatal (Kt. Graubünden, Schweiz). Phys. Geogr. 3, 215 pp.

Maisch, M. 1987. Zur Gletschergeschichte des alpinen Spätglazials: Analyse und Interpretation von Schneegrenzdaten. Geographica Helvetica 42, 2, 63–71.

Maisch, M., Wipf, A., Denneler, B., Battaglia, J., Benz, C., 2000. Die Gletscher der Schweizer Alpen: Gletscherhochstand 1850, Aktuelle Vergletscherung, Gletscherschwund-Szenarien. (Schlussbericht NFP 31). 2. Auflage. vdf Hochschulverlag an der ETH Zürich, 373 pp.

Marcer, M., Bodin, X., Brenning, A., Schoeneich, P., Charvet, R., Gottardi, F., 2017. Permafrost Favorability Index: Spatial Modeling in the French Alps Using a Rock Glacier Inventory. Frontiers in Earth Science 5. https://doi.org/10.3389/feart.2017.00105

Martin, D., 1933. II. Observations sur la neige et les glaciers méridionaux du Pelvoux. In: Études Glaciologiques, tome 7, Études glaciologiques 1920-1930. 272–294.

Martin, C., Ménot, G., Thouveny, N., Peyron, O., Andrieu-Ponel, V., Montade, V., … Bard, E., 2020a. Early Holocene Thermal Maximum recorded by branched tetraethers and pollen in Western Europe (Massif Central, France). Quaternary Science Reviews 228, 106109. https://doi.org/10.1016/j.quascirev.2019.106109

Martin, L.C.P., Blard, P.-H., Balco, G., Lavé, J., Delunel, R., Lifton, N., Laurent, V., 2017. The CREp program and the ICE-D production rate calibration database: A fully parameterizable and updated online tool to compute cosmic-ray exposure ages. Quat. Geochronol. 38, 25–49. https://doi.org/10.1016/j.quageo.2016.11.006

Martin, L.C.P., Blard, P.-H., Lavé, J., Jomelli, V., Charreau, J., Condom, T., Lupker, M., ASTER Team, 2020b. Antarctic-like temperature variations in the Tropical Andes recorded by glaciers and lakes during the last deglaciation. Quaternary Science Reviews 247, 106542. https://doi.org/10.1016/j.quascirev.2020.106542

Matthews, J.A., Winkler, S., Wilson, P., Tomkins, M.D., Dortch, J.M., Mourne, R.W., Hill, J.L., Owen, G., Vater, A.E., 2018. Small rock-slope failures conditioned by Holocene permafrost degradation: a new approach and conceptual model based on Schmidt-hammer exposure-age dating, Jotunheimen, southern Norway. Boreas 47, 1144–1169. https://doi.org/10.1111/bor.12336

Mekhaldi, F., Czymzik, M., Adolphi, F., Sjolte, J., Björck, S., Aldahan, A., Brauer, A., Martin-Puertas, C., Possnert, G., Muscheler, R., 2020. Radionuclide wiggle matching reveals a nonsynchronous early Holocene climate oscillation in Greenland and western Europe around a grand solar minimum, Clim. Past, 16, 1145–1157. https://doi.org/10.5194/cp-16-1145-2020.

Menounos, B., Clague, J.J., Clarke, G.K C., Marcott, S.A., Osborn, G., Clark, P.U., Tennant C., Novak, A.M., 2013. Did rock avalanche deposits modulate the late Holocene advance of Tiedemann Glacier, southern Coast Mountains, British Columbia, Canada? Earth and Planetary Science Letters 384, 154–164. https://doi.org/10.1016/j.epsl.2013.10.008

Merchel, S., Herpers, U., 1999. An update on radiochemical separation techniques for the determination of long-lived radionuclides via Accelerator Mass Spectrometry. Radiochim. Acta 84, 215–219. https://doi.org/10.1524/ract.1999.84.4.215

Monjuvent, G., 1973. La transfluence Durance-Isère. Essai de synthèse du Quaternaire du bassin du Drac (Alpes françaises). Géol. alpine, 49, 57–118.

Moran, A. P., Kerschner, H., Ochs, S.I., 2016a. Redating the moraines in the Kromer Valley (Silvretta Mountains) – New evidence for an early Holocene glacier advance. The Holocene 26, 4, 655–664. https://doi.org/10.1177/0959683615612571

Moran, A. P., Ivy-Ochs, S., Schuh, M., Christl, M., Kerschner, H., 2016b. Evidence of central Alpine glacier advances during the Younger Dryas–early Holocene transition period. Boreas 45, 3, 398–410. https://doi.org/10.1111/bor.12170

Moran, A.P., Ivy Ochs, S., Vockenhuber, C., Kerschner, H., 2016c. Rock glacier development in the Northern Calcareous Alps at the Pleistocene-Holocene boundary. Geomorphology 273, 178–188. https://doi.org/10.1016/j.geomorph.2016.08.017

Moran, A.P., Ivy-Ochs, S., Vockenhuber, C., and Kerschner, H., 2017a. First ^{36}Cl exposure ages from a moraine in the Northern Calcareous Alps, E&G Quaternary Sci. J. 65, 145–155. https://doi.org/10.3285/eg.65.2.03

Moran, A.P., Ivy Ochs, S., Christl, M., Kerschner, H., 2017b. Exposure dating of a pronounced glacier advance at the onset of the late-Holocene in the central Tyrolean Alps. The Holocene 27, 9, 1350–1358. https://doi.org/10.1177/0959683617690589

Munroe, J.S., Laabs, B.J.C., Corbett, L.B., Bierman, P.R., Handwerger, A.L., 2024. Rock glacier movement and debris transport over annual to multi-millennial timescales. Journal of Geophysical Research: Earth Surface, 129, e2023JF007453. https://doi.org/10.1029/2023JF007453

Nicoletti, P.G., Sorriso-Valvo, M., 1991. Geomorphic controls on the shape and mobility of rock avalanches. Geological Society of America Bulletin 103, 1365–1373.

Nicolussi, K., 2011. Gletschergeschichte der Pasterze e Spurensuche in die nacheiszeitliche Vergangenheit. In: Die Pasterze - Der Gletscher am Großglockner. Pustet, Salzburg, 24–27.

Nicolussi, K., Patzelt, G., 2000. Discovery of early-Holocene wood and peat on the forefield of the Pasterze glacier, Eastern Alps, Austria. The Holocene 10, 2, 191–199. https://doi.org/10.1191/095968300666855842

Nicolussi, K., Patzelt, G., 2001. Untersuchungen zur holozänen Gletscherentwicklung von Pasterze und Gepatschferner (Ostalpen). Z. Gletsch. Glazialgeol., 36, 1–87.

Nicolussi, K., Schlüchter, C., 2012. The 8.2 ka event – Calendar-dated glacier response in the Alps. Geology 40, 819–822. https://doi.org/10.1130/G32406.1

Nicolussi, K., Jörin, U., Kaiser, K.F., Patzelt, G., Thurner, A., 2006. Precisely dated glacier fluctuations in the Alps over the last four millennia. In: Price, M.F. (Ed.) Global Change in Mountain Regions. Sapiens Publishing, 59–60.

Nicolussi, K., Dusch, M., Drescher-Schneider, R., Kellerer-Pirklbauer, A., Le Roy, M., Maussion, F., Schlüchter, C., 2019. Glacier evolution in the Alps during the early and mid-Holocene - new results from Tschierva and Pasterze glaciers. INQUA Dublin, 27th July, 2019, P-2451. http://dx.doi.org/10.13140/RG.2.2.27658.21447

Nicolussi, K., Dusch, M., Drescher-Schneider, R., Kellerer-Pirklbauer, A., Maussion, F., 2020. Always delayed? Holocene and current evolution of Pasterze Glacier, Austria, EGU General Assembly 2020, Online, 4–8 May 2020, EGU2020-9317. https://doi.org/10.5194/egusphere-egu2020-9317

Nicolussi, K., Le Roy M., Schlüchter, C., Wacker L., Stoffel M., 2022. The glacier advance at the onset of the Little Ice Age in the Alps – new evidence from Mont Miné and Morteratsch glaciers. The Holocene 32, 7, 624–638. https://doi.org/10.1177/09596836221088247

Oien, R., Rea, B., Spagnolo, M., Barr, I., Bingham, R., 2022. Testing the area–altitude balance ratio (AABR) and accumulation–area ratio (AAR) methods of calculating glacier equilibrium-line altitudes. Journal of Glaciology 68, 268, 357–368. https://doi.org/10.1017/jog.2021.100

Orombelli, G., 2005. Il Ghiacciaio del Ruitor (Valle d'Aosta) nella piccola etá glaciale. Geografia Fisica e Dinamica Quaternaria, Suppl. VII, 239–251.

Orombelli, G., Porter, S., 1982. Late Holocene fluctuations of Brenva Glacier. Geografia Fisica e Dinamica Quaternaria 5, 14–37.

Ortu, E., Peyron, O., Bordon, A., de Beaulieu, J.L., Siniscalco, C., Caramiella, R., 2008. Lateglacial and Holocene climate oscillations in the South-western Alps: an attempt at quantitative reconstruction. Quaternary International 190, 71–88. https://doi.org/10.1016/j.quaint.2008.04.004

Parriaux, A., Nicoud, G.F., 1990. Hydrological behaviour of glacial deposits in mountainous areas. In: Molnár, L. (Ed.), Hydrology of Mountainous Areas: International Association of Hydrological Sciences, Publication, 190, 291–311.

Patzelt, G., 2016. Das Bunte Moor in der Oberfernau (Stubaier Alpen, Tirol) – Eine neu bearbeitete Schlüsselstelle für die Kenntnis der nacheiszeitlichen Gletscherschwankungen der Ostalpen. Jahrbuch der Geologischen Bundesanstalt Band 156, 97–107.

Pearson, C., Sigl, M., Burke, A., Davies, S., Kurbatov, A., Severi, M., Cole-Dai, J., Innes, H., Albert, P.G., Helmick, M., 2022. Geochemical ice-core constraints on the timing and climatic impact of Aniakchak II (1628 BCE) and Thera (Minoan) volcanic eruptions. PNAS Nexus 1, 2, pgac048. https://doi.org/10.1093/pnasnexus/pgac048

Pellitero, R., Rea, B.R., Spagnolo, M., Bakke, J., Hughes, P., Ivy-Ochs, S., Lukas, S., Ribolini, A., 2015. A GIS tool for automatic calculation of glacier equilibrium-line altitudes. Comput. Geosci. 82, 55–62. https://doi.org/10.1016/j.cageo.2015.05.005

Pendleton, S., Miller, G., Lifton, N., Young, N., 2019. Cryosphere response resolves conflicting evidence for the timing of peak Holocene warmth on Baffin Island, Arctic Canada, Quaternary Science Reviews 216, 107–115. https://doi.org/10.1016/j.quascirev.2019.05.015

Pindur P., Heuberger H. 2010. Zur holozänen Gletschergeschichte im Zemmgrund in den Zillertaler Alpen, Tirol (Ostalpen). Zeitschrift für Gletscherkunde und Glazialgeologie, Bd. 42 (2008), H. 2, S. 21–89.

Porter, T.J., Schoenemann, S.W., Davies, L.J., Steig, E.J., Bandara, S., Froese, D.G., 2019. Recent summer warming in northwestern Canada exceeds the Holocene thermal maximum. Nature Communications 10, 1631. https://doi.org/10.1038/s41467-019-09622-y

Prager, C., Zangerl, C., Patzelt, G., Brandner, R., 2008. Age distribution of fossil landslides in the Tyrol (Austria) and its surrounding areas. Nat. Hazards Earth Syst. Sci. 8, 377–407. https://doi.org/10.5194/nhess-8-377-2008

Prochnow, M., Hepp, J., Strobel, P., Zech, R., Acharya, S., Szidat, S., Rius, D., Millet, L., Glaser, B., Zech, M., 2024. Late Glacial summer paleohydrology across Central Europe. Sci. Rep. 14, 30546. https://doi.org/10.1038/s41598-024-83189-7

Protin, M., Schimmelpfennig, I., Mugnier, J.-L., Ravanel, L., Le Roy, M., Deline, P., Favier, V., Buoncristiani J-F., ASTER Team., 2019. Climatic reconstruction for the Younger Dryas/Early Holocene transition and the Little Ice Age based on paleo-extents of Argentière glacier (French Alps). Quaternary Science Reviews 221, 105863. https://doi:10.1016/j.quascirev.2019.105863

Protin, M., Schimmelpfennig, I., Mugnier, J.-L., Buoncristiani, J.-F., Le Roy, M., Pohl, B., Moreau, L., ASTER Team, 2021. Millennial-scale deglaciation across the European Alps at the transition between the Younger Dryas and the Early Holocene – evidence from a new cosmogenic nuclide chronology. Boreas 50, 3, 671–685. https://doi.org/10.1111/bor.12519

Putnam, A.E., Schaefer, J.M., Barrell, D.J.A., Vandergoes, M.J., Denton, G.H., Kaplan, M.R., Finkel, R.C., Schwartz, R., Goehring, B.M., Kelley, S.E., 2010. In situ cosmogenic 10Be production-rate calibration from the Southern Alps, New Zealand. Quat. Geochronol. 5, 392–409. https://doi.org/10.1016/j.quageo.2009.12.001

Rasmussen, S.O., Vinther, B.M., Clausen, H.B., Andersen, K.K., 2007. Early Holocene climate oscillations recorded in three Greenland ice cores. Quaternary Sci. Rev. 26, 1907–1914. https://doi.org/10.1016/j.quascirev.2007.06.015

Rabatel, A., Letréguilly, A., Dedieu, J.-P., Eckert, N., 2013. Changes in glacier equilibrium-line altitude in the western Alps from 1984 to 2010: evaluation by remote sensing and modeling of the morpho-topographic and climate controls. The Cryosphere 7, 1455–1471. https://doi.org/10.5194/tc-7-1455-2013

Ravanel, L., Deline, P., 2011. Climate influence on rockfalls in high-Alpine steep rockwalls: the north side of the Aiguilles de Chamonix (Mont Blanc massif) since the end of the 'Little Ice Age'. The Holocene 21, 2, 357–365. https://doi.org/10.1177/0959683610374887

Rea, B.R., 2009. Defining modern day Area-Altitude Balance Ratios (AABRs) and their use in glacier-climate reconstructions. Quat. Sci. Rev. 28, 237–248. https://doi.org/10.1016/j.quascirev.2008.10.011

Rea, B.R., Pellitero, R., Spagnolo, M., Hughes, P., Ivy-Ochs, S., Renssen, H., Ribolini, A., Bakke, J., Lukas, S., Braithwaite, R.J., 2020. Atmospheric circulation over Europe during the Younger Dryas. Science Advances 6, 50. https://doi.org/10.1126/sciadv.aba4844

Reimer, P.J., Austin, W.E.N., Bard, E., et al. The IntCal20 Northern Hemisphere Radiocarbon Age Calibration Curve (0–55 cal kBP). Radiocarbon 62, 4, 725–757. https://doi.org/10.1017/RDC.2020.41

Reinthaler, J., Paul, F., 2024. Assessment of methods for reconstructing Little Ice Age glacier surfaces on the examples of Novaya Zemlya and the Swiss Alps. Geomorphology 461, 109321. https://doi.org/10.1016/j.geomorph.2024.109321

Reinthaler, J., Paul, F., 2025. Reconstructed glacier area and volume changes in the European Alps since the Little Ice Age. The Cryosphere 19, 753–767. https://doi.org/10.5194/tc-19-753-2025

Reitner, J.M., Ivy-Ochs, S., Drescher-Schneider, R., Hajdas, I., Linner, M. 2016. Reconsidering the current stratigraphy of the Alpine Lateglacial: Implications of the sedimentary and morphological record of the Lienz area (Tyrol/Austria). E&G Quaternary Science Journal 65, 113–144. https://doi.org/10.3285/eg.65.2.02

Reitner, J.M., Ivy-Ochs, S., Steinemann, O., Lattner, D., Römer, A., 2020. The early Holocene Buchwiese rock avalanche (Eastern Alps, Austria): Geological conditions, kinematics, morphological and sedimentary legacy. Alpine and Mediterranean Quaternary 33, 2, 165–181. https://doi.org/10.26382/AMQ.2020.12

Reznichenko, N.V., Davies, T.R.H., Alexander, D.J., 2011. Effects of rock avalanches on glacier behaviour and moraine formation. Geomorphology 132, 3-4, 327–338. https://doi.org/10.1016/j.geomorph.2011.05.019

Reznichenko, N.V., Davies, T.R.H., Winkler, S., 2016. Revised palaeoclimatic significance of Mueller Glacier moraines, Southern Alps, New Zealand. Earth Surf. Process. Landforms 41, 196–207. https://doi.org/10.1002/esp.3848.

Roe, G.H., Christian, J.E., Marzeion, B., 2021. On the attribution of industrial-era glacier mass loss to anthropogenic climate change. The Cryosphere 15, 1889–1905. https://doi.org/10.5194/tc-15-1889-2021

Rodés, Á., 2020a. CEAA: Cosmogenic Exposure Age Averages (v1.2). https://doi.org/10.5281/zenodo.4024909

Rodés, Á., 2020b. CASC: Cosmo-Ages Sequence Calculator. https://github.com/angelrodes/CASC

Ronnert, L., Mickelson, D.M., 1992. High porosity of basal till at Burroughs glacier, southeastern Alaska. Geology 20, 9, 849–852. https://doi.org/10.1130/0091-7613(1992)020<0849:HPOBTA>2.3.CO;2

Röthlisberger, F., Schneebeli, W., 1979. Genesis of lateral moraine complexes, demonstrated by fossil soils and trunks: indicators of postglacial climatic fluctuations. In: Schlüchter, C. (Ed.), Moraines and Varves. Balkema, Rotterdam, 387–419.

Rowan, A.V., Egholm, D.L., Clark, C.D., 2022. Forward modelling of the completeness and preservation of palaeoclimate signals recorded by ice-marginal moraines. Earth Surface Processes and Landforms 47, 9, 2198–2208. https://doi.org/10.1002/esp.5371

Sailer, R., 2001. Späteiszeitliche Gletscherstände in der Ferwallgruppe. PhD thesis, Universität Innsbruck.

Samartin, S., Heiri, O., Vescovi, E., Brooks, S.J., Tinner, W., 2011. Lateglacial and early Holocene summer temperatures in the southern Swiss Alps reconstructed using fossil chironomids. Journal of Quaternary Science 27, 3, 279–289. https://doi.org/10.1002/jqs.1542

Samivel, 1978. Le Grand Oisans sauvage. Arthaud, 127 pp.

Scapozza, C., 2013. Stratigraphie, morphodynamique, paléoenvironnements des terrains sédimentaires meubles à forte déclivité du domaine périglaciaire alpin. Institut de géographie et durabilité de l'Université de Lausanne, Lausanne. Géovisions 40, 551 pp.

Schimmelpfennig, I., Schaefer, J.M., Akçar, N., Ivy-Ochs, S., Finkel, R.C., Schlüchter, C., 2012. Holocene glacier culminations in the Western Alps and their hemispheric relevance. Geology 40, 891–894. https://doi.org/10.1130/G33169.1

Schimmelpfennig, I., Schaefer, J.M., Akçar, N., Koffman, T., Ivy-Ochs, S., Schwartz, R., Finkel, R.C., Zimmerman, S., Schlüchter, C.A., 2014. Chronology of Holocene and Little ice age glacier culminations of the Steingletscher, central Alps, Switzerland, based on high-sensitivity beryllium-10 moraine dating. Earth Planet. Sci. Lett. 393, 220–230. https://doi.org/10.1016/j.epsl.2014.02.046

Schimmelpfennig, I., Schaefer, J. M., Lamp, J., Godard, V., Schwartz, R., Bard, E., Tuna, T., Akçar, N., Schlüchter, C., Zimmerman, S., ASTER Team, 2022. Glacier response to Holocene warmth inferred from in situ ^{10}Be and ^{14}C bedrock analyses in Steingletscher's forefield (central Swiss Alps). Clim. Past 18, 23–44. https://doi.org/10.5194/cp-18-23-2022

Schindelwig, I., 2010. The Last Glacial – Interglacial Transition: an interval of high alpine-glacier dynamics in the Central and Western Swiss Alps? Unpublished PhD thesis, Institute of Geology, University of Bern, 101 pp.

Schindelwig, I., Akçar, N., Kubik, P.W., Schlüchter, C., 2012. Lateglacial and early Holocene dynamics of adjacent valley glaciers in the Western Swiss Alps. Journal of Quaternary Science 27, 1, 114–124. https://doi.org/10.1002/jqs.1523

Schmidt, R., Kamenik, C., Kaiblinger, C., Tessadri, R., 2009. Klimaschwankungen und -trends des alteren Holozäns in den südlichen Niederen Tauern: multidisziplinäre Auswertung eines Sedimentkerns aus dem Oberen Landschitzsee (Lungau). In: Schmidt, R., Matulla, C., Psenner, R. (Eds.), Klimawandel in Österreich. Die letzten 20.000 Jahre. . . und ein Blick voraus. Innsbruck University Press, Innsbruck, 55–64.

Schneider, D., Huggel, C., Haeberli, W., Kaitna, R., 2011. Unravelling driving factors for large rock-ice avalanche mobility. Earth Surf. Process. Landforms 36, 1948–1966. https://doi.org/10.1002/esp.2218

Schoeneich, P., 1998. Les stades tardiglaciaires des Préalpes vaudoises et leur corrélation avec le modèle des Alpes orientales. ETHZ, VAW Mitteilungen 158, 192–207.

Schoeneich, P., Deline, P., Carcaillet, J., Schimmelpfennig, I., Bodin, X., Choler, P., Le Roy, M., 2019. Timing of Lateglacial moraines in the Northern and Western parts of the Ecrins massif (French Alps), INQUA 2019, Dublin, 25-31 July 2019.

Scotti, R., Brardinoni, F., Crosta, G.B., Cola, G., Mair, V., 2017. Time constraints for post-LGM landscape response to deglaciation in Val Viola, Central Italian Alps. Quat. Sci. Rev. 177, 10–33. https://doi.org/10.1016/j.quascirev.2017.10.011

Shugar, D.H., Clague, J.J., 2011. The sedimentology and geomorphology of rock avalanche deposits on glaciers. Sedimentology 58, 7, 1762–1783. https://doi.org/10.1111/j.1365-3091.2011.01238.x

Shulmeister J., Davies, T.R., Evans, D.J.A., Hyatt, O.M., Tovar, D.S., 2009. Catastrophic landslides, glacier behaviour and moraine formation – A view from an active plate margin. Quaternary Science Reviews 28, 11–12, 1085–1096. https://doi.org/10.1016/j.quascirev.2008.11.015

Sigl, M., Toohey, M., McConnell, J. R., Cole-Dai, J., Severi, M., 2022. Volcanic stratospheric sulfur injections and aerosol optical depth during the Holocene (past 11 500 years) from a bipolar ice-core array. Earth Syst. Sci. Data 14, 3167–3196. https://doi.org/10.5194/essd-14-3167-2022

Sissons, J.B., 1974. A lateglacial ice cap in the central Grampians, Scotland. Transactions of the Institute of British Geographers 62, 95–114. https://doi.org/10.2307/621517

Small, R.J., Beecroft, I.R., Stirling, D.M., 1984. Rates of Deposition on Lateral Moraine Embankments, Glacier De Tsidjiore Nouve, Valais, Switzerland. Journal of Glaciology 30, 106, 275–281. https://doi.org/10.3189/S0022143000006092

Smith, M.W., Carrivick, J.L., Quincey, D.J., 2015. Structure from motion photogrammetry in physical geography. Progress in Physical Geography 40, 2, 247–275. https://doi.org/10.1177/0309133315615805

Soldati, M., Borgatti, L., Cavallin, A., De Amicis, M., Frigerio, S., Giardino, M., Mortara, G., Pellegrini, G.B., Ravazzi, C., Surian, N., Tellini, C., Zanchi, A., in collaboration with Alberto, W., Albanese, D., Chelli, A., Corsini, A., Marchetti, M., Palomba, M., Panizza, M, 2006. Geomorphological evolution of slopes and climate changes in northern Italy during the Late

Quaternary: spatial and temporal distribution of landslides and landscape sensitivity implications. Geogr. Fis. Din. Quat. 29, 165–183.

Sommer, C., Malz, P., Seehaus, T. C., Lippl, S., Zemp, M., Braun, M.H., 2020. Rapid glacier retreat and downwasting throughout the European Alps in the early 21st century. Nature Communications 11, 3209. https://doi.org/10.1038/s41467-020-16818-0

Spencer, C., Yakymchuk, C., Ghaznavi, M., 2017. Visualising data distributions with kernel density estimation and reduced chi-squared statistic. Geoscience Frontiers 8, 1247–1252. https://doi.org/10.1016/j.gsf.2017.05.002

Steinemann, O., Ivy-Ochs, S., Hippe, K., Christl, M., Haghipour, N., Synal, H.-A., 2021. Glacial erosion by the Trift glacier (Switzerland): deciphering the development of riegels, rock basins and gorges. Geomorphology 375, 107533. https://doi.org/10.1016/j.geomorph.2020.107533

Stock, G.M., Uhrhammer, R.A., 2010. Catastrophic rock avalanche 3600 years BP from El Capitan, Yosemite Valley, California. Earth Surf. Process. Landforms 35, 941–951. https://doi.org/10.1002/esp.1982

Strand, P.D., Putnam, A.E., Schaefer, J.M., Denton, G.H., Barrell, D.J.A., 2024. Tracking rapid ice recession in a major Southern Alps valley during the last glacial termination. Quaternary Science Reviews 335, 108737. https://doi.org/10.1016/j.quascirev.2024.108737

The GlaMBIE Team, 2025. Community estimate of global glacier mass changes from 2000 to 2023. Nature 639, 382–388. https://doi.org/10.1038/s41586-024-08545-z

Uppala, S.M., KÅllberg, P.W., Simmons, A.J., Andrae, U., Bechtold, V.D.C., Fiorino, M., Gibson, J.K., Haseler, J., Hernandez, A., Kelly, G.A., Li, X., Onogi, K., Saarinen, S., Sokka, N., Allan, R.P., Andersson, E., Arpe, K., Balmaseda, M.A., Beljaars, A.C.M., Van De Berg, L., Bidlot, J., Bormann, N., Caires, S., Chevallier, F., Dethof, A., Dragosavac, M., Fisher, M., Fuentes, M., Hagemann, S., Holm, E., Hoskins, B.J., Isaksen, L., Janssen, P.A.E.M., Jenne, R., Mcnally, A.P., Mahfouf, J.-F., Morcrette, J.- J., Rayner, N.A., Saunders, R.W., Simon, P., Sterl, A., Trenberth, K.E., Untch, A., Vasiljevic, D., Viterbo, P., Woollen, J., 2005. The ERA-40 re-analysis. Q. J. R. Meteorol. Soc. 131, 2961–3012. http://dx.doi.org/10.1256/qj.04.176

Vallon, M., 1989. Evolution, Water Balance, Potential Hazards, and Control of a Pro-Glacial Lake in the French Alps. Annals of Glaciology 13, 273–278. https://doi.org/10.3189/S0260305500008041

Vallon, M., 1992. Note sur la surveillance du site d'Arsine, à l'attention du Service de Restauration des Terrains de Montagne des Hautes Alpes et des mairies des communes concernées. 5 pp.

Vallon, M., Vincent, C., 2000. Glacier et lacs d'Arsine, rapport intermédiaire n°2 à la commune de Monêtier les Bains. 17 pp.

van der Beek, P., Bourbon, P., 2008. A quantification of the glacial imprint on relief development in the French western Alps. Geomorphology 97, 1-2, 52–72. https://doi.org/10.1016/j.geomorph.2007.02.038

van Dijk, E.J.C., Jungclaus, J., Sigl, M., Timmreck, C., Krüger, K., 2024. High-frequency climate forcing causes prolonged cold periods in the Holocene. Commun. Earth Environ. 5, 242. https://doi.org/10.1038/s43247-024-01380-0

Vargo, L.J., Anderson, B.M., Dadić, R. Horgan H.J., Mackintosh A.N., King A.D., Lorrey A.M., 2020. Anthropogenic warming forces extreme annual glacier mass loss. Nat. Clim. Chang. 10, 856–861. https://doi.org/10.1038/s41558-020-0849-2

Vernay, M., Lafaysse, M., Monteiro, D., Hagenmuller, P., Nheili, R., Samacoïts, R., Verfaillie, D., Morin, S., 2022. The S2M meteorological and snow cover reanalysis over the French mountainous areas: description and evaluation (1958–2021). Earth Syst. Sci. Data 14, 1707–1733. https://doi.org/10.5194/essd-14-1707-2022

Vlug, A., Marzeion, B., Prange, M., van der Laan, L., Maussion, F., 2023. The influence of climate forcings on global glacier evolution over the last millennium, EGU General Assembly 2023, Vienna, Austria, 24–28 Apr 2023, EGU23-9580. https://doi.org/10.5194/egusphere-egu23-9580

Violot, V. 2014. Impact de la déglaciation Tardiglaciaire et Holocène sur la genèse des écroulements postglaciaires de la vallée de la Haute Romanche. MSc thesis, University of Clermont Ferrand, 57 pp.

Vivian, R., 1979. Les glaciers sont vivants. Paris, Denoël, 238 pp.

Walsh, K., Court-Picon, M., de Beaulieu, J.-L., Guiter, F., Mocci, F., Richer, S., Sinet, R., Talon, B., Tzortzis, S., 2014. A historical ecology of the Ecrins (Southern French Alps): Archaeology and palaeoecology of the Mesolithic to the Medieval period. Quaternary International 353, 52–73. https://doi.org/10.1016/j.quaint.2013.08.060

Wahrhaftig, C., Cox, A., 1959. Rock glaciers in the Alaska Range. Geological Society of America Bulletin 70, 4, 383–436. https://doi.org/10.1130/0016-7606(1959)70[383:rgitar]2.0.co;2

Winkler, S., 2018. Investigating Holocene mountain glaciations: a plea for the supremacy of glacial geomorphology when reconstructing glacier chronologies. Erdkunde 72, 3, 215–234. https://doi.org/10.3112/erdkunde.2018.03.04

Wipf, A., 2001. Gletschergeschichtliche Untersuchungen im spät- und postglazialen Bereich des Hinteren Lauterbrunnentals (Berner Oberland, Schweiz). Geogr. Helv. 56, 133–144. https://doi.org/10.5194/gh-56-133-2001

Wirsig, C., Ivy-Ochs, S., Akçar, N., Lupker, M., Hippe, K., Wacker, L., Vockenhuber, C., Schlüchter C., 2016. Combined cosmogenic ^{10}Be, in situ ^{14}C and ^{36}Cl concentrations constrain Holocene history and erosion depth of Grueben glacier (CH). Swiss J. Geosci. 109, 379–388. https://doi.org/10.1007/s00015-016-0227-2

Young, N.E., Briner, J.P., Miller, G.H., Lesnek, A.J., Crump, S.E., Thomas, E.K., Pendleton S.L., Cuzzone J., Lamp J., Zimmerman S., Caffee M., Schaefer, J.M., 2020. Deglaciation of the Greenland and Laurentide ice sheets interrupted by glacier advance during abrupt coolings. Quaternary Science Reviews 229, 106091. https://doi.org/10.1016/j.quascirev.2019.106091

Zander, P.D., Żarczyński, M., Tylmann, W., Vogel, H., Grosjean, M., 2024. Subdecadal Holocene warm-season temperature variability in central Europe recorded by biochemical varves. Geophysical Research Letters 51, e2024GL110871. https://doi.org/10.1029/2024GL110871

Zekollari, H., Huss, M., Farinotti, D., 2020. On the Imbalance and Response Time of Glaciers in the European Alps. Geophysical Research Letters 47, e2019GL085578. https://doi.org/10.1029/2019GL085578

Zoller, H., Schindler, C. M. & Röthlisberger, H., 1966. Postglaziale Gletscherstände und Klimaschwankungen im Gotthardmassiv und Vorderrheingebiet. Verhandlungen der Naturforschenden Gesellschaft in Basel 77, 97–164.

Zumbühl, H.J., Holzhauser, H., 1988. Alpengletscher in der Kleinen Eiszeit. In: Die Alpen. Sonderheft zum 125 jährigen Jubiläum des SAC, 64. Jg., 3. Quartal, Bern.

Highlights

- Most detailed TCN-based Holocene-long glacier chronology for the western European Alps
- Main glacier advances occurred at 11.9, 11.1, 10.3, 3.7, 2.7, 1.7, 0.65 and 0.17 ka
- Dating of a c. 8.4×10^6 m^3 rock avalanche onto eastern part of the glacier 10.7 ka ago
- RA responsible for prominent moraine deposition outboard the LIA extent up to 9.5 ka
- We review evidence for Holocene glacier activity in the Alps

Figure

Click here to access/download;Figure;FIG 1_revised.jpg

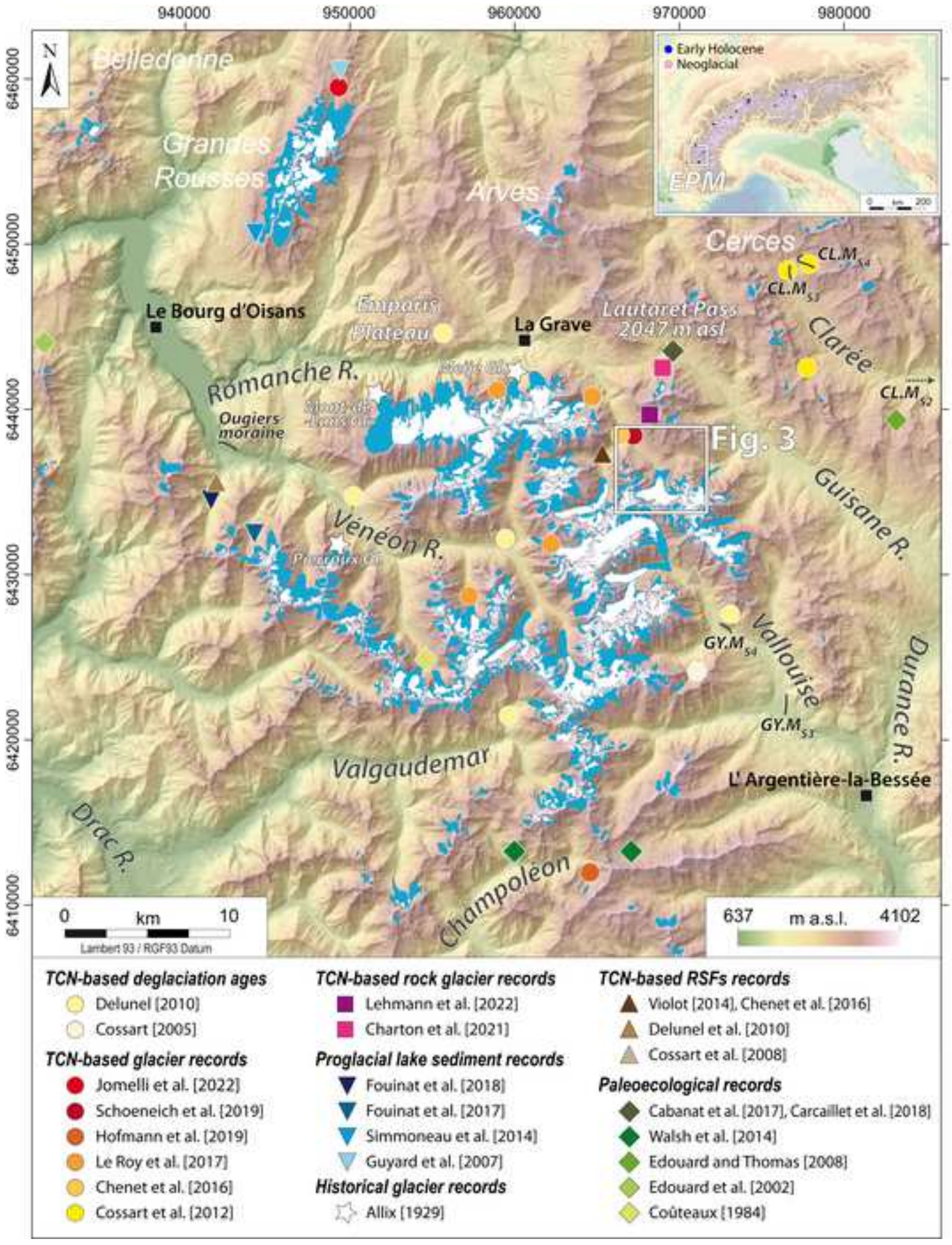

Figure

Click here to access/download;Figure;FIG 2_revised.jpg

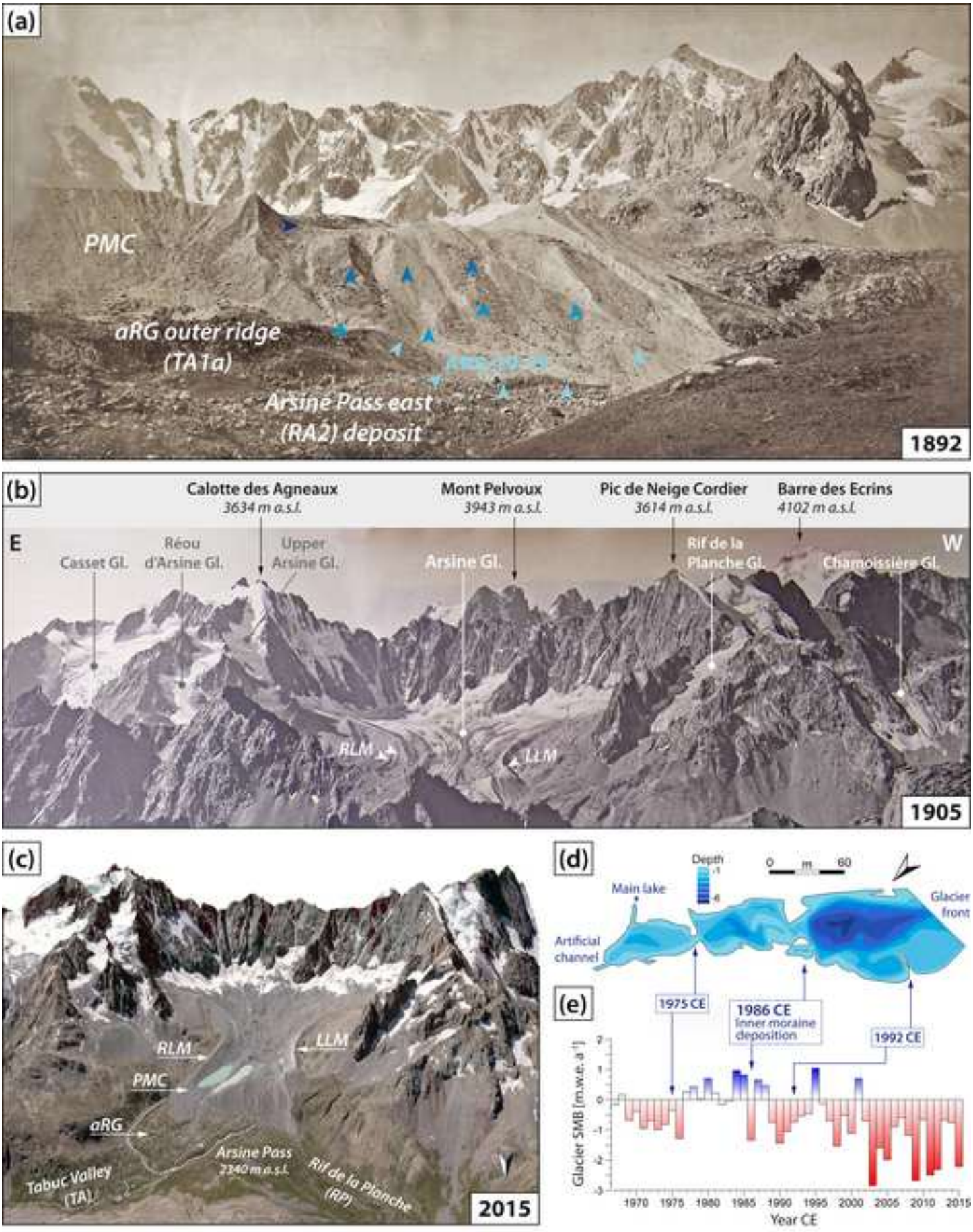

Figure

Click here to access/download;Figure;FIG 3_revised.jpg

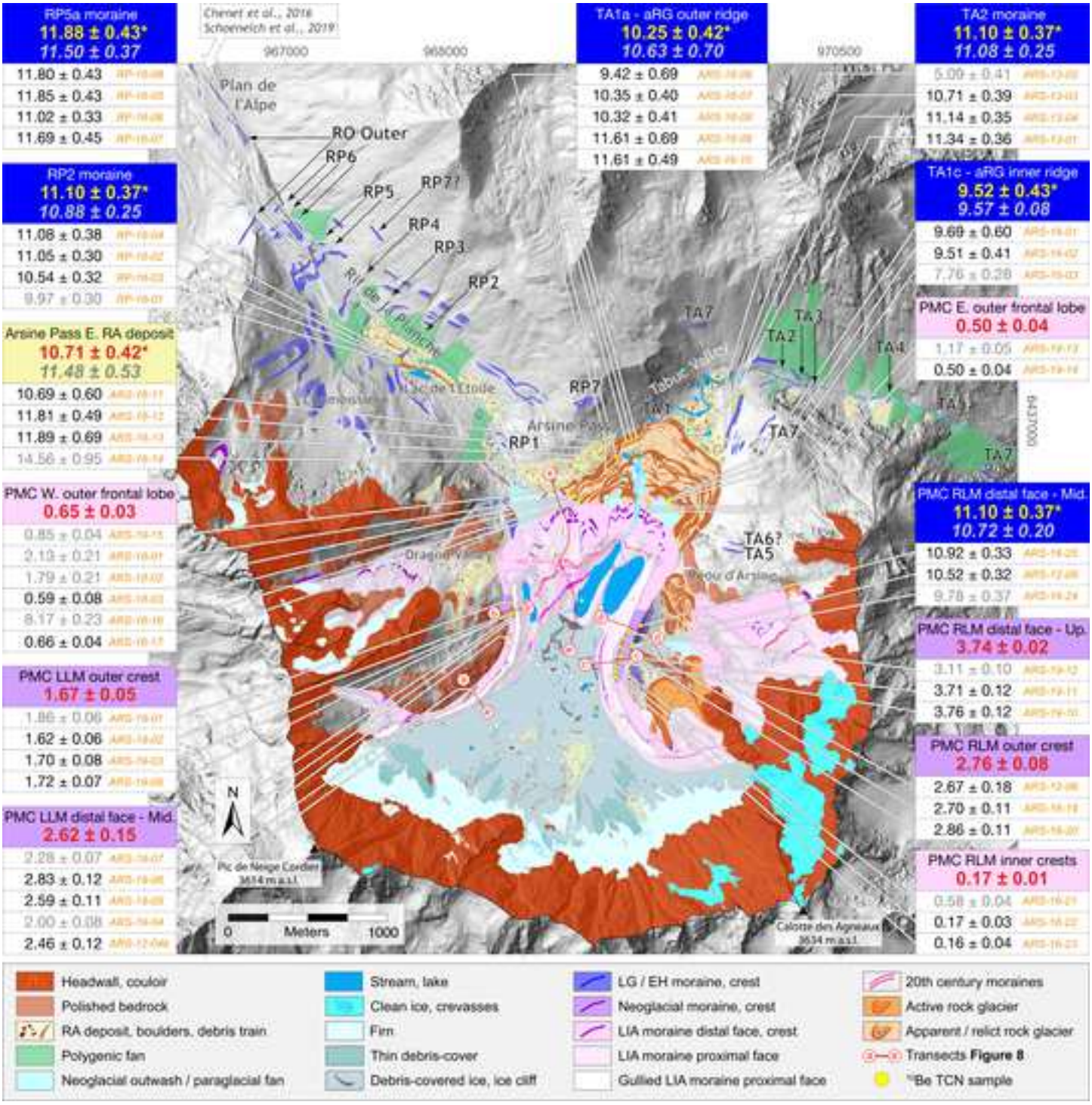

Figure

Click here to access/download;Figure;FIG 4_revised.jpg

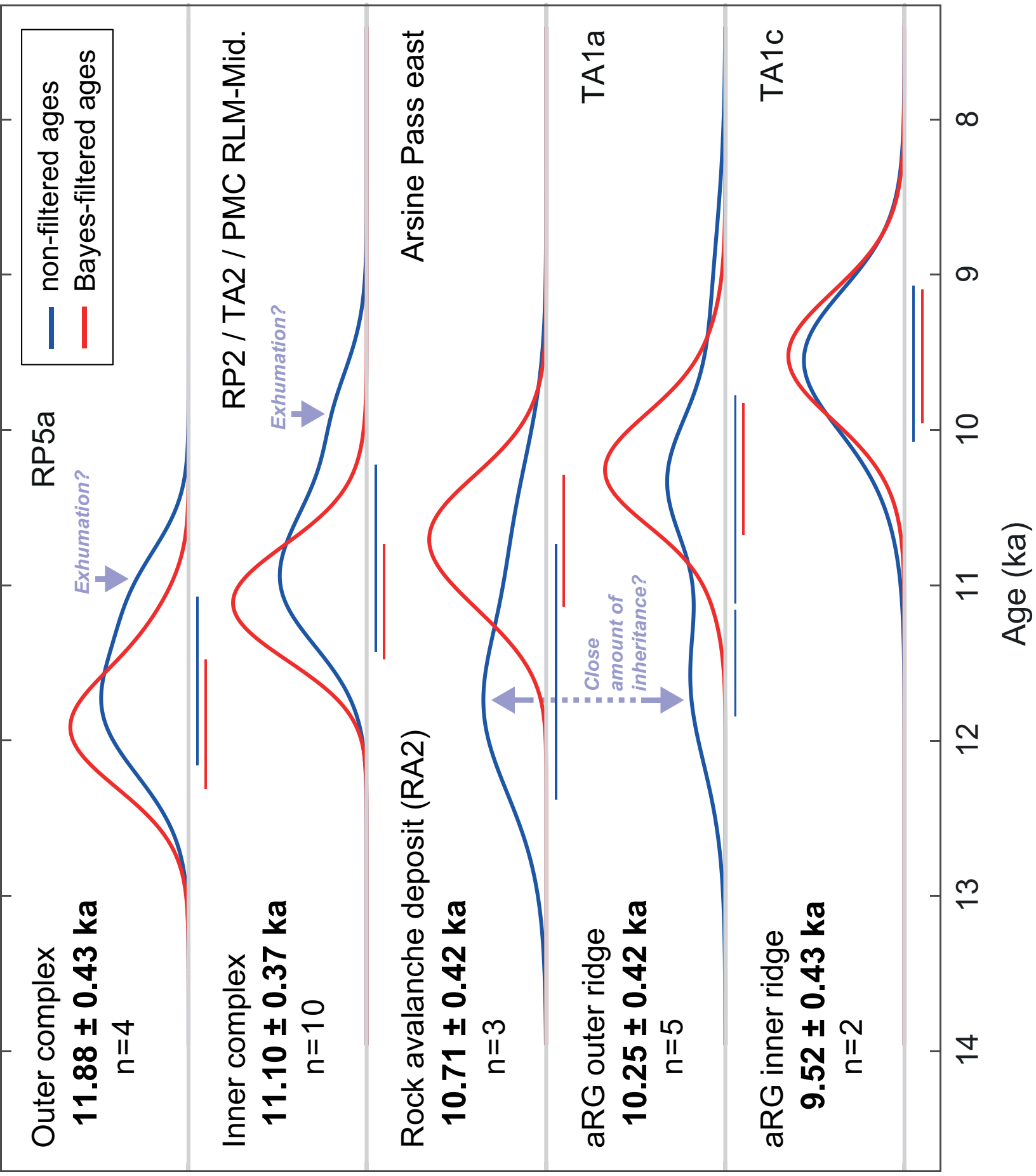

Figure

Click here to access/download;Figure;FIG 6_revised.jpg

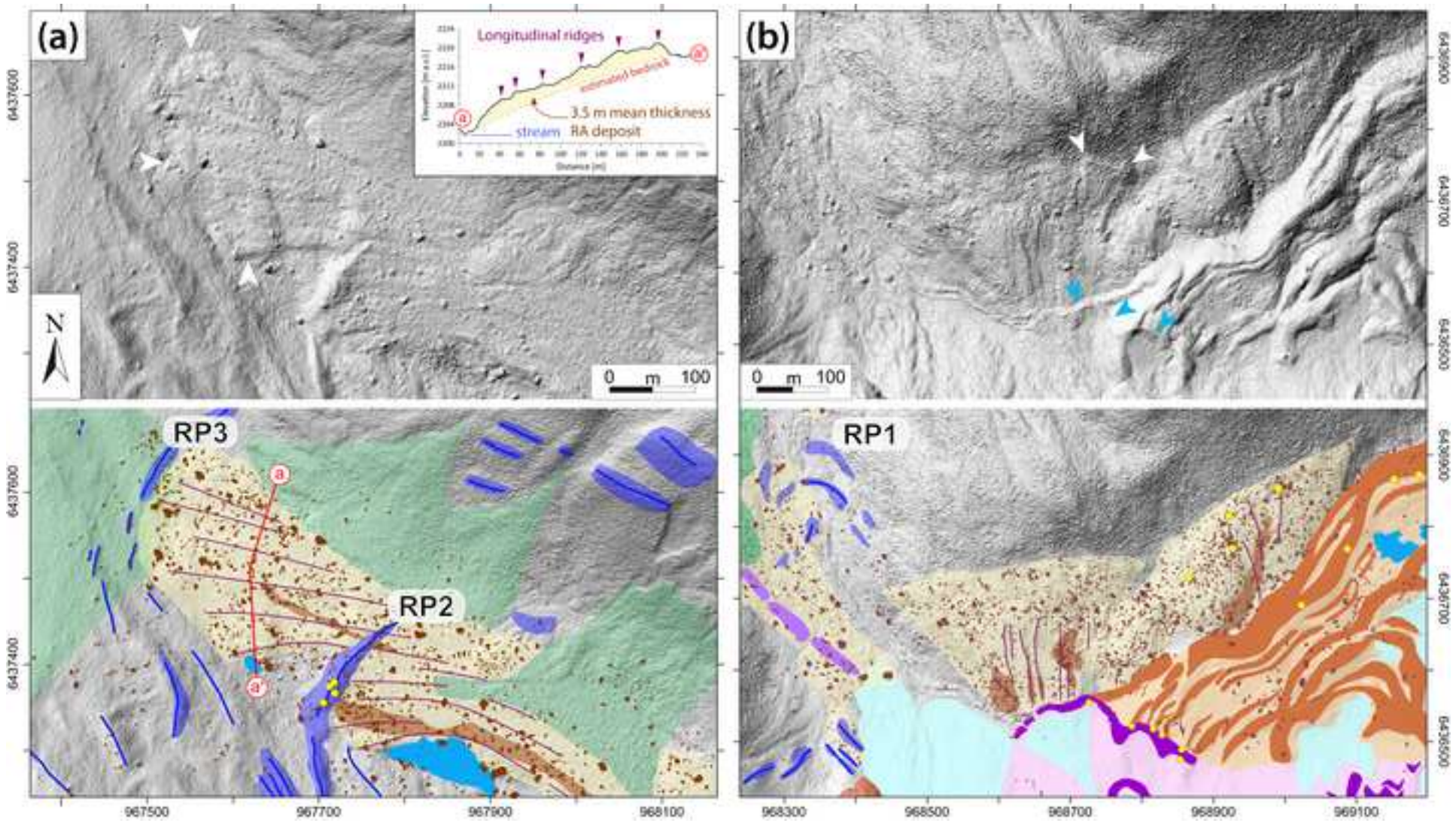

Figure

Click here to access/download;Figure;FIG 7_revised.jpg

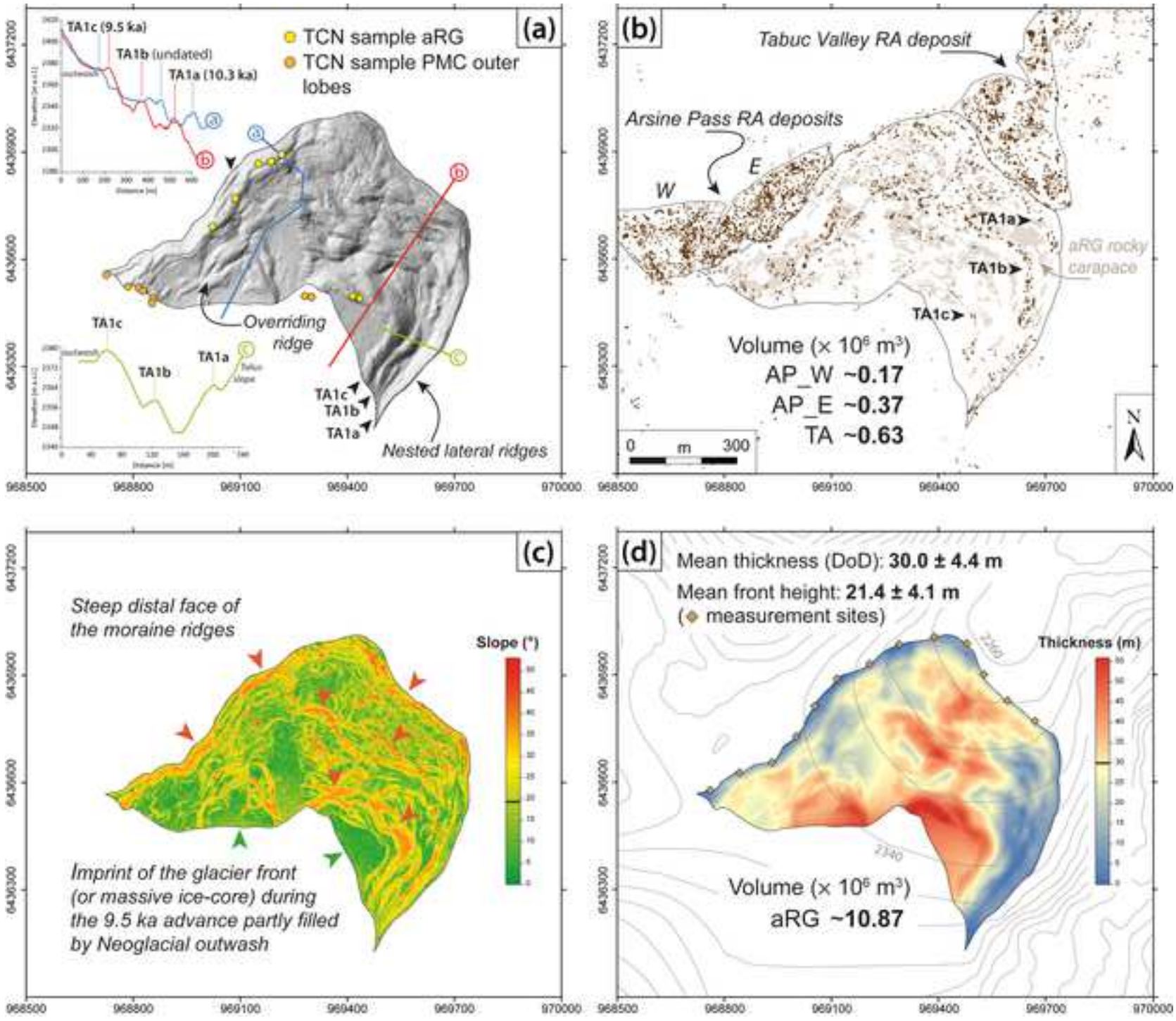

Figure

Click here to access/download;Figure;FIG 8_revised.jpg

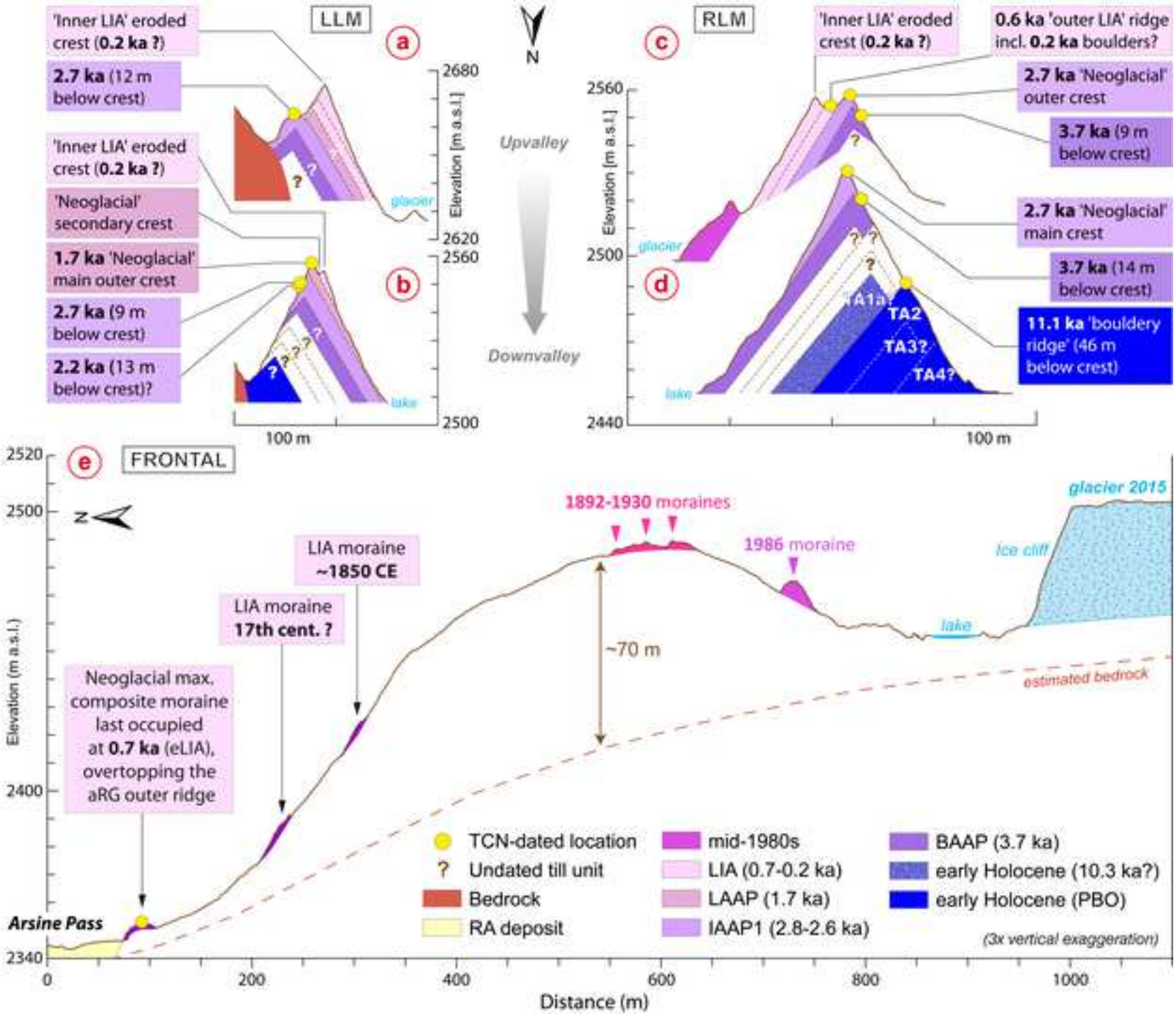

Figure

Click here to access/download;Figure;FIG 9_revised.jpg

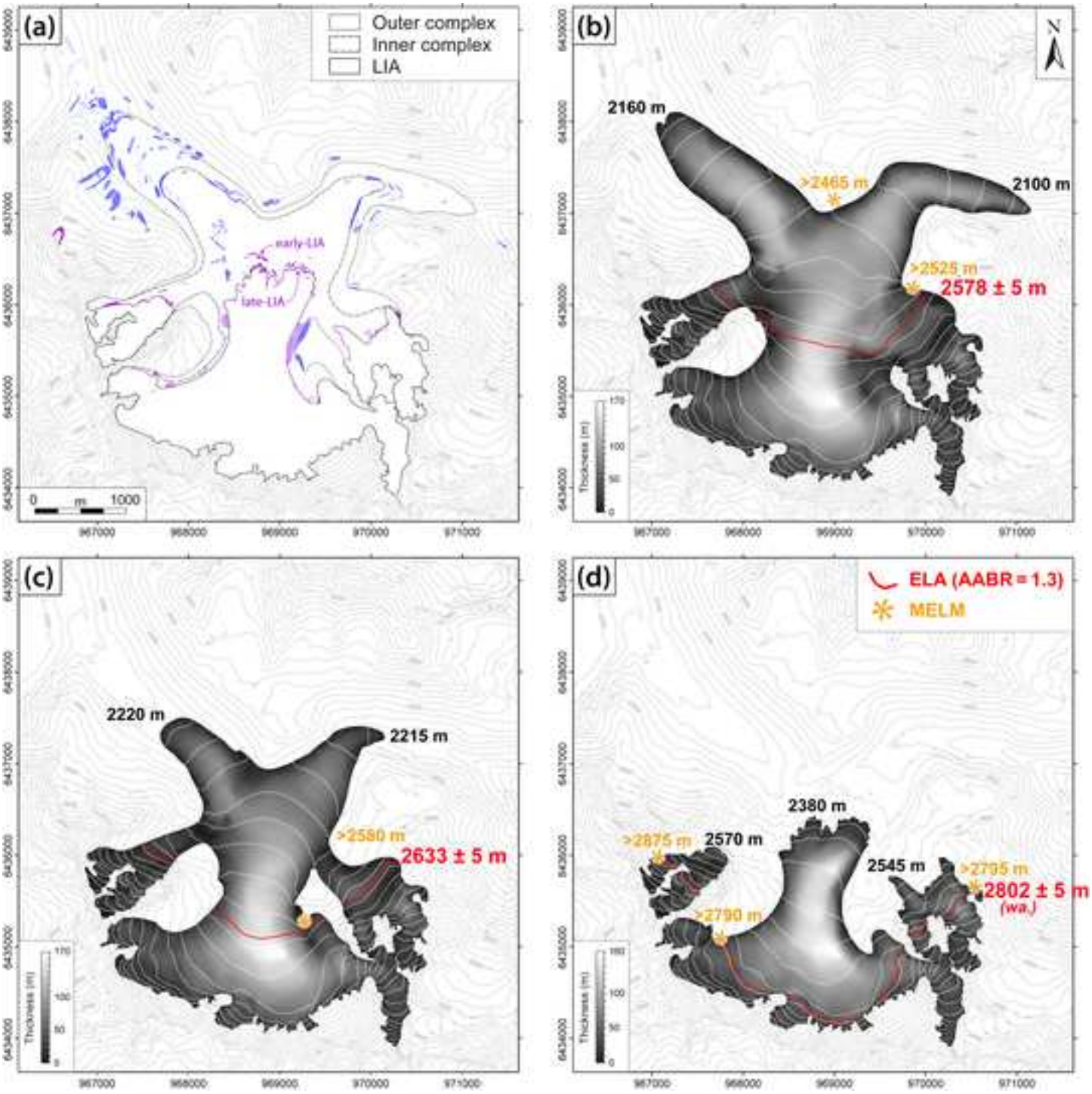

Figure

Click here to access/download;Figure;FIG 10_revised.eps

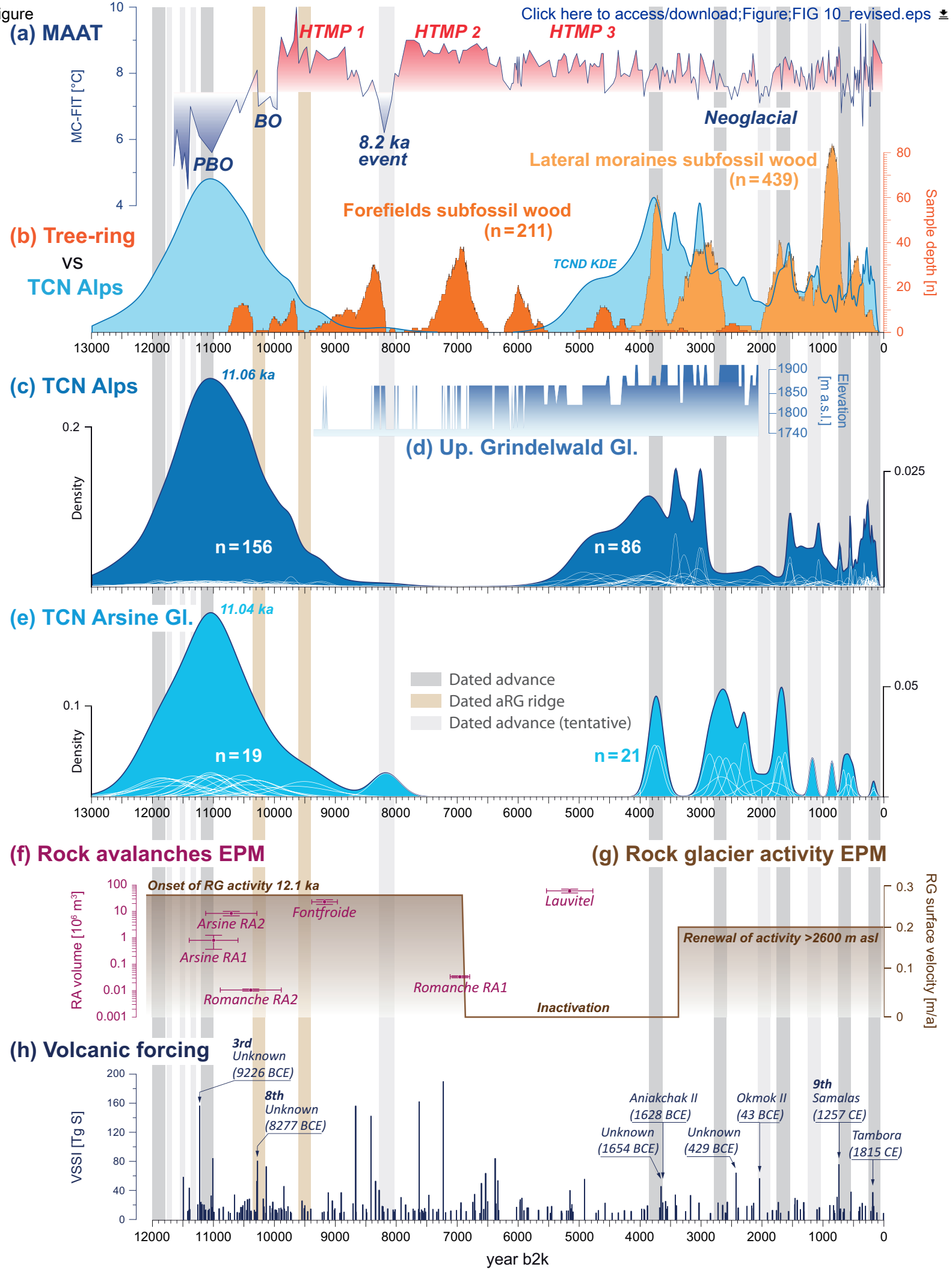

Figure

Click here to access/download;Figure;FIG 11_revised.jpg

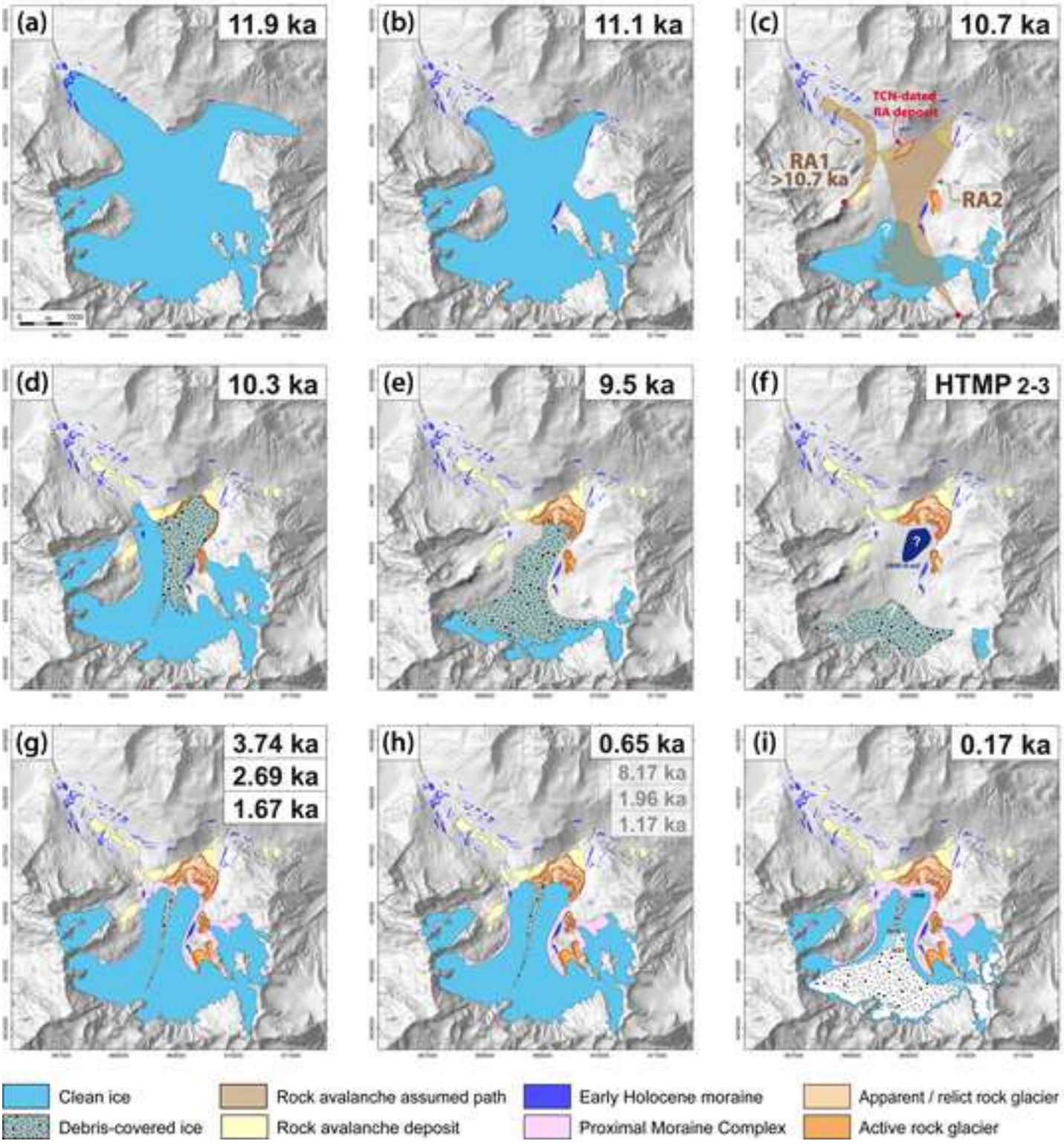

Figure

Click here to access/download;Figure;FIG. 12_revised.eps

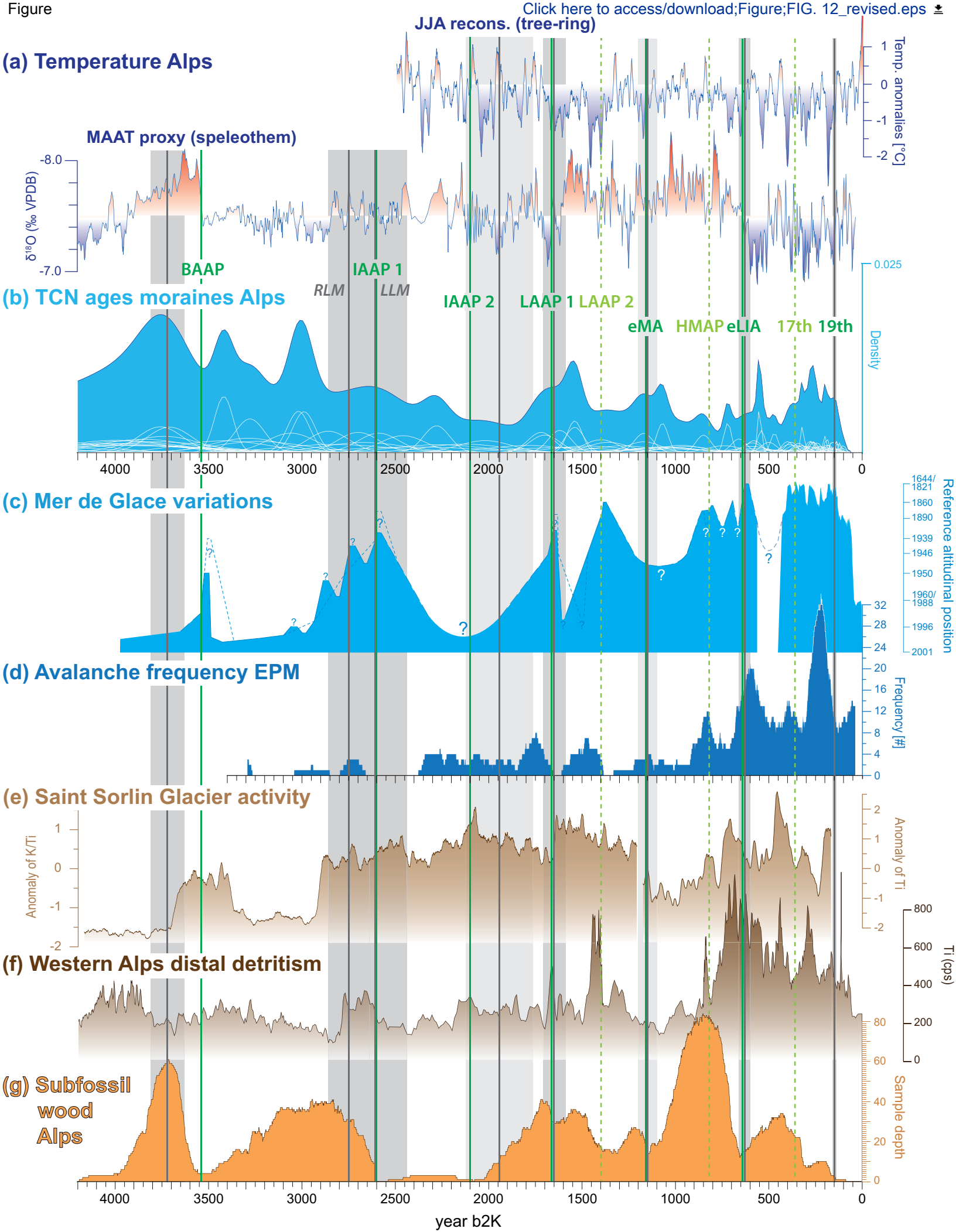

Table 1. Results of the ^{10}Be measurements at Arsine Glacier.

Sample	Mass of dissolved quartz [g]	Mass of ^{9}Be in carrier [mg]	^{10}Be/^{9}Be [× 10^{-14}]	^{10}Be concentration [atoms g^{-1} quartz]
RP5a moraine				
RP-16-05	10.7470	0.30440	13.914 ± 0.489	252563 ± 9387 [b]
RP-16-06	15.0120	0.30520	17.891 ± 0.565	235336 ± 7763 [b]
RP-16-07	16.5750	0.30560	20.745 ± 0.807	248592 ± 9996 [b]
RP-16-08	15.7720	0.30480	19.872 ± 0.708	249264 ± 9201 [b]
RP2 moraine				
RP-16-01	28.6500	0.43863	21.433 ± 0.675	216212 ± 6918 [d]
RP-16-02	28.2200	0.44386	23.175 ± 0.698	240472 ± 7352 [d]
RP-16-03	28.4600	0.44964	21.923 ± 0.697	228723 ± 7367 [e]
RP-16-04	20.0800	0.45278	16.489 ± 0.603	244583 ± 9100 [e]
TA2 moraine				
ARS-13-01	11.0300	0.45650	9.539 ± 0.322	257802 ± 8985 [c]
ARS-13-02	7.7200	0.44619	3.298 ± 0.257	116045 ± 10050 [d]
ARS-13-03	22.2300	0.44498	18.699 ± 0.724	246178 ± 9704 [d]
ARS-13-04	17.6300	0.46407	14.860 ± 0.500	257616 ± 8837 [c]
Arsine Pass eastern rock avalanche deposit				
ARS-16-11	22.8443	0.44262	20.129 ± 1.193	257683 ± 15453 [g]
ARS-16-12	22.4856	0.45490	21.540 ± 0.904	288223 ± 12232 [g]
ARS-16-13	22.0673	0.45324	21.177 ± 1.248	288077 ± 17127 [f]
ARS-16-14	20.5858	0.45535	24.394 ± 1.675	357320 ± 24759 [g]
PMC right lateral moraine distal face – Middle slope				
ARS-12-08	34.9571	0.29740	48.019 ± 1.565	271538 ± 8919 [a]
ARS-16-24	16.1700	0.46576	13.252 ± 0.503	250971 ± 9723 [c]
ARS-16-25	13.2400	0.46400	12.167 ± 0.394	279932 ± 9294 [c]
TA1a – aRG outer ridge				
ARS-16-06	2.8265	0.46252	2.304 ± 0.151	231888 ± 16830 [f]
ARS-16-07	14.3735	0.45115	12.285 ± 0.492	253008 ± 10345 [g]
ARS-16-08	21.5815	0.46059	17.353 ± 0.721	244849 ± 10295 [f]
ARS-16-09	23.3734	0.45408	21.597 ± 1.331	277510 ± 17279 [g]
ARS-16-10	20.6656	0.45874	18.778 ± 0.826	275804 ± 12262 [f]
TA1c – aRG inner ridge				
ARS-16-01	21.9057	0.45212	17.324 ± 1.075	235876 ± 14832 [g]
ARS-16-02	23.3568	0.44180	18.740 ± 0.791	234007 ± 10010 [g]
ARS-16-03	23.4555	0.45045	15.100 ± 0.544	191357 ± 6989 [f]
PMC right lateral moraine distal face – Upper slope				
ARS-19-10	39.4074	0.44930	12.903 ± 0.428	96197 ± 3271 [i]
ARS-19-11	22.6519	0.44032	7.629 ± 0.255	96684 ± 3327 [h]
ARS-19-12	39.5947	0.45142	9.355 ± 0.296	69171 ± 2271 [i]
PMC right lateral moraine outer crest				
ARS-12-06	40.2210	0.29840	14.171 ± 0.895	68993 ± 4468 [a]
ARS-16-19	26.5400	0.46419	6.231 ± 0.226	70325 ± 2695 [c]
ARS-16-20	27.7200	0.46416	6.878 ± 0.245	74567 ± 2788 [c]
PMC left lateral moraine distal face – Middle slope				
ARS-12-04b	20.2220	0.45411	4.717 ± 0.215	66674 ± 3261 [i]
ARS-19-04	19.8839	0.45136	3.658 ± 0.131	52746 ± 2033 [h]

ARS-19-05	14.0737	0.43112	3.359 ± 0.125	64878 ± 2617 [h]
ARS-19-06	21.2019	0.45617	5.234 ± 0.208	73096 ± 3013 [j]
ARS-19-07	39.8588	0.45339	7.810 ± 0.242	57996 ± 1854 [h]
PMC left lateral moraine outer crest				
ARS-19-01	34.8320	0.45103	6.033 ± 0.207	49813 ± 1813 [i]
ARS-19-02	45.2433	0.44846	6.720 ± 0.223	42675 ± 1494 [i]
ARS-19-03	21.9402	0.43273	3.735 ± 0.161	45434 ± 2172 [i]
ARS-19-08	40.7496	0.43669	6.532 ± 0.242	44739 ± 1746 [i]
PMC western outer frontal lobe				
ARS-16-16	47.9400	0.44991	32.091 ± 0.918	199629 ± 5762 [e]
ARS-16-17	50.6600	0.45200	2.918 ± 0.154	15867 ± 950 [e]
ARS-18-01	24.6488	0.45024	4.317 ± 0.403	49982 ± 4925 [g]
ARS-18-02	18.4146	0.45442	2.795 ± 0.297	42463 ± 4915 [g]
ARS-18-03	12.7830	0.45200	0.795 ± 0.074	14356 ± 1862 [f]
ARS-19-15	48.0370	0.45106	3.412 ± 0.140	19677 ± 904 [i]
PMC eastern outer frontal lobe				
ARS-19-13	49.7830	0.44840	4.931 ± 0.179	28008 ± 1096 [i]
ARS-19-14	20.9248	0.45378	1.014 ± 0.061	12083 ± 967 [h]
PMC right lateral moraine inner crest				
ARS-16-21	40.9300	0.44855	2.443 ± 0.140	15996 ± 1066 [e]
ARS-16-22	47.3900	0.45018	1.026 ± 0.089	4875 ± 616 [e]
ARS-16-23	19.7400	0.46077	0.501 ± 0.046	4463 ± 1017 [c]

Procedural blanks				
Name	**Processed with**	**Mass of ^{9}Be in carrier [mg]**	**^{10}Be/^{9}Be [× 10^{-15}]**	**Total number of atoms ^{10}Be**
BKGRE74_2013Apr11	(a)	0.30250	2.51 ± 1.06	50667 ± 21508
BKGRE102_2018Jan23	(b)	0.30250	5.73 ± 0.83	115861 ± 16784
B1_2018May28	(c)	0.46276	2.14 ± 0.46	66154 ± 14114
B2_2018May28	(d)	0.45088	2.91 ± 0.40	87519 ± 12111
B3_2018May28	(e)	0.45151	2.57 ± 0.40	77553 ± 12003
BKM1_2019Mar15	(f)	0.46343	1.83 ± 0.27	56634 ± 8470
BKM2_2019Mar15	(g)	0.45454	2.20 ± 0.28	66764 ± 8542
BL1_2020Nov24	(h)	0.45063	1.81 ± 0.27	54585 ± 7977
BL2_2020Nov24	(i)	0.45239	2.75 ± 0.32	83068 ± 9699
BL_2021Jun01	(j)	0.45889	1.49 ± 0.29	45707 ± 8744

Table 2. ^{10}Be TCN boulder exposure age results and mean surface ages computed at Arsine Glacier, according to three different scaling schemes. Individual and mean ages are reported with the internal (analytical) uncertainties and the external uncertainties (including production rate uncertainties) between brackets. No snow- nor erosion- correction have been applied (see main text). Pruned outliers are in italic (see Section 3.6.3). The weighted mean ages shown here (together with weighted mean internal and external uncertainties) are not necessarily the landform ages used in the discussion (see Section 3.6.4). For calculation we assumed a rock density of 2.65 g cm^{-3}. Exposure ages are expressed in ka before the sampling year (indicated in sample label).

Sample	(1) ^{10}Be exposure age (ka) CREp + 'Lm-ERA-LiftVDM' + Alps calibration	(2) ^{10}Be exposure age (ka) CRONUS v3 + 'Lm-ERA-LiftVDM' + Alps calibration	*% diff.*	(3) ^{10}Be exposure age (ka) CREp + 'LSDn-ERA-LiftVDM' + Alps calibration	*% diff.*
RP5a moraine					
RP-16-05	11.85 ± 0.43 (0.52)	12.10 ± 0.45 (1.22)	*2.0*	11.19 ± 0.39 (0.46)	*-5.6*
RP-16-06	11.02 ± 0.33 (0.42)	11.28 ± 0.37 (1.12)	*2.2*	10.38 ± 0.33 (0.40)	*-5.9*
RP-16-07	11.69 ± 0.45 (0.53)	11.95 ± 0.48 (1.22)	*2.2*	11.05 ± 0.41 (0.48)	*-5.5*
RP-16-08	11.80 ± 0.43 (0.51)	12.04 ± 0.45 (1.22)	*2.0*	11.13 ± 0.38 (0.46)	*-5.7*
Reduced chi-sq.	**1.15**	**0.93**		**1.18**	
Wtd. mean	**11.50 ± 0.37 (0.46)**	**11.78 ± 0.36 (1.16)**	*2.4*	**10.89 ± 0.35 (0.43)**	*-5.3*
Bayesian age	**11.88 ± 0.43**	**12.14 ± 0.44**	*2.2*	**11.19 ± 0.39**	*-5.8*
RP2 moraine					
RP-16-01	*9.97 ± 0.30 (0.38)*	*10.22 ± 0.33 (1.01)*	*2.5*	*9.33 ± 0.30 (0.39)*	*-6.4*
RP-16-02	11.05 ± 0.30 (0.39)	11.30 ± 0.35 (1.12)	*2.2*	10.37 ± 0.30 (0.39)	*-6.2*
RP-16-03	10.54 ± 0.32 (0.40)	10.78 ± 0.35 (1.12)	*2.3*	9.90 ± 0.31 (0.38)	*-6.1*
RP-16-04	11.08 ± 0.38 (0.44)	11.35 ± 0.42 (1.15)	*2.5*	10.43 ± 0.37 (0.44)	*-5.9*
Reduced chi-sq.	**0.86**	**0.76**		**0.82**	
Wtd. mean	**10.88 ± 0.25 (0.35)**	**11.12 ± 0.26 (1.08)**	*2.2*	**10.21 ± 0.24 (0.33)**	*-6.2*
Bayesian age	**11.10 ± 0.37**	**11.37 ± 0.40**	*2.4*	**10.41 ± 0.38**	*-6.2*
TA2 moraine					
ARS-13-01	11.34 ± 0.36 (0.44)	11.60 ± 0.41 (1.16)	*2.3*	10.65 ± 0.36 (0.44)	*-6.1*
ARS-13-02	*5.09 ± 0.41 (0.43)*	*4.99 ± 0.43 (0.64)*	*-2.0*	*4.79 ± 0.40 (0.41)*	*-6.3*
ARS-13-03	10.71 ± 0.39 (0.46)	10.95 ± 0.43 (1.12)	*2.4*	10.04 ± 0.37 (0.44)	*-6.1*
ARS-13-04	11.14 ± 0.35 (0.43)	11.40 ± 0.39 (1.14)	*2.4*	10.44 ± 0.34 (0.42)	*-6.3*
Reduced chi-sq.	**0.75**	**0.63**		**0.72**	
Wtd. mean	**11.08 ± 0.25 (0.36)**	**11.33 ± 0.27 (1.10)**	*2.3*	**10.38 ± 0.25 (0.35)**	*-6.3*
Bayesian age	**11.10 ± 0.37**	**11.37 ± 0.40**	*2.4*	**10.41 ± 0.38**	*-6.2*
Arsine Pass eastern rock avalanche deposit					
ARS-16-11	10.69 ± 0.60 (0.64)	10.92 ± 0.66 (1.22)	*2.2*	9.98 ± 0.58 (0.63)	*-6.6*
ARS-16-12	11.81 ± 0.49 (0.56)	12.06 ± 0.51 (1.24)	*2.1*	11.06 ± 0.44 (0.50)	*-6.4*
ARS-16-13	11.89 ± 0.69 (0.75)	12.12 ± 0.72 (1.35)	*1.9*	11.11 ± 0.62 (0.67)	*-6.6*
ARS-16-14	*14.56 ± 0.95 (1.01)*	*14.73 ± 1.02 (1.72)*	*1.2*	*13.62 ± 0.90 (0.95)*	*-6.5*
Reduced chi-sq.	**1.27**	**1.11**		**1.29**	
Wtd. mean	**11.48 ± 0.53 (0.59)**	**11.75 ± 0.52 (1.22)**	*2.4*	**10.77 ± 0.49 (0.55)**	*-6.2*
Bayesian age	**10.71 ± 0.42**	**10.98 ± 0.45**	*2.3*	**10.03 ± 0.44**	*-6.5*
PMC right lateral moraine distal face – Middle slope					
ARS-12-08	10.52 ± 0.32 (0.40)	10.77 ± 0.36 (1.07)	*2.4*	9.73 ± 0.32 (0.39)	*-7.5*
ARS-16-24	*9.78 ± 0.37 (0.43)*	*10.03 ± 0.39 (1.02)*	*2.6*	*8.97 ± 0.37 (0.44)*	*-8.3*
ARS-16-25	10.92 ± 0.33 (0.41)	11.17 ± 0.37 (1.11)	*2.3*	10.13 ± 0.31 (0.40)	*-7.2*
Reduced chi-sq.	**0.73**	**0.61**		**0.81**	
Wtd. mean	**10.72 ± 0.20 (0.31)**	**10.96 ± 0.20 (1.05)**	*1.3*	**9.94 ± 0.20 (0.31)**	*-8.1*

Bayesian age	**11.10 ± 0.37**	**11.37 ± 0.40**	*2.4*	**10.41 ± 0.38**	*-6.2*
TA1a – aRG outer ridge					
ARS-16-06	9.42 ± 0.69 (0.73)	9.71 ± 0.71 (1.15)	*3.1*	8.69 ± 0.65 (0.69)	*-7.7*
ARS-16-07	10.35 ± 0.40 (0.46)	10.61 ± 0.44 (1.09)	*2.5*	9.65 ± 0.40 (0.45)	*-6.8*
ARS-16-08	10.32 ± 0.41 (0.47)	10.58 ± 0.45 (1.09)	*2.5*	9.63 ± 0.41 (0.47)	*-6.7*
ARS-16-09	11.61 ± 0.69 (0.74)	11.87 ± 0.74 (1.34)	*2.2*	10.87 ± 0.64 (0.68)	*-6.4*
ARS-16-10	11.61 ± 0.49 (0.56)	11.87 ± 0.53 (1.24)	*2.3*	10.89 ± 0.45 (0.52)	*-6.2*
Reduced chi-sq.	**2.54**	**2.22**		**2.84**	
Wtd. mean	**10.63 ± 0.70 (0.74)**	**10.88 ± 0.71 (1.04)**	*2.4*	**9.96 ± 0.72 (0.76)**	*-6.3*
Bayesian age	**10.25 ± 0.42**	**10.50 ± 0.44**	*2.4*	**9.54 ± 0.43**	*-6.9*
TA1c – aRG inner ridge					
ARS-16-01	9.69 ± 0.60 (0.64)	9.95 ± 0.63 (1.13)	*2.7*	8.96 ± 0.59 (0.63)	*-7.5*
ARS-16-02	9.51 ± 0.41 (0.47)	9.79 ± 0.42 (1.01)	*3.0*	8.79 ± 0.40 (0.46)	*-7.6*
ARS-16-03	*7.76 ± 0.28 (0.33)*	*7.93 ± 0.29 (0.80)*	*2.2*	*7.25 ± 0.23 (0.28)*	*-6.6*
Reduced chi-sq.	**0.06**	**0.05**		**0.06**	
Wtd. mean	**9.57 ± 0.08 (0.24)**	**9.84 ± 0.07 (0.93)**	*2.8*	**8.85 ± 0.08 (0.24)**	*-7.5*
Bayesian age	**9.52 ± 0.43**	**9.79 ± 0.44**	*2.8*	**8.81 ± 0.42**	*-7.5*
PMC right lateral moraine distal face – Upper slope					
ARS-19-10	3.76 ± 0.12 (0.15)	3.58 ± 0.12 (0.36)	*-4.7*	3.46 ± 0.12 (0.14)	*-8.0*
ARS-19-11	3.71 ± 0.12 (0.15)	3.51 ± 0.12 (0.35)	*-5.4*	3.40 ± 0.11 (0.14)	*-8.4*
ARS-19-12	*3.11 ± 0.10 (0.12)*	*2.95 ± 0.10 (0.29)*	*-5.2*	*2.86 ± 0.10 (0.12)*	*-8.0*
Reduced chi-sq.	**0.09**	**0.19**		**0.14**	
Wtd. mean	**3.74 ± 0.02 (0.09)**	**3.54 ± 0.04 (0.33)**	*-5.3*	**3.43 ± 0.03 (0.08)**	*-8.3*
PMC right lateral moraine outer crest					
ARS-12-06	2.67 ± 0.18 (0.19)	2.56 ± 0.17 (0.29)	*-4.2*	2.42 ± 0.17 (0.18)	*-9.4*
ARS-16-19	2.70 ± 0.11 (0.13)	2.59 ± 0.10 (0.26)	*-4.0*	2.46 ± 0.10 (0.12)	*-8.9*
ARS-16-20	2.86 ± 0.11 (0.13)	2.73 ± 0.10 (0.28)	*-4.7*	2.61 ± 0.10 (0.12)	*-8.7*
Reduced chi-sq.	**0.69**	**0.60**		**0.76**	
Wtd. mean	**2.76 ± 0.08 (0.11)**	**2.64 ± 0.07 (0.26)**	*-4.6*	**2.52 ± 0.08 (0.10)**	*-9.0*
PMC left lateral moraine distal face – Middle slope					
ARS-12-04b	2.46 ± 0.12 (0.14)	2.37 ± 0.12 (0.25)	*-3.7*	2.20 ± 0.12 (0.13)	*-10.6*
ARS-19-04	*2.00 ± 0.08 (0.09)*	*1.94 ± 0.08 (0.20)*	*-3.1*	*1.79 ± 0.07 (0.08)*	*-10.5*
ARS-19-05	2.59 ± 0.11 (0.13)	2.48 ± 0.10 (0.25)	*-4.1*	2.34 ± 0.11 (0.12)	*-9.7*
ARS-19-06	2.83 ± 0.12 (0.14)	2.70 ± 0.11 (0.28)	*-4.5*	2.58 ± 0.12 (0.13)	*-8.8*
ARS-19-07	*2.28 ± 0.07 (0.09)*	*2.21 ± 0.07 (0.22)*	*-3.1*	*2.05 ± 0.07 (0.09)*	*-10.1*
Reduced chi-sq.	**2.46**	**2.26**		**2.57**	
Wtd. mean	**2.62 ± 0.15 (0.17)**	**2.52 ± 0.13 (0.27)**	*-3.8*	**2.37 ± 0.15 (0.16)**	*-9.5*
PMC left lateral moraine outer crest					
ARS-19-01	*1.86 ± 0.06 (0.09)*	*1.79 ± 0.07 (0.18)*	*-3.5*	*1.67 ± 0.07 (0.08)*	*-10.2*
ARS-19-02	1.62 ± 0.06 (0.07)	1.55 ± 0.05 (0.16)	*-4.1*	1.44 ± 0.06 (0.07)	*-11.1*
ARS-19-03	1.70 ± 0.08 (0.09)	1.62 ± 0.08 (0.17)	*-4.5*	1.51 ± 0.08 (0.09)	*-11.2*
ARS-19-08	1.72 ± 0.07 (0.08)	1.65 ± 0.06 (0.17)	*-4.1*	1.54 ± 0.06 (0.08)	*-10.5*
Reduced chi-sq.	**0.67**	**0.72**		**0.72**	
Wtd. mean	**1.67 ± 0.05 (0.06)**	**1.60 ± 0.04 (0.18)**	*-4.2*	**1.49 ± 0.04 (0.06)**	*-10.8*
PMC western outer frontal lobe					
ARS-16-16	*8.17 ± 0.23 (0.30)*	*8.36 ± 0.24 (0.82)*	*2.3*	*7.60 ± 0.20 (0.26)*	*-7.0*
ARS-16-17	0.66 ± 0.04 (0.05)	0.63 ± 0.04 (0.07)	*-3.9*	0.60 ± 0.04 (0.04)	*-9.1*
ARS-18-01	*2.13 ± 0.21 (0.22)*	*2.08 ± 0.21 (0.28)*	*-2.5*	*1.95 ± 0.20 (0.21)*	*-8.5*
ARS-18-02	*1.79 ± 0.21 (0.22)*	*1.74 ± 0.20 (0.26)*	*-2.8*	*1.63 ± 0.20 (0.20)*	*-8.9*

ARS-18-03	0.59 ± 0.08 (0.08)	0.57 ± 0.07 (0.09)	*-4.2*	0.54 ± 0.07 (0.07)	*-8.5*
ARS-19-15	*0.85 ± 0.04 (0.05)*	*0.84 ± 0.04 (0.09)*	*-1.8*	*0.76 ± 0.04 (0.04)*	*-10.6*
Reduced chi-sq.	**0.61**	**0.70**		**0.53**	
Wtd. mean	**0.65 ± 0.03 (0.03)**	**0.62 ± 0.03 (0.06)**	*-4.6*	**0.59 ± 0.03 (0.03)**	*-9.2*
PMC eastern outer frontal lobe					
ARS-19-13	*1.17 ± 0.05 (0.05)*	*1.16 ± 0.05 (0.12)*	*-0.8*	*1.05 ± 0.04 (0.05)*	*-10.3*
ARS-19-14	0.50 ± 0.04 (0.04)	0.47 ± 0.04 (0.06)	*-6.0*	0.46 ± 0.03 (0.04)	*-8.0*
Reduced chi-sq.	-	-		-	
Wtd. mean	**0.50 ± 0.04 (0.04)**	**0.47 ± 0.04 (0.06)**	*-6.0*	**0.46 ± 0.03 (0.04)**	*-8.0*
PMC right lateral moraine inner crest					
ARS-16-21	*0.58 ± 0.04 (0.05)*	*0.56 ± 0.04 (0.06)*	*-3.8*	*0.53 ± 0.03 (0.04)*	*-8.6*
ARS-16-22	0.17 ± 0.03 (0.03)	0.17 ± 0.02 (0.03)	*1.8*	0.17 ± 0.02 (0.02)	*0*
ARS-16-23	0.16 ± 0.04 (0.04)	0.16 ± 0.04 (0.04)	*-3.1*	0.15 ± 0.03 (0.03)	*-6.3*
Reduced chi-sq.	**0.04**	**0.19**		**0.31**	
Wtd. mean	**0.17 ± 0.01 (0.01)**	**0.17 ± 0.01 (0.02)**	*0*	**0.16 ± 0.01 (0.01)**	*-5.9*

Table 3. Characteristics of the Early Holocene rock avalanches (RAs) at Arsine Glacier.

RA event	Estimated max. elevation of source area [m a.s.l.]	Toe elevation [m a.s.l.]	H [m]	L [m]	H/L	RA deposit name	Min. area [km²]	Mean thickness [m]	Mean sediment volume [10^6 m^3]	Bedrock volume (porosity corrected) [10^6 m^3]
RA1	2820	2195	625	2345	0.27	RP	0.20	5.6	1.15 ± 0.63	0.81 ± 0.44
RA2	3405	2245	1160	3850	0.30	AP_W	0.05	3.3	0.17 ± 0.06	0.12 ± 0.04
						AP_E	0.05	8.0	0.37 ± 0.19	0.26 ± 0.14
						TA	0.10	6.8	0.63 ± 0.08	0.44 ± 0.06
						aRG	0.40	27.1	10.87 ± 2.31	7.61 ± 1.62
						Total RA2	0.60	23.4	12.04 ± 2.32	8.43 ± 1.63

Table 4. Characteristics and paleo-ELAs of the three main reconstructed stadials of Arsine Glacier. The paleo-ELAs are calculated using two different methods (AABR and AAR). The ELAs marked in italics are computed values that conflict with independent evidence (MELM method). Note that the AAR of 0.67 yields no suitable estimate for any of the stadials. The ELAs marked with asterisks are the values used to compute the 'LIA 1850 CE' weighted average. The ELAs marked in bold are the values retained for the Discussion section. The MELM values are rounded up to the nearest 5 m. The uncertainty amounts to ± 5 m for the computed ELA values and ± 10 m for the δELA values.

Glacier position		Area [km²]	Volume [km³]	Mean/Max. thickness [m]	ELA1 AABR = 1.3	ELA2 AABR = 1.6	ELA3 AAR = 0.54	ELA4 AAR = 0.67	MELM
YD maximum?		-	-	-	-	-	-	-	**2465**
δELA		-	-	-	-	-	-	-	**-335**
Outer complex		8.7	0.56	65/171	**2578**	2568	2568	*2468*	2525
δELA		-	-	-	**-224**	-234	-234	-	-
Inner complex		6.7	0.38	56/171	**2633**	2613	2643	*2533*	2580
δELA		-	-	-	**-169**	-189	-159	-	-
LIA 1850 CE	Arsine	3.4	0.21	62/162	*2737*	*2727*	*2727*	*2687*	2790*
	Réou	0.6	0.02	32/79	2818*	2808	2798	*2748*	2795
	Dragon	0.4	0.01	15/47	2882*	2862	2882	*2812*	2875
	Total	4.3	0.24	54/162	**2802***				

Supplementary Material

The Holocene history of Arsine Glacier (Western European Alps): a detailed ^{10}Be record of oscillations driven by climate and modulated by rock avalanches

Melaine Le Roy[a *], Irene Schimmelpfennig[b], Philip Deline[a], Julien Carcaillet[c], Tancrède P.M. Leger[d], Pierre Jégot[b], Philippe Schoeneich[e], Diego Cusicanqui[a, f], Felix Martin Hofmann[g], Xavier Bodin[a], ASTER Team[b, 1]

[a] Environnements, Dynamiques et Territoires de Montagne (EDYTEM), Université Savoie Mont Blanc, CNRS, Chambéry, France

[b] Centre de Recherche et d'Enseignement des Géosciences de l'Environnement (CEREGE), Aix Marseille Université, CNRS, IRD, INRA, Aix-en-Provence, France

[c] Institut des Sciences de la Terre (ISTerre), Université Grenoble Alpes, Université Savoie Mont Blanc, CNRS, IRD, IFSTTAR, Grenoble, France

[d] Institute of Earth Surface Dynamics, University of Lausanne, Lausanne, Switzerland

[e] Institut d'Urbanisme et de Géographie Alpine (IUGA), Université Grenoble Alpes, Grenoble, France

[f] Institut des Sciences de la Terre (ISTerre), Université Grenoble Alpes, CNES, CNRS, IRD, Grenoble, France

[g] Institute of Earth and Environmental Sciences, University of Freiburg, Freiburg, Germany

[1] Consortium: Georges Aumaître, Karim Keddadouche, Fawzi Zaidi

Supplementary Table 1. Characteristics of the TCN samples at Arsine Glacier. Sampling year is indicated in the sample name. Sample height represents the minimum height above ground of the sampled surface (when different from boulder height). Dip and dip direction are given for samples taken from non-flat boulder surfaces. Shielding factor includes topographic and self-shielding.

Sample	Latitude [DD]	Longitude [DD]	Elevation [m a.s.l.]	Boulder size L x W x H [cm]	Sample height [cm]	Dip/dip dir.	Thickness [cm]	Shielding factor
RP5a moraine								
RP-16-05	44.989882	6.390797	2179	210 x 095 x 070	70	-	3.00	0.977291
RP-16-06	44.989789	6.390749	2178	230 x 115 x 105	105	-	2.00	0.977291
RP-16-07	44.989779	6.390758	2177	300 x 110 x 140	140	-	3.00	0.977291
RP-16-08	44.990356	6.391149	2172	220 x 170 x 130	130	-	3.00	0.974601
RP2 moraine								
RP-16-01	44.983593	6.397364	2229	850 x 400 x 300	300	-	3.09	0.972582
RP-16-02	44.983693	6.397530	2229	300 x 230 x 150	150	-	3.26	0.972582
RP-16-03	44.983760	6.397467	2228	400 x 210 x 200	200	-	3.20	0.972582
RP-16-04	44.983807	6.397556	2229	190 x 150 x 060	60	-	1.83	0.972582
TA2 moraine								
ARS-13-01	44.981070	6.424630	2268	580 x 300 x 220	220	-	1.64	0.973700
ARS-13-02	44.978497	6.423341	2318	430 x 300 x 400	250	-	1.32	0.974200
ARS-13-03	44.980132	6.424177	2296	280 x 190 x 240	240	-	3.01	0.981100
ARS-13-04	44.980580	6.424369	2285	520 x 380 x 230	230	-	2.14	0.984100
Arsine Pass eastern rock avalanche deposit								
ARS-16-11	44.978586	6.413372	2352	1500 x 800 x 400	400	-	2.00	0.983300
ARS-16-12	44.978270	6.412463	2357	800 x 800 x 500	500	-	1.83	0.983030
ARS-16-13	44.977860	6.412506	2356	600 x 400 x 400	400	-	2.53	0.983030
ARS-16-14	44.977528	6.411715	2356	800 x 400 x 400	400	-	1.75	0.983030
PMC right lateral moraine distal face – Middle slope								
ARS-12-08	44.966991	6.415182	2495	1200 x 500 x 200	200	-	2.25	0.959767
ARS-16-24	44.966903	6.415055	2510	800 x 500 x 240	0*	22/120 SE	2.50	0.951050
ARS-16-25	44.968106	6.415942	2483	560 x 380 x 290	20	-	2.50	0.960697
TA1a – aRG outer ridge								
ARS-16-06	44.977105	6.413681	2370	180 x 160 x 170	170	-	1.23	0.988830
ARS-16-07	44.977791	6.414536	2352	220 x 160 x 090	90	-	1.10	0.990280
ARS-16-08	44.978638	6.415416	2344	300 x 220 x 200	200	-	2.77	0.978990
ARS-16-09	44.978680	6.415863	2346	190 x 150 x 100	100	-	2.85	0.978990
ARS-16-10	44.978843	6.416246	2338	170 x 130 x 100	100	-	3.05	0.978990
TA1c – aRG inner ridge								
ARS-16-01	44.975218	6.418637	2381	530 x 250 x 160	160	-	3.15	0.987050
ARS-16-02	44.975200	6.418562	2382	160 x 100 x 050	50	-	1.98	0.987050
ARS-16-03	44.975130	6.418802	2378	230 x 130 x 090	90	-	1.95	0.987050
PMC right lateral moraine distal face – Upper slope								
ARS-19-10	44.966097	6.414167	2554	470 x 310 x 270	130	-	4.39	0.968903
ARS-19-11	44.966457	6.414137	2555	800 x 450 x 500	280	21/83 E	2.46	0.975370
ARS-19-12	44.967730	6.414987	2526	510 x 230 x 240	0	52/119 SE	2.39	0.845903
PMC right lateral moraine outer crest								
ARS-12-06	44.967939	6.414953	2533	440 x 340 x 190	190	10/172 S	2.00	0.977335
ARS-16-19	44.967450	6.414567	2545	280 x 280 x 250	90	-	2.50	0.979573
ARS-16-20	44.966943	6.414270	2551	320 x 220 x 120	100	-	2.50	0.979573

PMC left lateral moraine distal face – Middle slope								
ARS-12-04b	44.964876	6.402192	2667	860 x 540 x 300	190	28/6 N	1.69	0.936231
ARS-19-04	44.964913	6.402196	2663	680 x 530 x 260	150	33/333 NW	3.19	0.916193
ARS-19-05	44.967778	6.405334	2566	340 x 240 x 270	215	29/286 W	3.72	0.940801
ARS-19-06	44.968980	6.405586	2552	720 x 230 x 340	170	11/155 SE	2.27	0.967485
ARS-19-07	44.969089	6.405481	2547	440 x 280 x 270	110	20/215 W	3.23	0.958970
PMC left lateral moraine outer crest								
ARS-19-01	44.969727	6.405672	2559	190 x 120 x 100	80	-	1.67	0.980291
ARS-19-02	44.969143	6.405709	2560	080 x 070 x 050	110	21/265 W	3.05	0.973477
ARS-19-03	44.969111	6.405726	2560	140 x 120 x 110	100	-	1.62	0.978392
ARS-19-08	44.969141	6.405613	2554	360 x 190 x 210	125	-	3.12	0.964998
PMC western outer frontal lobe								
ARS-16-16	44.975363	6.411454	2379	390 x 330 x 320	90	-	2.50	0.980749
ARS-16-17	44.975240	6.411419	2380	220 x 150 x 130	130	-	2.50	0.976002
ARS-18-01	44.975681	6.410592	2374	100 x 060 x 040	40	-	3.10	0.981403
ARS-18-02	44.975639	6.410965	2377	100 x 075 x 060	60	-	3.23	0.982038
ARS-18-03	44.975558	6.411117	2376	160 x 080 x 120	50	-	2.55	0.982673
ARS-19-15	44.976004	6.409837	2349	610 x 320 x 240	240	-	3.67	0.983401
PMC eastern outer frontal lobe								
ARS-19-13	44.975219	6.417099	2386	260 x 210 x 110	90	10/156 SE	3.51	0.987862
ARS-19-14	44.975251	6.416864	2389	170 x 120 x 110	85	-	3.35	0.987623
PMC right lateral moraine inner crest								
ARS-16-21	44.965920	6.413774	2564	510 x 450 x 250	70	-	2.50	0.978128
ARS-16-22	44.965602	6.413791	2571	400 x 300 x 270	160	30/320 NW	2.50	0.958303
ARS-16-23	44.965279	6.413770	2579	530 x 250 x 250	250	-	2.50	0.976063

Author contributions

Melaine Le Roy: Writing original draft, writing review & editing, Conceptualisation, Fieldwork, TCN Lab work, Interpretation, Figure preparation; **Irene Schimmelpfennig**: Writing review & editing, Conceptualisation, Fieldwork, TCN Lab work, Interpretation, Funding acquisition; Project leader; **Philip Deline**: Writing review & editing, Conceptualisation, Fieldwork, Interpretation, Funding acquisition, Project leader; **Julien Carcaillet**: Writing review & editing, Fieldwork, TCN Lab work; **Tancrède P.M. Leger**: Writing review & editing, TCN Lab work, Data processing; **Pierre Jégot**: Fieldwork, TCN Lab work; **Philippe Schoeneich**: Writing review & editing, Conceptualisation, Fieldwork, Interpretation, Funding acquisition; **Diego Cusicanqui**: Writing review & editing, DEM processing; **Felix Martin Hofmann**: Writing review & editing, TCN Lab work; **Xavier Bodin**: Writing review & editing, Fieldwork; **ASTER Team**: AMS measurement**.**